Experimental investigations of fiber dynamics for the LISA backlink

Von der Quest-Leibniz-Forschungsschule
der Gottfried Wilhelm Leibniz Universität Hannover
zur Erlangung des Grades

Doktor der Naturwissenschaften
- Dr. rer. nat. -

genehmigte Dissertation

von
M. Sc. Johann Max Rohr

2022

Abstract

The LISA mission is a planned gravitational wave observatory in space that will use inter spacecraft laser links to measure their relative distance changes. In the current baseline implementation, each spacecraft will utilize two optical subsystems. This approach requires an optical connection between the two subsystems, planned as a fiber-based connection. These optical fibers are prone to disturbances by external factors. Thus, it was found that fiber dynamics will limit the phase performance of this connection, the "backlink." The primary contributors in the scope of LISA are fiber backscatter and phase signals induced by temperature or motion of the backlink fiber.

A new transportable measurement setup was developed to obtain values for these fiber dynamics. Additional equipment was implemented to measure the temperature and motion effects: a temperature modulator and a motion simulator. The effects of ionizing radiation on the backscattered signal were investigated since backscattered light is one of the primary factors limiting the performance and not yet tested for changes in the relevant environment.

Four types of fibers were tested in backscatter and temperature coupling properties: the successor of the fibers in the LISA pathfinder mission, a polarizing fiber, and later two types of fibers with larger core diameters. It was necessary to switch to these large core fiber candidates to pre-

vent stimulated Brillouin scattering from arising. These new fiber types showed less backscatter than the previous candidates. All tested types showed no change in the backscattered power under increasing exposure to ionizing radiation within the expected levels of LISA. Therefore, no degradation of the backlink's performance is expected over the mission duration.

Temperature-to-phase coupling of the fiber candidates was measured, and it was found that the new fibers offer lower temperature coupling. This lower coupling makes the backlink less prone to phase noise induced by temperature fluctuations. The motion mock-up simulates a LISA-like fiber motion to estimate the phase coupling of this fiber motion which is less than $1\,\mathrm{rad/°}$.

Lastly, the measured coupling factors and the updated backscatter numbers were implemented in an existing simulation of the backlink's performance. These simulations show that the change in fiber type is beneficial for the backlink's performance as the noise decreases. Adding the motion into these simulations also reveals that the coupling found is low enough to be negligible and not change the performance significantly.

The ongoing "Three-Backlink experiment" and the future backlink engineering model studies can be used to verify the impact of these dynamics on the performance experimentally.

Kurzzusammenfassung

Der geplante Gravitationswellendetektor im Weltall, LISA, wird mittels Laserverbindungen paarweise die Entfernung zwischen Satelliten messen, um Gravitationswellen zu messen. Aktuell ist es vorgesehen, dass jeder Satellit zwei optische Untereinheiten beinhalten, eine optische Verbindung zwischen diesen wird daher nötig. Dieso ist derzeit faserbasiert geplant und daher anfällig für äußere Störungen. Die dadurch induzierten Phasendynamiken werden die Performance dieser Verbindung, des "Backlinks", limitieren. Für LISA sind dies Temperatureffekte, Bewegung der Fasern und Faserrückstreuung.

Um diese Dynamiken zu messen, wurde ein neues, transportables Experiment entwickelt. Weiteres Equipment wurde entwickelt, um zusätzlich die Effekte von Temperaturschwankungen und Faserbewegung zu messen. Darüber hinaus wurden Tests durchgeführt, in denen die Fasern mit ionisierender Strahlung bestrahlt werden, um deren Effekt auf die Rückstreuung zu bestimmen. Dies war bisher nicht im Rahmen von LISA getestet.

Hierfür wurden vier Fasertypen getestet: Das Nachfolgermodell der Faser in LISA Pathfinder, eine polarisierende Faser sowie zwei Fasern mit größerem Kerndurchmesser. Letztere wurden getestet, da die Gefahr bestand, dass stimulierte Brillouinstreuung auftritt bei Verwendung des ursprüng-

lichen Faserkandidaten. Es wird keine Performanceverschlechterung des Backlinks erwartet, da die getesteten Fasern keinen Anstieg der Rückstreuung zeigen, wenn die Bestrahlung erhöht wird.

Die Temperaturkopplung dieser Fasern wurde bestimmt und die neuen Kandiaten zeigen eine niedrigere Kopplung, was eine Verringerung des Phasenrauschens im Backlink bedeutet. Mit dem "Motion mock-up" wurde die Bewegungskopplung bestimmt, die in der Größenordnung von $1\,\mathrm{rad}/°$ liegt.

Die Performancesimulationen wurden mit den gemessenen Kopplungsfaktor aktualisiert und um die Bewegungskopplung erweitert. Die Simulationen zeigen, dass der Faserwechsel zu einer Performanceverbesserung führen wird und die Bewegungskopplung gering genug ist, um das Erfüllen der Anforderungen nicht zu gefährden.

Die Einflüsse der Faserdynamiken können mit dem "Drei-Backlink Experiment" und dem "Backlink Engineering-Modell" experimentell bestätigt werden.

Schlüsselwörter: LISA, Backlink, Faserdynamiken, Faserrückstreuung

Contents

List of Figures

List of Tables

Acronyms

ADC   analog-to-digital converter

AOM   acousto-optic modulator

CBV   calculated backscatter value

CDF   cumulative distribution function

CFBL   classic fiber backlink

DAQ   data acquisition

DFBL   direct fiber backlink

EM   engineering model

EOM   electro-optic modulator

ESA   European Space Agency

FBBL   free-beam backlink

FIOS   fiber injection optical system

FMZI   fiber Mach-Zehnder interferometer

FSFBL   frequency-separated fiber backlink

GRS   gravitational reference sensor

GW   gravitational wave

LDPN   laser differential phase noise

LIGO   Laser Interferometer Gravitational-Wave Observatory

LISA   Laser Interferometer Space Antenna

LO   local oscillator

LPF   LISA Pathfinder

MBV   mean backscatter value

MMF	multi-mode fiber
MOSA	movable optical sub-assembly
MZI	Mach-Zehnder interferometer
OB	optical bench
PBS	polarizing beam splitter
PBV	peak backscatter value
PCF	photonic crystal fiber
PD	photodiode
PMF	polarization-maintaining fiber
PR	photoreceiver
PRDS	phase reference distribution system
PZF	polarizing fiber
RIA	radiation induced attenuation
RIC	radiation induced compaction
RIE	radiation induced emission
SBS	stimulated Brillouin scattering
SMF	single-mode fiber
TBE	Three-Backlink experiment
TDI	time-delay interferometry
TIA	transimpedance amplifier
TID	total ionizing dose
VOA	voltage-controlled optical attenuator

Iconography

Throughout the thesis, the following symbols are used to represent different optical and electrical components. These

component**library** version three
by alexander franzen 2k+6

symbols originate from the component**library** by A. Franzen (see `http://www.gwoptics.org/ComponentLibrary/`, published under the CC-BY-NC 3.0 license) or are adapted from the component**library** indicated by ‡.

Pictogram	Description
	Laser
	Fixed mirror
	Adjustable mirror
	Half wave plate
	Quarter wave plate
	Polarizer
	Beam splitter

	‡Polarizing beam splitter
	Acousto-optic modulator (AOM)
	‡Optical fiber
	‡Fiber beam splitter
	Beam dump
	Photo receiver
	Faraday isolator
	Signal generator
	Sum
	Multiplication
	Difference
	Amplifier
PID	‡PI(D) controller

1

Introduction

With the formulation of the theory of general relativity in 1915, Einstein predicted the existence of gravitational waves (GWs) [1]. GWs are tiny perturbations of space-time resulting from accelerated masses and propagating at the speed of light. A GW is a quadrupol wave that stretches and contracts space-time perpendicular to its propagation direction. On a measurement device of length L, this will induce a relative length change, a so-called strain, of $h \approx \delta L/L$. Here, δL represents the absolut length change of the measurement device. GWs from astrophysical sources, that are reaching the Earth and are measurable by the current gound based detectors, will mostly have strains in the order of $h = 10^{-21}$ or lower [2, 3]. Figure 1.1 shows the effect of GW on a ring of test masses in two of the polarization states general relativity predicts: Plus (+) and Cross (×) polarization [4].

Because of these small strains, it is challenging to measure GWs. Therefore, for a long time, only indirect evidence existed for the existence of GWs: the observation of the orbital decay of the Hulse-Taylor binary pulsar [5–8] from the 1970s. In 2015 this changed with the direct detection of the GW emitted by the merger of two black holes, GW150914, by the two LIGO detectors [9]. Figure 1.2 depicts both of these examples. In the meantime, several further detections were made [13, 14], including binary neutron star mergers [15], black hole neutron star mergers [16] and mergers with electromagnetic counterparts [17, 18].

1
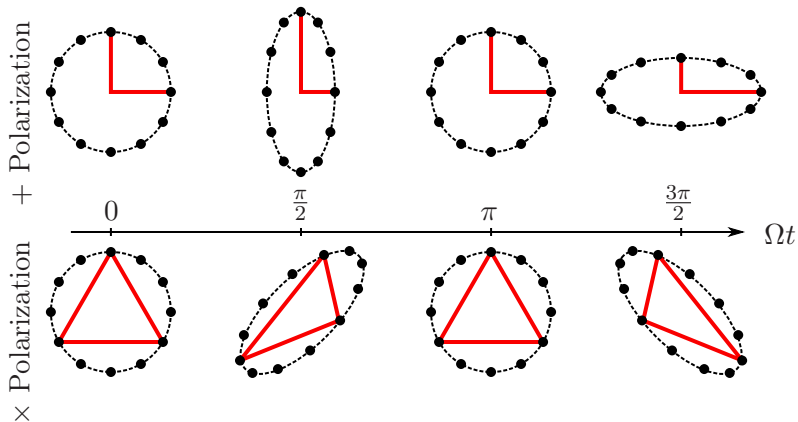
Figure 1.1: Sketch of the two polarization states of GWs. A ring of test masses is deformed by the passing GW. From left to right, the evolution of the test mass ring under the influence of the GW of one period is shown.

All these detections were done using ground-based detectors: E. g. the Laser Interferometer Gravitational-Wave Observatory (LIGO) [19, 20] and Virgo [21, 22]. Being ground-based, these detectors are limited to observing GWs of relatively high frequencies. The current generation of ground-based detectors, the "advanced" detectors, has a sensitivity range from 10 Hz up to 10 kHz [23, 24]. This results from the relatively short arm length of the detectors (some km) and several noise sources in the low frequencies, including Newtonian, gravity gradient and seismic noise [19].

To access lower frequencies of GWs, longer detector arms and stronger suppression of seismic noise are required, which is envisioned for the next generation GW detectors, like the Einstein Telescope [25] or Cosmic Explorer [26]. However, the arm length is at some point harder to increase as a result of the curvature of the Earth's surface. Therefore, moving the detector to space is necessary to make very long detector arms possible. This will also remove the influence of limiting low frequency noises of the ground-based detects but will induce other difficulties. Another proposed approach to access lower frequencies of GWs are pulsar timing
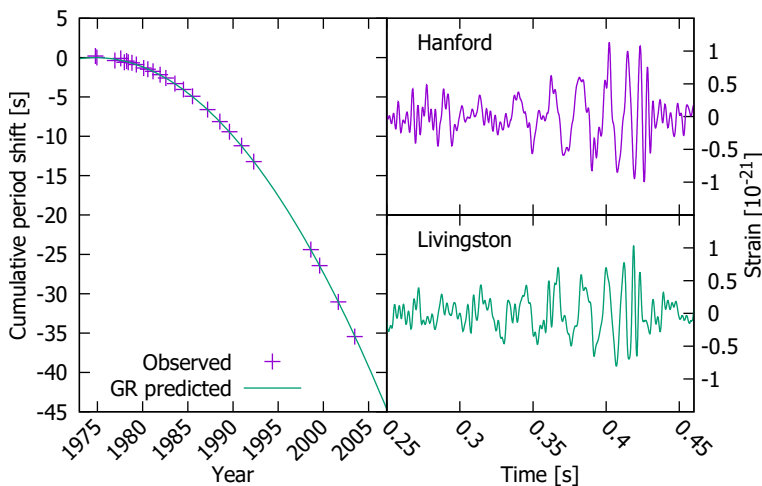
Figure 1.2: Indirect evidence and a direct measurement of GWs. Left: Observed and predicted change in the orbital period of the pulsar PSR 1913+16, which shows a good match between observation and prediction. Modified from [10] based on [11]. Right: Strain data from the two LIGO detectors for GW150914. The labels "Hanford" and "Livingston" denote the sites of the detectors. Data from [12] and the related publication [9].

arrays which will give access to GWs with frequencies in range 10^{-6} to 10^{-9} Hz [2, 27].

In between these frequency bands lie the space based detectors. The Laser Interferometer Space Antenna (LISA) is such a planned detector and will access the frequency band from 10^{-4} Hz to 1 Hz [28, 29]. The LISA constellation will consist of three spacecraft with an inter spacecraft separation in the order of million km and use inter-spacecraft laser links to measure the distance between spacecraft pairs. Due to the relative motion between the satellites, Doppler shifts will occur on the transmitted beams. Therefore, LISA will utilize a heterodyne readout scheme. The spacecraft will have to handle angular variations between one another, and, therefore, each spacecraft will feature two movable optical sub-assemblies (MOSAs). This two subsystem approach requires an optical connection between the two sub-assemblies to work, which known as "backlink." The current baseline for the implementation of the "backlink" is a fiber connection between the two MOSAs. Optical fibers, however,

are subject to disturbing phase dynamics and scattering. This will limit the backlink's performance and, in consequence, the overall measurement sensitivity of LISA.

This thesis is organized as follows: Chapter 2 introduces some basic principles related to heterodyne interferometry, including equations required to extract the backscattered power in later chapters. LISA, the backlink, and some of their difficulties are introduced in chapter 3. Chapter 4 gives a short overview of optical fibers. A measurement setup for these properties was developed, which measures the fiber properties in the same manner as these would disturb the performance of LISA. This setup is introduced in chapter 5 and the observed fiber dynamics in the chapters 6, 7 and 8. Previously, the backlink's performance was estimated in simulations based on older experiments [30]. In chapter 9, the fiber dynamics found in the experiments presented in this thesis are applied to the simulation, which leads to a performance estimation based on the experimentally observed fiber dynamics and shows a new estimate for the expected performance.

Precision Interferometry

In this chapter, we derive an equation for calculating the backscattered power from an interference signal. For this, we start from an equation of the electric field of a laser beam. We obtain an expression that includes the desired signal by interfering two such beams at a beam splitter. After that, we introduce the digitization of such a signal and explain some polarization properties of the beam.

2.1 Electric field of a laser beam

Laser interferometers are devices capable of measuring relative length changes with very high precision. Gravitational wave detectors are a possible application of laser interferometers where relative length changes down to 10^{-23} are measured by utilizing the principle of interference [2]. In this context, a laser beam can be described as an electromagnetic wave and thus with an electric or magnetic field, $\vec{E}$ or $\vec{H}$ respectively. In the following, we will only use the electric field as both, $\vec{E}$ and $\vec{H}$, are connected by the equation

$$\vec{H}(\vec{r}, t) = \frac{1}{\epsilon_0 \mu} \cdot \frac{\vec{k}}{k} \times \vec{E}(\vec{r}, t) \tag{2.1}$$

and, thus, the magnetic field is described in terms of the electric field [31, 32]. In this equation, μ is the combined permeability with $\mu = \mu_0 \mu_{\mathrm{r}}$,

where μ_{r} is the relative permeability of the permeated material and μ_0 the vacuum permeability; ϵ_0 is the vacuum permittivity, and $\vec{k}$ is the wave vector with k its corresponding wave number. $\vec{r}$ and t are the location and time where the fields are evaluated.

A simple way to describe the laser beam is the amplitude approach [33, 34], here applied to the electric field:

$$\vec{E}(\vec{r}, t) = E_0 \vec{g}(\vec{r}) \exp\left(i(\vec{k} \cdot \vec{r} - \omega t + \varphi)\right). \tag{2.2}$$

In this equation, E_0 describes the electric field amplitude, ω the angular frequency of the field, and φ describes a phase offset. The vector $\vec{g}(\vec{r})$ describes the optical, including polarization, and geometrical properties of the beam and is normalized and complex.

2.2 Interference

Interference is a phenomenon related to waves occurring when two or more waves superimpose. The result is a possible change in the observed amplitudes. Depending on the phase relation between the incoming waves, this is either an increase, decrease, or no change. The total power remains constant nonetheless.

In a laser interferometer, two laser beams interfere at a beam splitter. The following matrix gives one example to describe the properties of a beam splitter:

$$M_{\mathrm{bsp}} = \begin{pmatrix} \rho & i\tau \\ i\tau & \rho \end{pmatrix}. \tag{2.3}$$

In equation (2.3), ρ denotes the amplitude reflectivity of the beam splitter and τ the amplitude transmittivity. In the ideal, loss-free case, these combine to $\rho^2 + \tau^2 = 1$. Applying this matrix to a vector containing the amplitudes of the input ports, in the form of equation (2.2), results in the superimposed output amplitudes. This is described by equation (2.4) and depicted in figure 2.1.

$$\begin{pmatrix} \vec{E}_3 \\ \vec{E}_4 \end{pmatrix} = M_{\text{bsp}} \cdot \begin{pmatrix} \vec{E}_1 \\ \vec{E}_2 \end{pmatrix} = \begin{pmatrix} \rho\vec{E}_1 + i\tau\vec{E}_2 \\ i\tau\vec{E}_1 + \rho\vec{E}_2 \end{pmatrix}. \tag{2.4}$$

For the sake of simplicity, the complex electric fields $\vec{E}_i(\vec{r}, t)$ are abbreviated to $\vec{E}_i$, $i = 1, 2, 3, 4$.
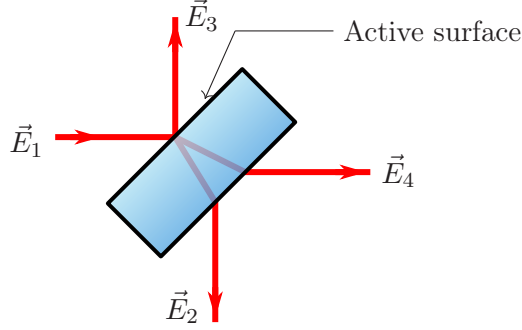
Figure 2.1: Schematic view of a beam splitter and the involved beams in the ideal case. $\vec{E}_1$ and $\vec{E}_2$ describe the two input ports. Consequently, $\vec{E}_3$ and $\vec{E}_4$ are the output ports of the beam splitter.

Assuming two input beams $\vec{E}_1, \vec{E}_2$ with the angular frequencies ω_1, ω_2, respectively, and choosing the coordinates such that the beam propagates along the z-axis, equation (2.4) results in

$$\begin{pmatrix} \vec{E}_3 \\ \vec{E}_4 \end{pmatrix} = \begin{pmatrix} E_{0,1}\rho\vec{g}_1(\vec{r})e^{i(k_1 z_1 - \omega_1 t + \varphi_1)} + iE_{0,2}\tau\vec{g}_2(\vec{r})e^{i(k_2 z_2 - \omega_2 t + \varphi_2)} \\ iE_{0,1}\tau\vec{g}_1(\vec{r})e^{i(k_1 z_1 - \omega_1 t + \varphi_1)} + E_{0,2}\rho\vec{g}_2(\vec{r})e^{i(k_2 z_2 - \omega_2 t + \varphi_2)} \end{pmatrix} \tag{2.5}$$

when applying equation (2.2). The intensity of an outgoing beam, e. g. $\vec{E}_3$, can be calculated using square-law detection. This is applicable when a photoreceiver (PR) is placed in the beam, and the diameter of the PR is significantly larger than the diameter of the beam and, thus, boundary effects can be neglected:

$$\begin{aligned} I_3 &= \frac{c\epsilon_0 n}{2}|\vec{E}_3|^2 \\ &= \frac{c\epsilon_0 n}{2}\left(E_{0,1}^2\rho^2|\vec{g}_1(\vec{r})|^2 + E_{0,2}^2\tau^2|\vec{g}_2(\vec{r})|^2 \right. \\ &\quad \left. + 2E_{0,1}E_{0,2}\rho\tau\vec{g}_1(\vec{r})\vec{g}_2(\vec{r})\sin(t(\omega_2 - \omega_1) + \Delta\varphi)\right). \tag{2.6} \end{aligned}$$

In these two equations, $E_{0,i}$ represent the original field amplitudes of the beams, c is the speed of light, n is the refractive index and the $k_i z_i$ and φ_i terms are summarized in the term $\Delta\varphi$, which describes the phase difference of the interfering beams. The resulting power shows a constant part and an oscillating part. In the case of $\omega_1 = \omega_2$ one speaks of homodyne interferometry whilst otherwise (when $\omega_1 \neq \omega_2$) of heterodyne interferometry. For the application presented in this thesis, heterodyne interferometry offers two significant advantages: Its capability of measuring effects that induce phase changes over several wavelengths and the relatively easy way to measure very small optical powers, see e. g. [35].

Equation (2.6) can be simplified by using the property that the $\vec{g}_i$ are normalized:

$$I_3 = \frac{c\epsilon_0 n}{2} \left(E_{0,1}^2 \rho^2 + E_{0,2}^2 \tau^2 + 2 E_{0,1} E_{0,2} \rho\tau \vec{g}_1(\vec{r})\vec{g}_2(\vec{r}) \sin(\omega_{\text{het}}t + \Delta\varphi) \right). \tag{2.7}$$

Here, we introduced the heterodyne frequency $\omega_{\text{het}} = \omega_2 - \omega_1$. The photodiode (PD) placed in the beam integrates this intensity and results in the photo current

$$i_{\text{PD}} = \mathcal{R} \left(\rho^2 P_1 + \tau^2 P_2 + 2\rho\tau \sqrt{P_1 P_2 \eta} \sin(\omega_{\text{het}}t + \Delta\varphi) \right). \tag{2.8}$$

Here, $\mathcal{R}$ represents the responsivity of the PD in A W^{-1}, and P_i are the optical powers of the involved beams. A new property, the heterodyne efficiency η is introduced here, with $\sqrt{\eta} = \vec{g}_1(\vec{r})\vec{g}_2(\vec{r})$. The heterodyne efficiency characterizes the interference quality and is in the range $\eta = 0 \dots 1$.

A transimpedance amplifier (TIA) (see e. g. [36]) can be used to convert this current to a more easily measurable voltage:

$$U_{\text{PD}} = R_{\text{TIA}} i_{\text{PD}}$$

$$= R_{\text{TIA}} \mathcal{R} \left(\underbrace{\rho^2 P_1 + \tau^2 P_2}_{\text{DC part}} + \underbrace{2\rho\tau \sqrt{P_1 P_2 \eta} \sin(\omega_{\text{het}}t + \Delta\varphi)}_{\text{AC part}} \right). \tag{2.9}$$

One can split this equation into two contributions, the DC part and the AC amplitude:

$$U_{\text{PD}}^{\text{DC}} = R_{\text{TIA}} \mathcal{R} \left(\rho^2 P_1 + \tau^2 P_2 \right), \tag{2.10}$$

$$U_{\text{PD}}^{\text{AC}} = R_{\text{TIA}} \mathcal{R} \cdot 2\rho\tau \sqrt{P_1 P_2 \eta}. \tag{2.11}$$

These equations are crucial to reconstruct the backscattered power in chapter 5 and will be used there in several steps. The second of these equations also shows why heterodyne interferometry is a good way to measure very low powers: The measured amplitude scales with $\sqrt{P}$. For example, measuring an optical power in the pW-range would result in a measurement in the order of 10^{-6} instead of 10^{-12} for a comparable direct measurement.

Furthermore, these equations allow calculating the contrast C, which defines how well the interference fringes are visible and is given as

$$C = \frac{U^{\text{AC}}}{U^{\text{DC}}}. \tag{2.12}$$

Alternatively, the contrast can be calculated using the extrema of the signal observed by a PR:

$$C = \frac{U_{\text{max}} - U_{\text{min}}}{U_{\text{max}} + U_{\text{min}}} = \frac{P_{\text{max}} - P_{\text{min}}}{P_{\text{max}} + P_{\text{min}}}. \tag{2.13}$$

The second part of this equation, with the optical powers, follows from the linear conversion of power to voltage in the PR.

When the properties of the detection system are unknown, the heterodyne efficiency can be calculated using the contrast C and the optical powers P_1 and P_2 of the interfering beams [37]:

$$\eta = \frac{C^2}{4} \frac{(P_1 + P_2)^2}{P_1 P_2}. \tag{2.14}$$

Chapter 2

2.3 Amplitude and phase read out

The general scheme of reading out the amplitude and phase of an interference signal is depicted in figure 2.2. A PR converts the incoming laser beam into a voltage signal which, subsequently, is digitized using an analog-to-digital converter (ADC). This digitized time-series is then multiplied with a sine and cosine term containing the demodulation frequency ω_{demod}. Subsequently, a low pass filter removes the $2f$ terms of the multiplication, which occur as the multiplication results in sum and difference terms. This results in the so-called I- and Q-values.
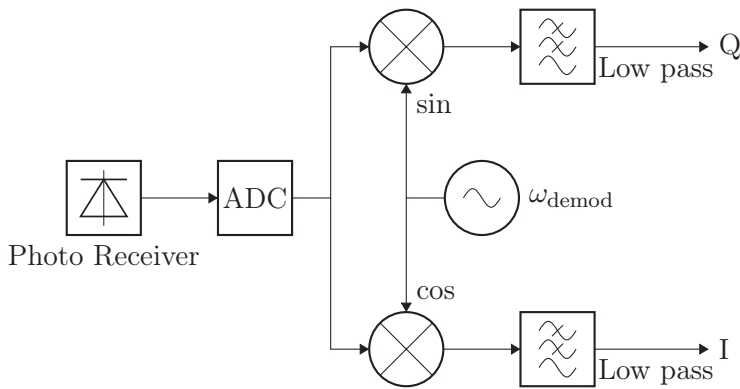
Figure 2.2: Overview of the I-Q demodulation: After detecting and digitizing the signal, the ADC-signal is multiplied by both, a sine and a cosine term. The application of a low pass filter obtains the I and Q values.

Using the I and Q values, the amplitude U^{AC} and phase φ are calculated as follows:

$$U^{\mathrm{AC}} = 2 \cdot \sqrt{Q^2 + I^2}, \tag{2.15}$$

$$\varphi = \arctan\left(\frac{Q}{I}\right). \tag{2.16}$$

The phase obtained this way originates from the sine term in equation (2.9) and will be used in chapters 7 and 8 to calculate the phase coupling of temperature and motion effects.

Another significant value is the averaged measured signal U^{DC} given by

$$U^{\mathrm{DC}} = \frac{1}{N} \sum_{i=1}^{N} U_i. \tag{2.17}$$

Here, N is the number of samples over which the averaging happens. It is essential to choose N such that the demodulation frequency is removed from the averaged signal, otherwise, U^{DC} is not useful. This is achieved by choosing N such that the average is calculated over several cycles of the demodulation frequency.

For the phase readout, it is crucial to match the demodulation frequency precisely to the frequency of the observed signal, as otherwise, this results in a linear drift of the measured phase. Figure 2.3 shows the effect in the phase measurement if the signal frequency and the demodulation frequency are not equal. In the plotted case, the difference between the demodulation frequency and the signal frequency is $\Delta f = 0.08\,\mathrm{Hz}$, and the heterodyne frequency is $f_{\mathrm{het}} = 5\,\mathrm{kHz}$. This slight frequency offset,
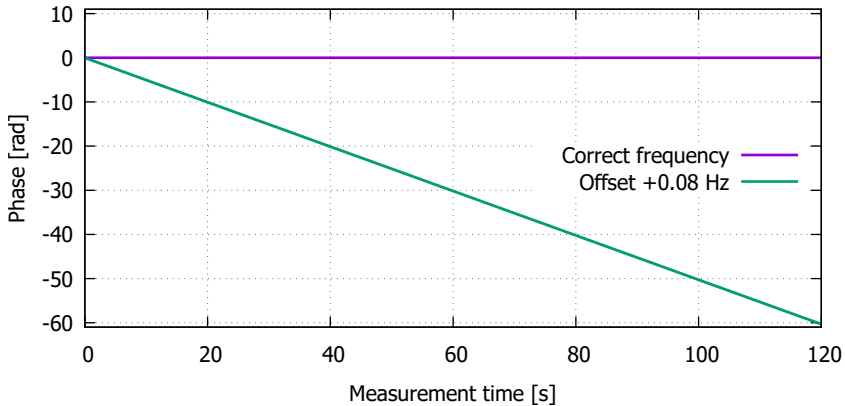
Figure 2.3: Simulated time series of the demodulated phases of a $5\,\mathrm{kHz}$ heterodyne signal with a constant phase: In the case of the correct demodulation frequency, the measured phase is constant. However, if the demodulation frequency shows only a tiny offset, the measured phase drifts linearly.

$0.0016\,\%$ of f_{het}, results in a phase drift of about $60\,\mathrm{rad}$ over the short measurement duration of $2\,\mathrm{min}$, which can obscure the phase effect to be

measured. The resulting drift can be removed by applying de-trending techniques; in our case, it is often sufficient to subtract a linear fit. Another approach to counteract this problem is using a frequency-tracking phase meters as in [38].

2.4 Polarization

In the previous sections, the polarization of the optical field was only introduced indirectly, i. e., hidden in the factor $\vec{g}(\vec{r})$ in equation (2.2). A common approach describing an optical field's polarization state is through the so-called "Jones vectors" [39, 40]. These represent the amplitudes of the electrical field in the x- and y-direction as the z-direction is chosen to equal the propagation direction of the beam:

$$\begin{pmatrix} E_\mathrm{x}(t) \\ E_\mathrm{y}(t) \\ 0 \end{pmatrix} \rightarrow \begin{bmatrix} E_{0,\mathrm{x}}e^{i\varphi_\mathrm{x}} \\ E_{0,\mathrm{y}}e^{i\varphi_\mathrm{y}} \end{bmatrix}. \tag{2.18}$$

This equation shows that Jones vectors contain the amplitudes and phase information of the beam's field in x- and y-direction. For simplification reasons, these vectors are commonly normalized. Table 2.1 lists the Jones vectors for some polarization states. The linear polarization states are

Table 2.1: Normalized Jones vectors of some polarization states.

s-polarized	p-polarized	left-hand circular	right-hand circular
$\begin{pmatrix} 1 \\ 0 \end{pmatrix}$	$\begin{pmatrix} 0 \\ 1 \end{pmatrix}$	$\frac{1}{\sqrt{2}}\begin{pmatrix} 1 \\ i \end{pmatrix}$	$\frac{1}{\sqrt{2}}\begin{pmatrix} 1 \\ -i \end{pmatrix}$

s-polarized, orthogonal to the optical table, and p-polarized, parallel to the optical table. A phase delay between the two components results in a non-linear polarization state. This is visible in the normalized Jones vectors by the appearance of the imaginary number i. A combination of linear and circular states results in an elliptical polarization state. Furthermore, these vectors show that two beams of orthogonal polarization states will not interfere [41] as their scalar product is zero. The exper-

iments presented throughout this thesis only use the linear polarization states.

For LISA and other interferometric applications, polarization fluctuations can result in excess noise. A spurious beat note is detected if both interfering beams carry some power in the equal but undesired polarization state. This polarization noise can limit the performance of an interferometer [42]. In LISA, we call this small vector noise since the spurious amplitude is small compared to the nominal signal. However, the spurious beat note has its own, often unstable, phase that contributes to the phase noise [43]. Figure 2.4 depicts this noise coupling in the phasor view by utilizing vector addition. In the worst case, the small vector is orthogonal to the nominal signal. If the phase relation between nominal
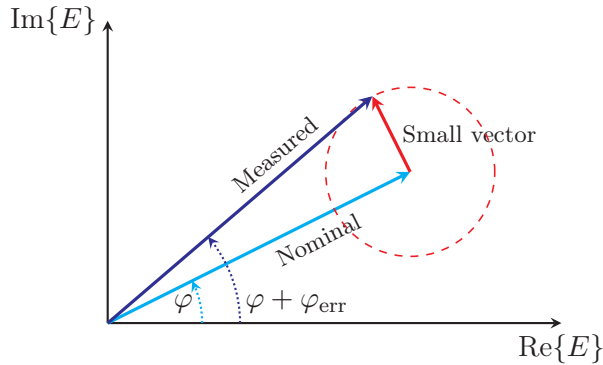
Figure 2.4: Phasor diagram of the small vector noise: The diagram rotates with the angular frequency ω of the field E. The small vector rotates around the nominal vector. Depending on the phase relation between nominal and small vector, a phase error φ_{err} is induced in the measurement.

and small vector is not constant, the measured phase fluctuates between $\varphi - \varphi_{\text{err}}$ and $\varphi + \varphi_{\text{err}}$.

In the experiments presented in this thesis, polarization is relevant as some optical media are birefringent. Birefringence occurs if such an optical medium has different refractive indices for the two linear polarization states [44]. This is also true for optical fibers and results in coupling between the two polarization states in optical fibers [45]. Therefore, po-

larization induced small vector noise is expected when utilizing optical fibers.

The LISA Backlink

In this chapter, we shortly introduce a proposed space-based GW detector, the Laser Interferometer Space Antenna (LISA), and its measurement principle. Subsequently, we introduce the required backlink and its foreseen fiber-based configuration and familiarize ourselves with former and planned experiments regarding the backlink. Lastly, we introduce possible issues arising from the space environment and the resulting exposure to ionizing radiation.

3.1 The Laser Interferometer Space Antenna

LISA is a planned, space-bound gravitational wave observatory that will access the frequency range from $100\,\mu\text{Hz}$ to about $1\,\text{Hz}$ [28, 29, 46, 47]. By its lower frequency band compared to the ground-based detectors ($10\,\text{Hz}$ to $10\,\text{kHz}$), LISA adds fundamental new insights in GWs, e. g. measuring mergers of massive black holes, mergers with extreme mass ratios [48], or observing stellar-mass mergers months or years before visible in the ground-based detectors [49].

The LISA constellation consists of three identical spacecraft placed in heliocentric orbits. The orbits of the individual spacecraft are chosen such that pairwise, the distance between two spacecraft is about $2.5\,\text{million km}$. The center of the triangular configuration will be placed at a distance

of about 1 au from the Sun, trailing the Earth by about 20°, and the constellation will be tilted by 60° with respect to the ecliptic [50]. This is depicted in figure 3.1. The measurement principle of LISA consists of three measurements per interferometer arm: a measurement between test mass, located in the gravitational reference sensor (GRS), and spacecraft, the inter spacecraft measurement, and another measurement between test mass and spacecraft, but for the remote spacecraft [51]. Combined, this results in a measurement between the local and remote spacecraft, which allows the detection of GWs. This measurement approach is depicted in figure 3.2.

The constellation will be in a primary-transponder configuration as the power received by a transponder spacecraft is too low for a reflection. Only several 100 pW arrive at the transponder spacecraft from an initial power in the order of 2 W, which renders the laser interferometric setup with a direct reflection of the light technically unfeasible [29]. A direct reflection would result in optical power in the order of zW returning to the primary spacecraft, which would be extremely challenging to detect. Additional challenge are armlength and pointing changes of the exchanged laser beams due to the orbital mechanics. The armlength variations will be in the order of some 10 000 km [52].
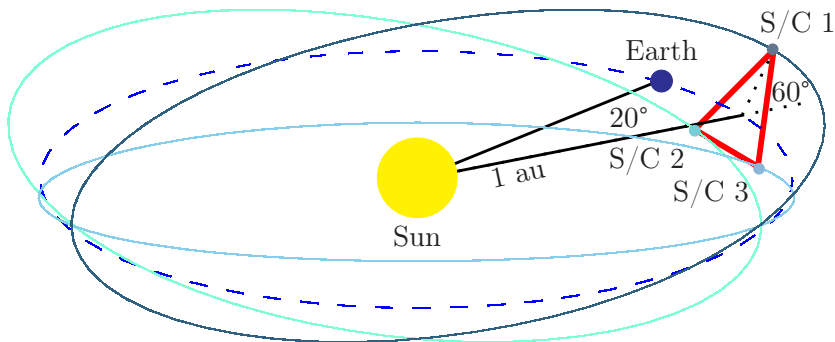
Figure 3.1: Orbital overview of the LISA mission (not to scale): The constellation trails the Earth by about 20° and is tilted by about 60° with respect to the ecliptic.

As consequence of this, the laser links in the LISA constellation would be lost over the orbits as the movement induces an angular variation along
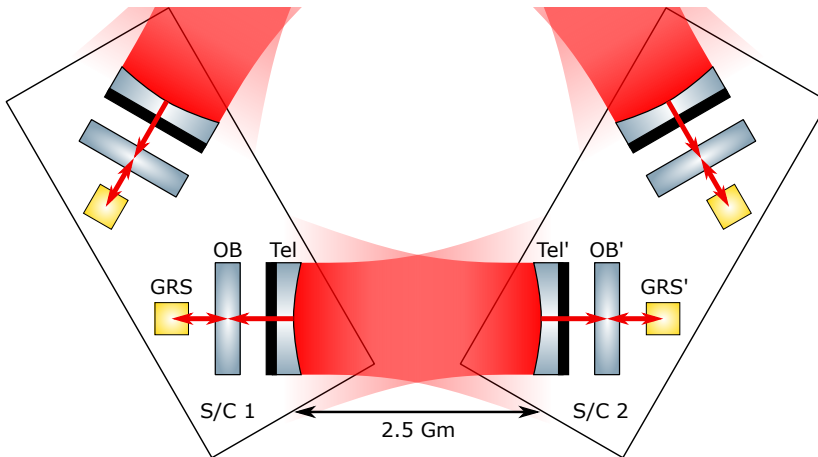
Figure 3.2: Optical length measurement in LISA: The measurement chain consists of a measurement between the GRS and the OB (test-mass interferometer), the inter-spacecraft measurement (long-arm interferometer) and another measurement between OB, and GRS on the remote spacecraft. "Tel" denotes the telescopes.

the arms of about $\pm1.5°$ [53, 54]. A more recent orbit consideration gets this down to $\pm1.1°$ [55]. Therefore, active pointing of the light sent to the distant spacecraft is required. Otherwise, the laser link will interrupt. Currently, two approaches are considered: telescope pointing and in-field pointing.

The satellites feature a single optical bench and one GRS in the in-field pointing approach. The pointing is performed by a steering mirror within the optical path in the telescope [56]. However, this approach is out of scope for this thesis and will not be further elaborated here. Furthermore, it does not represent the current baseline implementation for LISA at the time of writing this thesis.

In the case of telescope pointing, which is the current baseline design [50], the telescope is a fixed unit and moves to steer the outgoing beam to the remote spacecraft. Consequently, two movable optical sub-assemblies (MOSAs) are required within each spacecraft to address the pointing of both laser links. Each MOSA has its own optical bench and GRS, which are rigidly connected to the telescope. Thus, an optical connection between the two optical benches is required to distribute the local oscillator

and create a phase reference [50]. Both are established by the phase reference distribution system (PRDS), which is commonly called "backlink." In the following section, we will closely look into this intra-spacecraft connection.

3.2 The backlink

3.2.1 Purpose and goals

With the baseline decision for telescope pointing, the PRDS is required for LISA to function properly as each spacecraft houses two separate optical benches (OBs). First, the actuation of the MOSAs requires this link to be flexible, i. e., to keep the connection throughout the whole mission. Next, this connection needs to be bidirectional to exchange the light between both optical benches. Here, it is crucial that the path length in both directions is the same for the light transmitted through the fiber, i. e. the transmission in both directions is reciprocal. A fiber-based implementation is the current baseline for LISA. However, a free-beam approach is an option as well [57, 58]. Any inequality in this is called non-reciprocity, and its noise level is required (see [59]) to be below

$$s_{\text{backlink}}(f) = 3\,\text{pm}/\sqrt{\text{Hz}} \cdot \sqrt{1 + \left(\frac{2.8\,\text{mHz}}{f}\right)^4} \qquad (3.1)$$

where f is the frequency. The goal is to reach a non-reciprocity below $3\,\text{pm}/\sqrt{\text{Hz}}$. With a non-reciprocity below this level, the usage of time-delay interferometry (TDI) is possible [60, 61]. TDI is a post-processing technique to suppress the laser frequency noise that is dominating the readout signal of the LISA long-arm interferometer otherwise and to extract the scientific signal from the measurements [60, 61].

Previous experimental studies have shown that it is feasible to achieve a performance close to this required limit of non-reciprocity. The required performance should be reachable with the addition of suppression techniques of other impeding factors [62–65]. A short summary of these studies follows in the next section. A new, more elaborate study to ad-

dress the shortcomings concerning the former results was started in the form of the Three-Backlink experiment (TBE). The TBE is designed to compare three different approaches to implement the PRDS, one of which is an implementation similar to the previously mentioned experiment [57, 58]. The building and implementation of the TBE are ongoing as of writing this thesis. A short description of the TBE follows in section 3.2.5. Another ongoing part of the study is the building and implementation of the PRDS engineering model (EM), which will show the performance of the LISA-like implementation of a PRDS and will also be used for qualification purposes. The EM is also described briefly in section 3.2.5.

3.2.2 The "classic" backlink experiment

The previous study by R. Fleddermann [63] has shown that the required performance in the classic fiber backlink (CFBL) is, in principle, achievable. However, in these studies, several mitigation steps were required. The setup used for these measurements is depicted schematically in figure 3.3. Two beams (A and B) of different frequencies are counter-propagating through a fiber and interfered with the other beam in the interferometers MEAS1 and MEAS2, respectively. A reference interferometer, REF, is utilized to suppress common noise sources. The fiber, therefore, simulates the PRDS. The difference between the phase signals of interferometers MEAS1 and MEAS2 yields the so-called non-reciprocity and must fulfill the non-reciprocity requirement, which is given in equation (3.1).

The core results of these measurements are depicted in figure 3.4 and show three measurements: The initial measurement (violet), furthest from the requirement, a measurement with stray light suppression by addition of attenuators (green, see [66]), and the best performance from [63] by applying several additional noise corrections (cyan), i. e. balanced detection, stray light suppression, thermal shielding and pointing correction, but not including attenuators. From these noise suppression techniques, balanced detection and the addition of attenuators result in the strongest noise reduction; both of these are shortly explained in section 3.2.4. The best
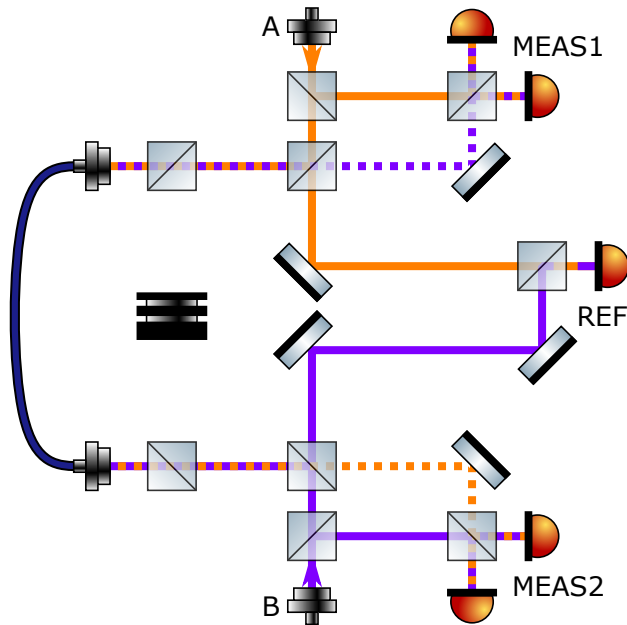
Figure 3.3: Overview of the classic fiber backlink as presented in [63]. Two beams of different frequencies (A and B) were transmitted through an optical fiber in a counter-propagating manner and measured in the two interferometers (MEAS1 and MEAS2). Dotted lines depict the transmitted beams. A reference interferometer (REF) is used to suppress common noise. The difference between the signals of MEAS1 and MEAS2 reveals the non-reciprocity of the fiber path.

measurement fulfills the requirement in the upper half of the frequency band and is close to it in the lower half and, in consequence, shows that a fiber-based PRDS can principally be realized. These measurements reveal that stray light is the limiting factor in performance.

3.2.3 Stray light coupling

As shown by the CFBL, stray light couples through different ways into the phase readout. We can approximate the phase error φ_{err} induced by the stray light as

$$\varphi_{\text{err}} \approx \sin(\varphi_{\text{SL}}) \cdot \sqrt{\eta_{\text{SL}} \frac{P_{\text{SL}}}{P_{\text{nominal}}}} \qquad (3.2)$$
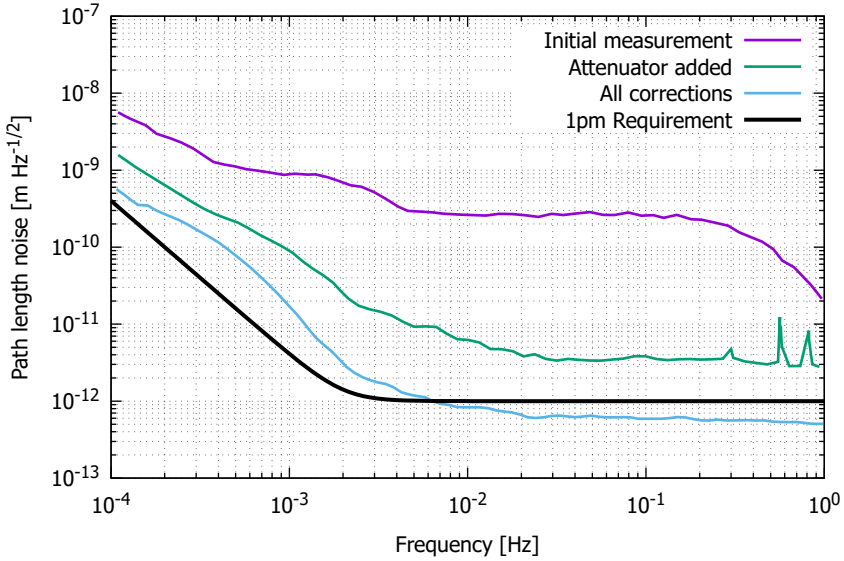
Figure 3.4: Performance of the CFBL as found by [63] and [66]: The initial measurement and a measurement with added attenuators for stray light suppression are shown. In addition, the final result after applying several noise corrections, but without attenuators, is depicted, which is close to fulfilling the requirement given by equation (3.1).

when the spurious distrubance is small compared to the nominal signal [43]. In this equation, φ_{SL} is the phase of the stray light, P_{SL} the power in the stray beam, η_{SL} the heterodyne efficiency of the stray light interfering with the local oscillator (LO), and $P_{nominal}$ denotes the power of the nominal beam interfering with the LO. Equation (3.2) shows further that the phase of the stray light is a more significant contributor (couples non-linearly; for small phase errors around zero, this coupling can be approximated as linear) to the phase error than the sole stray light amplitude (which couples with the square-root). In the case of a fiber connection, this allows coupling of several other spurious effects into the readout phase, e. g. the thermal aspects observed in the CFBL by [63].

For the LISA spacecraft, the dynamics that couple into the phase will mainly be thermal coupling and motion in the form of fiber bending [30]. The thermal coupling will project the thermal environment within the spacecraft onto the optical phase propagating through the backlink

fiber as the refractive index depends on the temperature of the fiber (see, for example, the thermal dependence of silica [67]). The actuation of the MOSAs causes the motion coupling that couples into the phase via bending of the fibers as bends in optical fibers result in a phase shift of the optical signal transmitted through those [68]. Both of these effects are factors that can limit the achievable performance of the backlink and, thus, can be a hindrance.

3.2.4 Stray light suppression

In the CFBL, the addition of attenuators and balanced detection were used to reduce the effect of the stray light in the phase measurement [63, 66]. Considering equation (3.2), it is obvious that the power ratio between stray light and nominal beam at the same optical frequency determines the impact of the spurious beam. Therefore, placing attenuators such that this power ratio is increased in favor of the nominal beam the spurious phase contribution is reduced. In the scope of the CFBL, this was done in [66].

Balanced detection, on the other hand, utilizes the properties of the re-combining beam splitter as the reflected port will see a phase shift of π with respect to the transmitted port [69]. In consequence, stray light contributions that interfere before the recombination beam splitter can be removed. This is achieved by placing PRs in both output ports and calculating the difference of the signals. Utilizing the phasor view of the signals, as depicted in figure 2.4, allows to visualize the working principle of balanced detection and the suppression of the stray light induced phase error. Figure 3.5 shows the suppression through balanced detection. The shift induced by the beamsplitter causes the nominal phasors (cyan) to point into opposite directions. The straylight signal that interfered before the beamsplitter (red) is not affected by this phase shift and, thus, shows in the same direction in both cases. By utilizing vector calculus, we can shift the phasor of the second PR such that the contribution of the straylight is mitigated. Figure 3.5 (c) depicts this and shows that the resulting phasor (orange) has the same phase as the nominal phasor
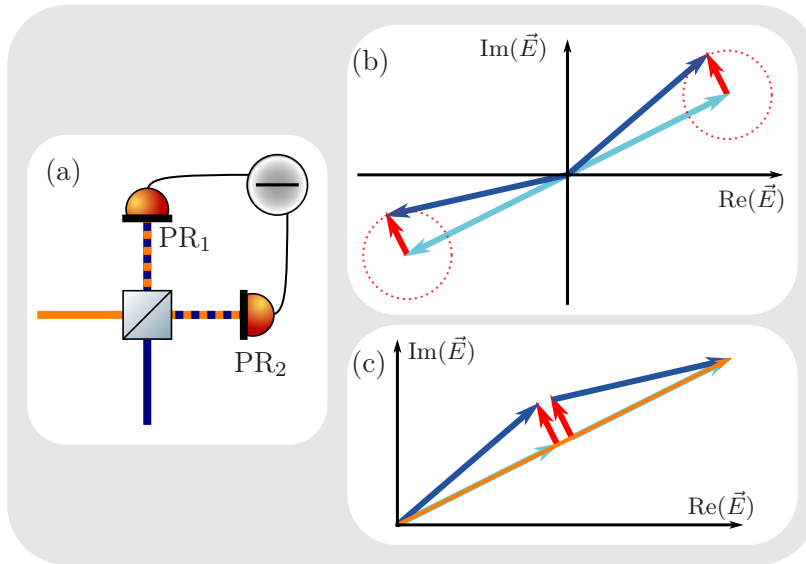
Figure 3.5: Overview of balanced detection for noise suppression: Part (a) shows the optical setup to utilize balanced detection. The difference of the two PRs-signals is not limited by a spurious interference of stray light that happens before the recombination beamsplitter. Part (b) shows the phasors of the signals observed by the two PRs. Here, the phase shift of π between the transmitted and reflected beam is visible. The phasors follow the scheme of figure 2.4. The resulting phase noise suppression is depicted in part (c). Here, the phasors are moved according to the vector calculus used in balanced detection. The orange phasor shows the result of the balancing process which shows the same phase as the nominal phasor (cyan).

(cyan). For balanced detection, the achieved suppression of the stray-light contribution depends critically on the matching of the gains of the complementary signals, i. e. the matching of the lengths of the phasors. However, it is possible to optimize the matching in post-processing procedures as shown in [64] where a noise suppression by more than two orders of magnitude was achieved.

3.2.5 Three-Backlink Experiment and Engineering Model

The Three-Backlink experiment (TBE) was designed to compare the direct fiber backlink (DFBL), which is a derivation of the CFBL, to other implementation schemes, namely the frequency-separated fiber backlink (FSFBL) and the free-beam backlink (FBBL) [43, 58]. These alternative schemes include approaches to suppress the noise sources identified in [63] by either removing its cause or shifting the resulting beat note frequency, measured on the PR, to a frequency differing from the nominal beat note frequency.

Figure 3.6 shows the implementation of the TBE schematically, which consists of two separate optical benches featuring four interferometers, each is establishing three backlink implementations.

The DFBL closely resembles the CFBL from [63] but features an additional Faraday isolator to prevent light from the DFBL and FBBL interferometers, reflecting or scattering back from the TX fiber injection optical system (FIOS) and fiber.

The second-fiber based implementation tested, the FSFBL, needs additional lasers in the form of the additional local oscillators, ALO and ALO′. By implementing these, the beat frequency of the stray light is different from the beat frequency of the desired signal. Thus, the stray light influence from the fiber is suppressed. However, the FSFBL implementation needs a second interferometer per bench, i. e., two reference interferometers, to create a phase reference between the two local lasers.

The last implementation, the FBBL, removes the fiber as a stray light source by implementing a free beam path between the two benches. A pair of steering mirrors keeps the link between the two benches when these are rotated. This rotation simulates the angular breathing.

The final part to verify the functionality of the backlink is the EM, which is being built, as of writing this thesis. The engineering model is an implementation of the DFBL, including all required suppression methods, and uses LISA-like components, which means that the components are designed and coated in the same way as those planned to be used on the
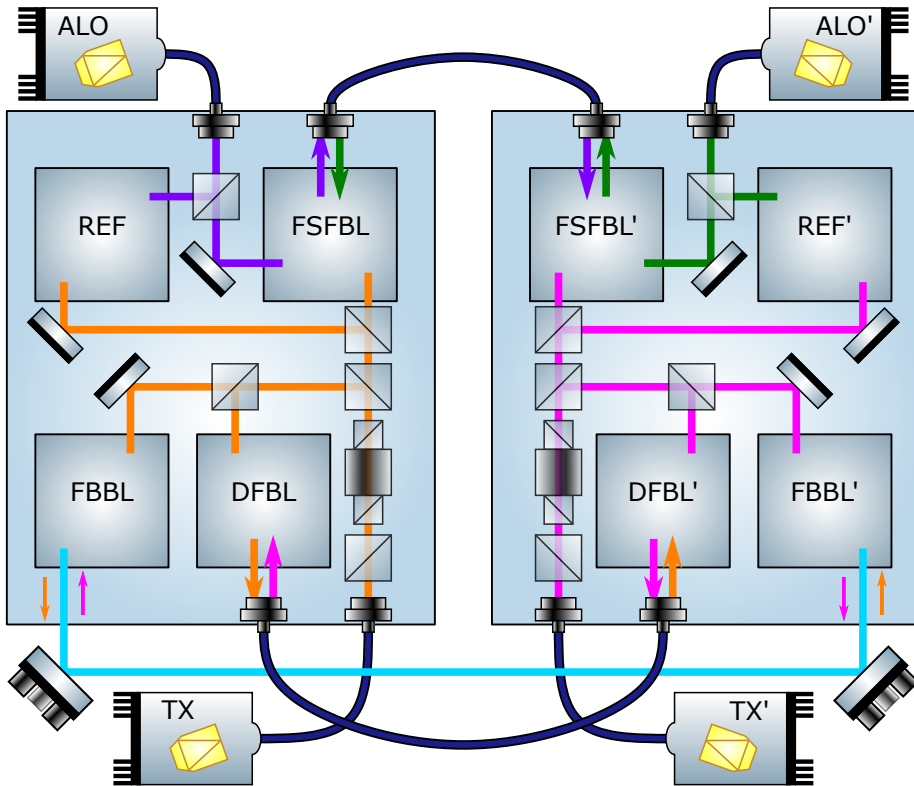
Figure 3.6: Simplified overview of the Three-Backlink experiment. Two optical benches with four interferometers each will be used to compare the optical performance of different backlink candidates: direct fiber backlink (DFBL), free-beam backlink (FBBL) and the frequency-separated fiber backlink (FSFBL). In addition, each bench features a reference interferometer between the TX and ALO lasers. The steering mirrors required for the FBBL are placed besides the OBs.

LISA optical bench [30]. Similar to the CFBL, the EM will feature two measurement interferometers, one at each end of the backlink connection, and a reference interferometer between the two lasers feeding the experiment. Two characteristics of the EM are essential: Some space on EM's optical bench is reserved for retrofitting an additional backlink to test the redundancy approach's influence after verifying the single backlink's performance. The other point is the last beam splitter in front of the backlink fibers: This beam splitter will have a reflectivity of 99.5 %. Therefore, only a tiny amount of light from the lasers is coupled into
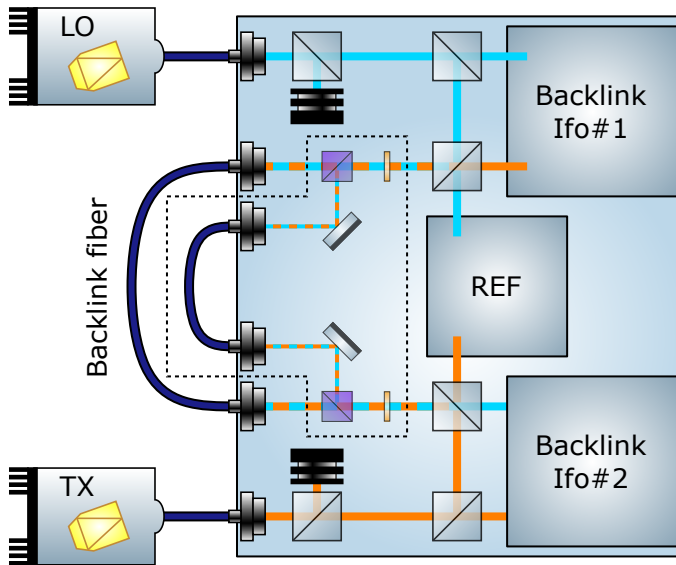
Figure 3.7: Simplified overview of the engineering model. The EM will consist of a DFBL configuration with interferometers on both ends of the backlink fiber as well as a reference interferometer between the two lasers. The first beamsplitter simulates the beam going to the telescope and reflects 98 % of the light. An option to retrofit a redundant backlink fiber at a later point is included, the required components are in the dashed area.

the backlink fiber, and most of the light going through it is directed into the backlink interferometers.This ratio of reflection and transmission will reduce the ratio of the stray light generated in the fiber connection to the nominal light in the backlink [30] as the stray light effectively passes this beam splitter twice.

3.3 Radiation environment

As a spaceborne GW observatory, LISA will naturally be exposed to ionizing radiation. For missions in orbits close to Earth, the radiation trapped in the Van Allen belts is problematic [70, 71]. For LISA, the transfer time through the Van Allen belts is short compared to the mission duration [29, 72], and the subsequent radiation from the Van Allen belts can be neglected. Therefore, the primary attribution considered for LISA

is radiation emitted by the Sun that consists of electromagnetic, plasma, and energetic particle components. The solar electromagnetic radiation and the plasmas are shielded by the outer hull of the spacecraft [72] and, thus, not further discussed here.

For the LISA backlink, the energetic particle radiation is critical. This type of radiation penetrates the spacecraft's hull and, consequently, reaches the backlink, including the related optical fiber. Hence, solar protons and gamma radiation are the relevant part of the energetic particle radiation for the backlink [72]. Though, gamma radiation arises as secondary radiation from the solar protons hitting the spacecraft. Thus, solar protons are the defining contributor to the relevant radiation environment. For LISA, the expected doses to reach within the spacecraft are calculated in dependence of the aluminium-equivalent shielding the spacecraft provides; these values are given in [72]. Different assumptions were applied in the two radiation measurement campaigns presented in chapter 6.

For the backlink, it is critical that the ionizing radiation can alter the properties of optics and fibers and, in consequence, degrade the transmission and reflection properties. This is especially critical for the fiber connecting the two OBs if its transmission degrades. Even more so, if the formation of color centers within the fiber results in an increased backscattering. Color centers are absorption points within the fiber that re-emit absorbed photons optically or thermally [73]. This would result in a degradation of the performance of the backlink since the increased scattering would increase the non-reciprocity. Chapter 4 gives an overview of optical fibers and introduces some of the effects caused by exposure of fibers to ionizing radiation.

Chapter 3

4
Optical Fibers

In this chapter, we introduce the fundamental working principle of optical fibers, different fiber types, and some fiber-related loss mechanisms. These are driving factors of the impedimental backscatter limiting the backlink. We shortly discuss the effects of ionizing radiation on the properties of optical fibers. Lastly, we introduce two ways to describe optical fibers' backscattering properties, which are used throughout the experimental work in this thesis.

4.1 Fundamentals

Optical fibers are typically made of glass and used to transmit light over long distances or other routes that are not easily accessible for a free-space transmission. Originally, they have been developed for telecommunication and are often used to transmit data in high-speed and low in distortions [74, 75]. However, fibers are not only used for data transmission but also in numerous other applications [76–78], e. g. fiber optic thermometers [79, 80] or fiber optic hygrometers [81], since fibers are suitable as sensors for many effects [82, 83].

Optical fibers rely on total internal reflection to guide the light. We can use Snell's law to describe this phenomenon:

$$n_1 \cdot \sin(\alpha_1) = n_2 \cdot \sin(\alpha_2). \tag{4.1}$$

Here n_1 and n_2 are the refractive indices of the two involved media. α_1 is the incidence angle in the medium of refractive index n_1 and α_2 of n_2. By rearranging equation (4.1), we can obtain an expression for the critical angle α_c where the refracted beam is propagating along the interface between the two media, thus, $\alpha_2 = 90°$:

$$n_1 \cdot \sin(\alpha_c) = n_2 \cdot \sin(90°) = n_2$$

$$\Longleftrightarrow \qquad \alpha_c = \arcsin\left(\frac{n_2}{n_1}\right), \tag{4.2}$$

If the angle of the incoming beam exceeds the critical angle, i. e. $\alpha_1 \geq \alpha_c$ total internal reflection occurs.

Adopting the notation according to figure 4.1, we find that

$$\vartheta_c = \arcsin\left(\frac{n_\text{clad}}{n_\text{core}}\right) \tag{4.3}$$

applies for the critical angle of the total internal reflection within a fiber.

As long as the relation $\vartheta_2 > \vartheta_c$ is fulfilled, the fiber will guide the light. One can calculate an acceptance cone for the fiber using the critical angle as follows: By using the angular sum of a triangle, we obtain the angle $\vartheta_1 = 90° - \vartheta_2$ after refracting the beam into the fiber and can use Snell's law to derive the incidence angle ϑ_in onto the fiber's face. By using ϑ_c in place of ϑ_2 we obtain the acceptance angle of the fiber, which forms a cone due to the rotation symmetry of the fiber:

$$n_0 \cdot \sin(\vartheta_\text{in}) = n_\text{core} \cdot \sin(90° - \vartheta_2). \tag{4.4}$$
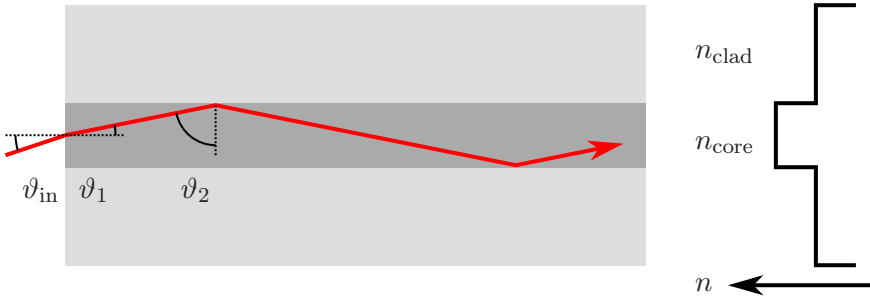
Figure 4.1: Sketch of total internal reflection (left) and the refractive index profile of a fiber (right): A beam incident at ϑ_{in} to the fiber face will be reflected under ϑ_2 within the fiber core. If $\vartheta_2 \geq \vartheta_{\text{c}}$ is satisfied, total internal reflection occurs, and the beam is transmitted through the fiber. Otherwise, fractions of the light are diffracted into the cladding and subsequently lost. A possible refractive index profile is the step-index profile where $n_{\text{core}} > n_{\text{clad}}$ is required to allow the total internal reflection.

Applying the limit case to this equation, thus using the critical angle $(\vartheta_2 \overset{!}{=} \vartheta_{\text{c}})$, results in the maximum acceptable angle for the incoupling to achieve guidance through the fiber:

$$\vartheta_{\text{ac}} = \arcsin\left(\frac{1}{n_0} \cdot \sqrt{n_{\text{core}}^2 - n_{\text{clad}}^2}\right). \tag{4.5}$$

In the two equations above, n_0 is the refractive index of the medium surrounding the fiber which is air or vacuum in many cases. Therefore, $n_0 \simeq 1$ which simplifies equation (4.5) to

$$\vartheta_{\text{ac}} = \arcsin\left(\sqrt{n_{\text{core}}^2 - n_{\text{clad}}^2}\right) = \arcsin(NA), \tag{4.6}$$

with the numerical aperture NA of the fiber. The numerical aperture is commonly given in the data sheet of the fibers and defined as $NA :=$ $\sqrt{n_{\text{core}}^2 - n_{\text{clad}}^2}$.

By their nature of having a small diameter and being made of glass, optical fibers are fragile and, therefore, feature several protective layers. Figure 4.2 shows the structure of an optical fiber and the different protective layers: The core and the cladding form the "active," i. e., the

Chapter 4

light guiding part of the fiber. The remaining three layers are added for robustness. Only core and cladding are manufactured from glass, often silica, and the coating is commonly a layer of UV-curable acrylate [84]. Strength member and jacket form an outer shell for the fiber where the strength member is used to absorb shear forces which otherwise would damage the fiber.
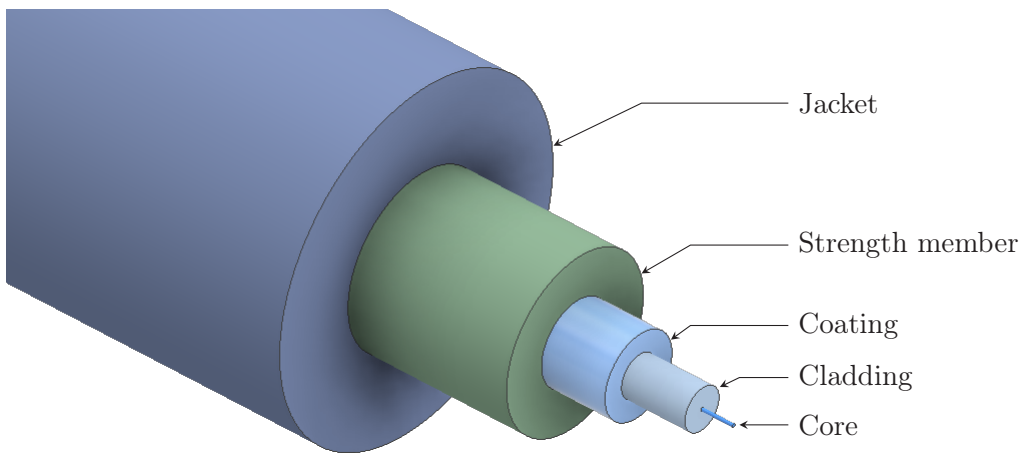
Figure 4.2: Overview of the layers of an optical fiber, drawn to scale for an outer diameter of 1 mm and a fiber as tested in section 6.2.1. Only the inner two layers (core and cladding) are relevant for the transmission of the fiber. The remaining layers are protective layers to reduce the risk of damage while handling the fibers.

4.2 Fiber types

There are several types of fibers available that are in use in different applications, e. g. single-mode fibers (SMFs), multi-mode fibers (MMFs), polarization-maintaining fibers (PMFs), and photonic crystal fibers (PCFs). Besides passive fibers, with the sole purpose of transmitting light, active fibers exist. These active fibers not only guide light as described in section 4.1 but can also have laser-active or non-linear media added to their core. Therefore, active fibers can amplify laser light or perform frequency conversions of the light coupled into the fiber [85]. Figure 4.3 shows

cross-sections of these fiber types and different geometries to achieve the polarization-maintaining properties for the PMFs. These geometries result in different ways to introduce the birefringence: Stress rods in the PANDA type (d), an elliptical core (e), and stress elements in a bow-tie configuration (f). This last configuration is also utilized to create polarizing fibers (PZFs), which feature a polarizing window and, thus, can be used to create in-fiber polarizers [86, 87]. Although PMFs are usually in the single-mode region, some in the multi-mode region exist [88, 89].

In the scope of the LISA optical bench and laser development, PMFs are the mainly considered fibers. PMFs feature drastically reduced polarization noise compared to SMFs, which show high polarization noise if these are subject to external disturbances, e. g. vibrations, and arise from coupling between the two polarization modes of the fiber. The coupling is induced by arising variations of the birefringence induced by external disturbances [90]. The reduction in PMF is achieved by deliberately increasing the birefringence of the fiber since this reduces the coupling between the two orthogonal polarization axes over the length of the fiber as the birefringence induces coupling between the polarization states such that it cancels over the so-called beat length [91].

4.3 Losses in fibers

Several absorption and scattering factors contribute to the attenuation of the transmission of light through an optical fiber. Depending on the wavelength range, the dominant factors are the multiphonon absorption (for longer wavelengths), the Urbach tail (for shorter wavelengths) and Rayleigh scattering in between [92]. The impact is often given as loss per unit-length, for fibers in units dB/km, and can be written in the typical way [92, 93]

$$\frac{P_{\text{out}}}{P_{\text{in}}} = \exp\left(-\alpha L/10\right) \iff \alpha = -10 \cdot \log\left(\frac{P_{\text{out}}}{P_{\text{in}}}\right) \cdot \frac{1}{L}, \qquad (4.7)$$

where α denotes the loss coefficient and L the fiber's length. Depending on the fiber type α is given in $\text{dB}\,\text{km}^{-1}$ or $\text{dB}\,\text{m}^{-1}$.
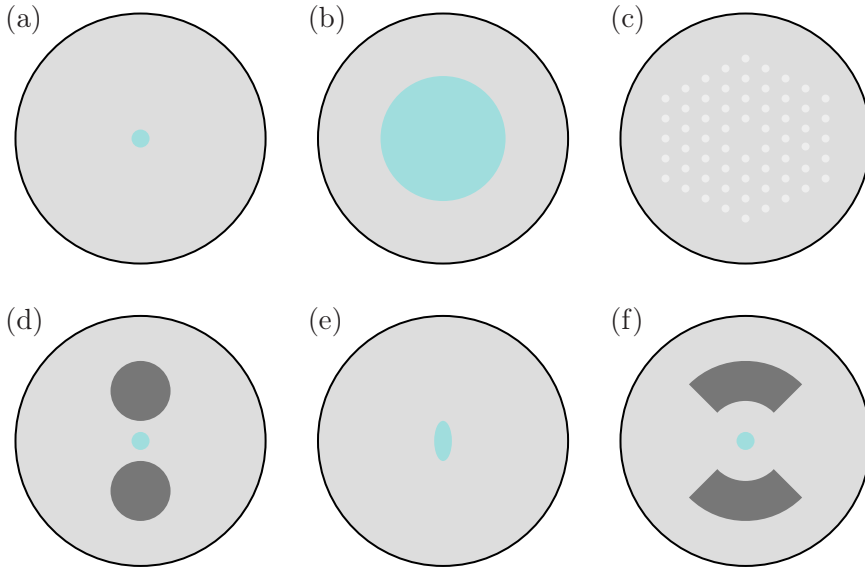
Figure 4.3: Cross-sections of different fiber types: (a) a single-mode fiber, (b) a multi-mode fiber, (c) a photonic crystal fiber, and (d-f) polarization-maintaining fibers in different configurations (PANDA, elliptical core, and bow-tie, respectively). Stress elements in the fibers are colored in dark gray, the claddings in gray, and the cores are depicted in cyan, except for (c) as the core of a PCF is defined by the air gaps around it, colored in light gray.

However, the aforementioned contributors are not the only factors attributing to the transmission losses: Fiber bending can lead to transmission loss [94, 95], and other sources of scattering can occur, like Mie scattering [96], Brillouin scattering [97], or Raman scattering [98]. All these loss contributions can be combined to obtain the total loss coefficient of the fiber:

$$\alpha_{\text{total}} = \frac{R_{\text{eff}}}{\lambda^4} + \alpha_{\text{OH}} + \alpha_{\text{IR}} + \alpha_{\text{UV}} + \dots \tag{4.8}$$

These contributions originate from different sources and depend on the wavelength transmitted through the fiber. Besides the Rayleigh scattering, these are, for example, absorption at hydroxyl ions α_{OH}, the infrared absorption α_{IR}, or absorption in the ultra-violet α_{UV} [92].

Relevant for this thesis are the Rayleigh scattering, in the form of backscat-
tering, and stimulated Brillouin scattering (SBS) as the driving factor for
the change of the fiber type for the PRDS. Although the power-levels in
the PRDS are low enough to not disturb by SBS the change was done for
development and implementation reasons [99].

Rayleigh scattering is an elastic scattering process and, thus, does not
induce a frequency shift but alters the direction of the scattered photon
[100]. In doing so, Rayleigh scattering induces power loss and phase
shifts within optical fibers. The scattering happens at variations in the
refractive, i. e., variations in the glass density, which are frozen into the
glass matrix during manufacture. These refractive index variations result
from the fiber's drawing process [101] and are shorter in their extent
than the wavelength of the light. The Rayleigh scattering loss can be
approximated using the following equation [102]:

$$\alpha_{\mathrm{R}} = \frac{R_{\mathrm{eff}}}{\lambda^4} \tag{4.9}$$

The effective Rayleigh scattering coefficient R_{eff} was determined experi-
mentally to be in the range $R_{\mathrm{eff}} = 0.6 - 0.8\,\mathrm{dB/km/\mu m^{-4}}$ by [102–104].
This equation shows that for longer wavelengths, the Rayleigh scattering
decreases. However, towards longer wavelengths, other effects increase
the absorption and, thus, transmission loss of the fibers, e. g. the infrared
absorption [92]. A possibility to reduce the contribution of Rayleigh scat-
tering is to use so-called hollow-core fibers [105] since this type of fibers is
based on an air-guiding core to remove the glass density fluctuations.

Brillouin scattering, on the other hand, can induce a frequency shift of
the light propagating through an optical fiber [106] as it is an inelastic
scattering process. Therefore, Brillouin scattering can induce phase noise
in the readout. In the development of the LISA OB and lasers, it was
deemed necessary to use fibers of a larger diameter than the fibers used
in the LISA Pathfinder (LPF) mission as these were too close to the
SBS threshold with a core diameter of about $6\,\mathrm{\mu m}$ [99]. The common

Chapter 4

approximation for the SBS power threshold P_th is given as (see e. g. [97])

$$P_\text{th} = 21 \frac{A_\text{eff}\alpha}{g_\text{B}} \tag{4.10}$$

where A_eff is the effective optical area and g_B the Brillouin gain. When exceeding this power level in the fiber, SBS will occur. SBS is the reason for changing the fibers within LISA to larger core diameters but not analyzed further within this thesis. The measurement setup introduced in chapter 5 cannot measure SBS.

4.4 Radiation induced fiber damages

If an optical fiber is not radiation-hard, exposure to ionizing radiation degrades its optical properties. These degradations can be attributed to three different mechanisms: Radiation induced attenuation (RIA), radiation induced emission (RIE), and radiation induced compaction (RIC) [107].

RIA is a measure of the decrease in transmission of an optical fiber as a result of ionizing radiation and can be utilized to detect ionizing radiation [108–111]. RIE describes radiation effects resulting in the emission of electromagnetic radiation of other wavelengths. This includes scintillation, which is also used to detect ionizing radiation [112]. Lastly, RIC takes changes in the structural properties of the fiber into account as a result of exposure to ionizing radiation [113]. Many applications of optical fibers exist to detect ionizing radiation utilizing these effects [114].

In the context of RIA and RIC, the formation of color centers within the optical fiber by ionizing radiation is important. Color centers are points within the fiber where passing photons are absorbed or scattered [73] and result from the ionization of atoms in the fiber lattice or local changes of the refractive index by deposition of ions or neutrons [115, 116]. Therefore, if the number of color centers in a fiber increases it may increase the backscattered signal, resulting in a worsening of the performance of the backlink.

4.5 Description of scattering

Throughout this thesis, we will use three ways to describe the backscatter signal of a fiber under test: the peak backscatter value (PBV), the mean backscatter value (MBV), and the calculated backscatter value (CBV). The PBV is obtained by extracting the highest backscatter value of a measured time-series. This value is necessary for the simulations of the LISA performance as the highest backscatter corresponds to the worst performance. Based on the speckle properties of the backscattered light [117], we obtain the MBV by transforming the measured time-series into a histogram and fit an inverse exponential distribution to the data. This speckle evaluation can also be used to estimate the size of the scatterers within the fibers, as shown by and explained in [118]. The last value, the CBV is obtained by calculating an expected peak value from the exponential distribution under a chosen limit. The following paragraphs show this for a simulated time-series and give an overview of the required calculus.
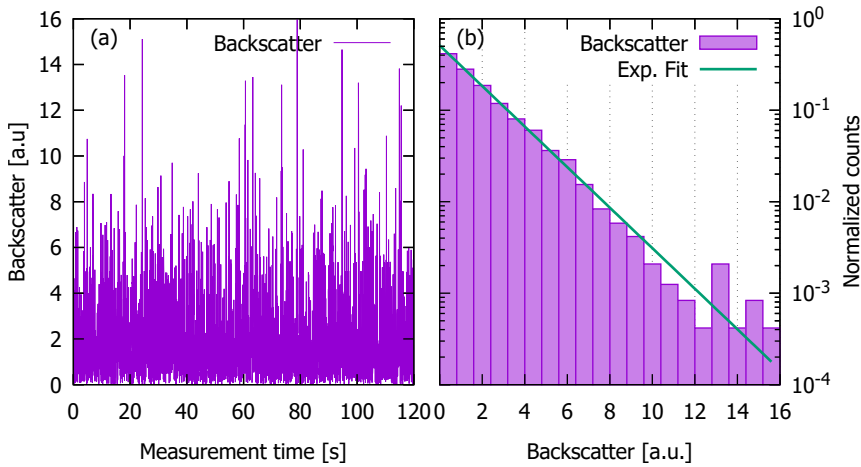
Figure 4.4: (a) Simulated time-series of the light backscattered from a fiber which shows a peak at about $79\,\mathrm{s}$. The peak backscatter in this time-series is $15.96\,\mathrm{a.u.}$ (b) Histogram created from this time-series. The histogram is normalized with the total number of samples in the time-series. Additionally, a fit of an exponential distribution is added which results in $\mu = 1.96\,\mathrm{a.u.}$

Chapter 4

Figure 4.4 (a) shows this simulated backscatter time-series. The simulations of the performance of LISA use the peak-value of such a measurement to describe the backscattering properties of the fiber [58]; in the plotted time-series the PBV is 15.96 a.u.. The statistically more robust approach in the form of the histogram is depicted in figure 4.4 (b). Fitting an exponential distribution of the form

$$f(x, \mu) = \frac{1}{\mu} e^{-\frac{x}{\mu}} \tag{4.11}$$

to the histogram results in the MBV which is the parameter μ of the distribution. $f(x, \mu)$ gives the probability of measuring the backscattered power x in such a distribution with the mean μ.

For the shown simulated data, this results in a MBV of 1.96 a.u.. This fit can then be utilized to obtain an expected value for the maximum expected backscatter, the CBV, using the cumulative distribution function (CDF) of the exponential distribution

$$F(x, \mu) = \int_0^x \frac{1}{\mu} e^{-\frac{x'}{\mu}} \mathrm{d}x' = 1 - e^{-\frac{x}{\mu}}. \tag{4.12}$$

By defining a limit $\mathcal{L} = 0 \dots 1$, a worst-case value of the expected backscatter can be calculated using the CDF:

$$CBV := BS_{\mathrm{max}} = \mu \ln \left(\frac{1}{1 - \mathcal{L}} \right) \tag{4.13}$$

Here, $\mathcal{L}$ describes the fraction of the mission duration in which the backscattered power shall not exceed the calculated maximum.

With $\mathcal{L} = 0.997$ (the equivalent of the 3-sigma value in the normal distribution) and the simulated example from above, this results in a CBV of 11.4 a.u. which is relatively close to the measured peak and could be used as a more robust value of determining the expected maximum backscatter.

5

Fiber Backscatter Experiment

This chapter shortly introduce the new backscatter experiment needed for measuring the fiber dynamics. We start with an overview of the experiment and apply equations from chapter 2 to reconstruct the backscattered signal. After that, we introduce the upgraded version of the backscatter experiment, which allows polarization-sensitive measurements. Subsequently, we characterize the measurement setup and perform some measurements and introduce the effect of a temperature modulation of the fiber under test. Lastly, we re-verify the linear dependence of backscattered power to the fiber length.

5.1 Purpose

The previous studies in [63, 119] found a linear fiber length-to-backscatter dependence and backscatter values acceptable for the LISA backlink, in that case, a backscatter of $4\,\mathrm{ppm/m}$. However, these experiments did not address possible influences to the backscattered power by environmental effects. The primary effect suspected to increase the backscattered power is the ionizing radiation in the space environment. Therefore, a new experiment to measure backscatter in optical was designed. This setup requires transportability to allow using it close to the radiation facilities needed for exposing the fibers under test to the ionizing radiation. The

proximity to the radiation source is desired to prevent annealing effects of the irradiated fibers [120, 121] from happening between the exposure and the performance measurement.

With some additions to the backscatter experiment, several other fiber-related effects besides the backscatter values can be observed, which is presented in the following sections and chapters.

5.2 Experimental setup
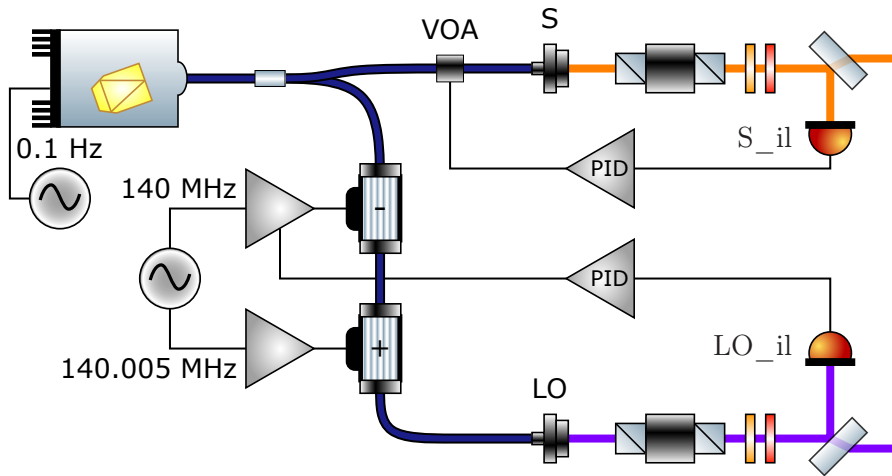
Figure 5.1: Laser preparation of the backscatter setup. A fiber-coupled laser is distributed into two beams (S and LO). LO is shifted in frequency by 5 kHz with respect to S by a pair of AOMs. Faraday isolators prevent the back-reflection of light coming from the interferometers. Polarization optics ensure the s-polarization of both beams. Two controllers are used in conjunction with two in-loop (_il) PRs to keep the amplitude sent into the interferometer stable.

The optical setup of the backscatter experiment is depicted in figures 5.1 and 5.2. The former shows the laser preparation and the latter the interferometer in a simplified schematic. A fiber-coupled NPRO Nd:YAG laser (Coherent Mephisto, $\lambda = 1064.5\,\mathrm{nm}$, $P_0 = 500\,\mathrm{mW}$) provides the light for the measurements. The necessary beam preparation is performed in fiber components. A fiber beamsplitter (Thorlabs PN1064R5A1) splits the incident beam into two parts: The signal-generating beam (S) in the upper
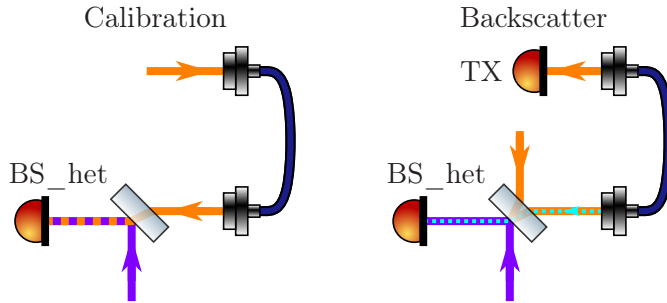
Figure 5.2: Simplified schematic of the calibration and backscatter measurements: In the calibration, S is transmitted in reverse through the fiber under test to align the LO to the fiber's output mode and obtain the heterodyne efficiency. In the backscatter measurement, S is transmitted through the fiber under test nominally, and the transmission is monitored. The backscattered light interferes with the LO and can be reconstructed from the heterodyne amplitude. The complete setup is depicted in appendix section A.1.2.

part of the figure drawn in orange in the free-beam path and the local oscillator (LO) in the lower part and colored in violet. The LO includes two AOMs to shift the frequency of the beam by 5 kHz with respect to S. This is achieved by utilizing diffraction into the positive and negative order, thus using up- and downshift type AOMs respectively (models SFO5177-T-M140-0.4C2G-3-F2P and SFO5178-T-M140-0.4C2G-3-F2P by Gooch & Housego). The up-/downshift configuration was chosen as these AOMs were available when the setup was built. A symmetric configuration with an AOM in both arms would be possible as well. The heterodyne approach is required to measure the low backscattered power (in the order of nW) and makes the measurement of the phase effects induced by the fiber possible which can be in the order of many wavelengths, as shown in later sections.

LO and S propagate in an anti-parallel configuration towards the recombining beamsplitter (all beamsplitters are BSW11 by thorlabs). Faraday isolators are placed after the fiber couplers to prevent reflections of the beams from the fiber coupler of the other beam since these would spoil the measurement. A polarizer and a half-wave plate clean the polarization of the beams and return these into the s-polarized state. An uncoated

fused silica component reflects a fraction of the incident beam to the power stabilization PR (S_il and LO_il). A PI-controller acts on an AOM to change the diffracted amplitude of the LO such that the signal on LO_il remains constant. In the case of S, the controller acts on an additional VOA (VOA, MMVOA-1-1064-P-6/125-3A3A-1-1-NO-WK by OZ Optics) to achieve power stabilization. PRs transform the optical signals into measurable voltages. The PRs consist of a large silicon photodiode (PC50-7 by FirstSensor, $d_{\text{active area}} = 7.98\,\text{mm}$) combined with a TIA. The TIAs are based on the AD8674 operational amplifier and feature feedback resistors in the range $R_{\text{TIA}} = 30\text{–}330\,\text{k}\Omega$ to obtain an average signal of about $5\,\text{V}$. Additionally, the TIAs also have capacitors in the range $C_{\text{TIA}} = 10\text{–}50\,\text{pF}$ in the feedback path to optimize the transfer function of the PR. All PRs are angled 5° out of plane to prevent back-reflections from spoiling the measurements.

The setup is operated in two modes: The "calibration mode" and the "backscatter mode." Operation in the former results in a measure of the interference quality. With this information, operation in the "backscatter mode" allows the measurement of the backscattered power.

5.3 Signal reconstruction

Using the voltage U_{cal} measured at BS_het in the calibration mode the heterodyne efficiency η at the recombining beamsplitter is calculated using equation (2.7) and given as

$$\eta = \frac{1}{(2R_{\text{TIA}}\mathcal{R}\rho\tau)^2} \cdot \frac{(U_{\text{cal}}^{\text{AC}})^2}{P_{\text{LO}}P_{\text{cal}}}. \tag{5.1}$$

Here, $\mathcal{R}$ describes the responsivity of the PR, and R_{TIA} is the resistance in the feedback path of the transimpedance amplifier. The properties of the recombining beam splitter are ρ, and τ, reflectivity and transmittivity, respectively. P_{LO} and P_{cal} are the optical power of LO and calibration beam, respectively, propagating to the recombining beam splitter. Lastly, $U_{\text{cal}}^{\text{AC}}$ is the AC part of the measured calibration signal U_{cal}.

Measuring in the backscatter mode yields another voltage U_{bs} which contains the searched-for backscattered power. To obtain the backscattered power, a similar equation is used:

$$P_{\mathrm{bs}} = \frac{1}{(2R_{\mathrm{TIA}}\mathcal{R}\rho\tau\tau_{\mathrm{pp}})^2} \cdot \frac{(U_{\mathrm{bs}}^{\mathrm{AC}})^2}{P_{\mathrm{LO}}\eta} \ . \tag{5.2}$$

Here, an additional beamsplitter in the path of the backscattered signal (which is not shown in figure 5.2 but in the full interferometric setup in appendix section A.1.1) is attributed to by adding the factor τ_{pp} as the backscattered signal is transmitted through it.

For better comparability between the different measurements, the backscattered power is divided by the power (P_{TX}) of the signal beam that is transmitted through the fiber. This is done to remove effects from differences in the coupling of light into the fiber between different measurements. This is possible because the transmitted power in a low-loss regime is roughly the same as the power coupled into the fiber. Thus, the relative backscatter is given by

$$\beta = \frac{P_{\mathrm{bs}}}{P_{\mathrm{TX}}} \ . \tag{5.3}$$

In appendix section A.2, we derive the calculus required for the error estimation of the backscattered power.

5.4 Upgraded backscatter experiment

After the first radiation campaign (see section 6.1), the setup was upgraded to enable polarization-split measurements of the backscattered power. The upgrade was implemented because other experiments found polarization-driven problems [42, 122]. To do so, polarizing beam splitters, type PBSW-1064 by Thorlabs, were added to the readout ports and the non-polarizing beamsplitters were replaced by BSW41-1064 from Thorlabs for their equal splitting in both linear polarization states. With a second PR in each output port, both s- and p-polarized contributions can be measured simultaneously. Figure 5.3 shows the laser preparation of the upgraded setup, which includes an additional quarter-wave plate
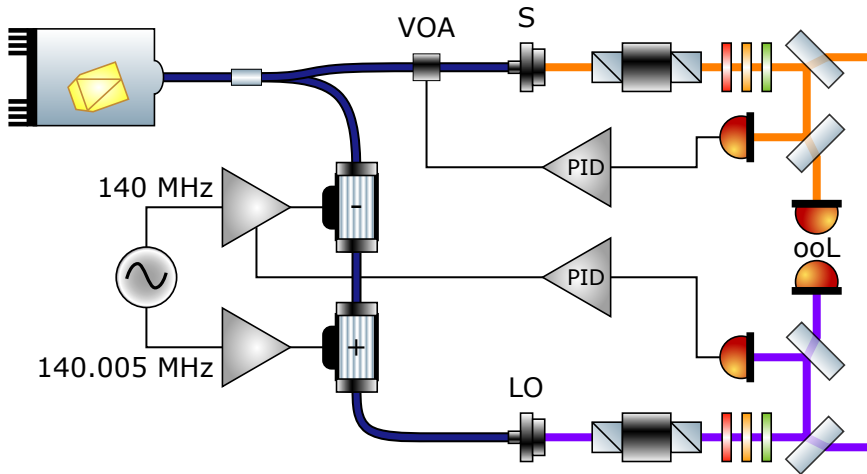
Figure 5.3: Laser preparation of the upgraded setup: The polarization control for both beams was updated such that the beam's polarization is cleaned first after the Faraday isolator by a polarizer. After that, a pair of quarter- and half-wave plates allows adjustment of the polarization to arbitrary states. Furthermore, the amplitude stabilization's out-of-loop (ooL) measurements were moved to the power pick-off by adding another beam splitter.

in the polarization stage for increased adjustability of the polarization of the respective beam. These are used to counteract the appearance of circular-polarized contributions since the beams propagate through the wave plates under a small angle. The tilts of the waveplates are introduced to prevent back-reflections from spoiling the measurements. Figure 5.4 shows a simplified overview of the optical setup after the beams are prepared. The setup utilizes three interferometers: the primary interferometer to measure the backscattered power (BS_s, BS_p), a secondary interferometer measuring effects on the transmitted light (TX_s, TX_p), and a reference interferometer (Ref_s, Ref_p). In addition, the upgraded setup features fiber collimators in a rotatable mount to improve the alignment of the fiber's slow axis (indicated by the key on the connector) to the polarization axis of the incoming beam. This improves the polarization stability along the fiber and reduces effects induced by a mismatch of the fiber axis to the polarization state of the incoupled beam.
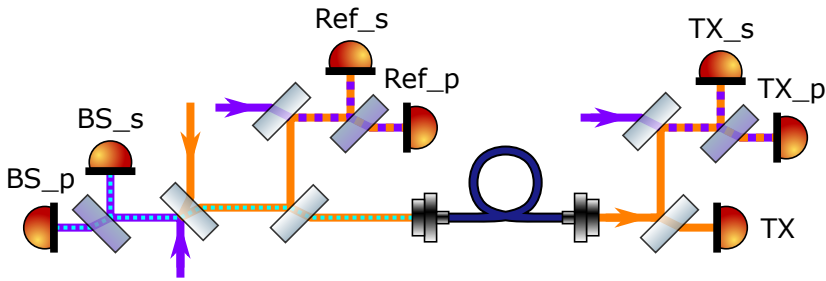
Figure 5.4: Simplified overview of the measurements done in the up-graded backscatter setup: The measurement is performed in three interferometers: the backscattered signal is measured with the PRs BS_* and transmission effects with the PRs TX_*. In addition, a reference interferometer is set up before the light is injected into the fiber, and the transmitted power is monitored with the PR TX. The complete optical setup is shown in appendix section A.1.2.

5.5 Characterization

5.5.1 Data acquisition

The data acquisition is performed using one (two in case of the upgraded setup) USB-1608FS-Plus-OEM by measurementComputing [123]. These feature eight channels each, with a 16 bit, simultaneous data acquisition. The acquisition is performed at $50 \, \text{kS} \, \text{s}^{-1}$, and the acquired data is demodulated at the heterodyne frequency using the IQ-demodulation described in section 2.3. Afterwards, an averaging filter is applied to achieve an effective sampling rate of $25 \, \text{S} \, \text{s}^{-1}$ by averaging over 2000 samples. In total, the data acquisition (DAQ) system returns three values for each channel: The demodulated heterdoyne phase and amplitude, and the averaged DC value.

The characterization measurement was performed based on recommendations from [124]: The DC performance is measured while pulling all channels to ground, and the AC performance is measured while applying an AC signal. For better comparability, all channels are connected to the same input signal, which allows obtaining an estimate of the excess noise by calculating the difference between two channels; this is a so-called "split measurement." Figure 5.5 shows the noise spectral density of this

split measurement for a single channel and the difference between two channels on one of the DAQ boards. These spectra and all other spectra in this thesis are calculated using the LPSD algorithm (see [125]). For frequencies above 1×10^{-3} Hz the observed noise is lower than specified in the datasheet [123], which is given as

$$1.52 \, \text{LSB}_{\text{RMS}} \hat{=} 1.52 \cdot \frac{20 \, \text{V}}{2^{16}} \simeq 0.46 \, \text{mV}$$
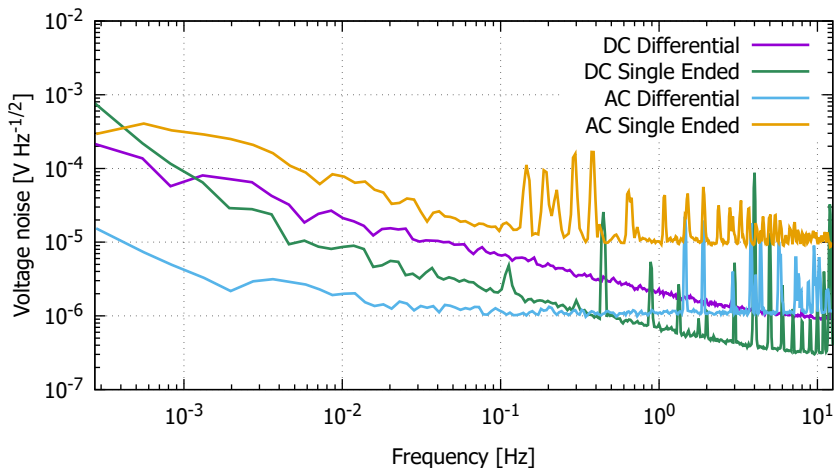
Figure 5.5: DAQ DC and AC noise in single-channel and differential configuration: The differential measurements show that for both AC and DC signals, the DAQ reaches µV-level performance. Several peaks in the noise curve are visible at different frequencies but these do not break the specified performance. The single-ended AC measurement is likely limited by the signal quality of the signal generator's output.

The spectral density in figure 5.5 also reveals several peaks in the range above 0.1 Hz, which are likely a result of the DAQ board as these peaks are canceled in the difference. The highest of these peaks is at about 4 Hz and nearly reaches the noise level specified in the datasheet. It is important to note that the noise can partially originate from the function generator providing the 5 kHz signal in the AC case.

With the AC signal, an evaluation of the phase performance is possible. This is shown in figure 5.6. The single-ended noise performance shows a strong drift, resulting from not-synchronized clocks between the signal

generator and the DAQ. The more interesting information lies in the differential signal, as this reveals the performance of the DAQ. This shows that the DAQ combined with the software phase meter (see appendix F) fulfills the 1 pm-requirement of the backlink and thus is capable of being used in such an experiment.
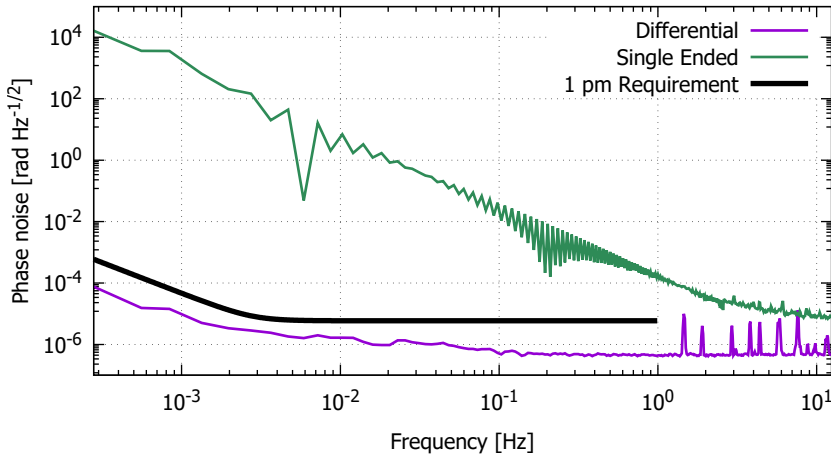
Figure 5.6: Phase noise of the DAQ: In the single-ended measurement, a strong phase drift is visible in the single-ended measurement, which originates from the function generator used to create the signal. The DAQ's performance is given in the differential measurement, which shows that the system fulfills the 1 pm-requirement of the LISA backlink.

5.5.2 Cross-talk and dark noise

The usage of two AOMs driven at $140\,\text{MHz}$ and $140\,\text{MHz} + 5\,\text{kHz}$ results in cross-talk between the two driving signals synthesized from the same chip and, thus, in a spurious beat note at the heterodyne frequency in the LO. Hence, the measured amplitude resulting from this cross-talk gives the lowest certainly resolvable backscatter signal.

To obtain this lowest measurable value, only the LO was allowed to enter the respective PRs. Assuming a heterodyne efficiency $\eta = 1$, as the interference happens within the AOMs, and using equation (5.2) allows calculating the lower bound of measurable backscatter. Figure 5.7 shows the time series of a cross-talk and a dark noise measurement in the primary

interferometer. The measured signals are transformed into a backscatter equivalent value (in ppm). The backscatter equivalent signal of the
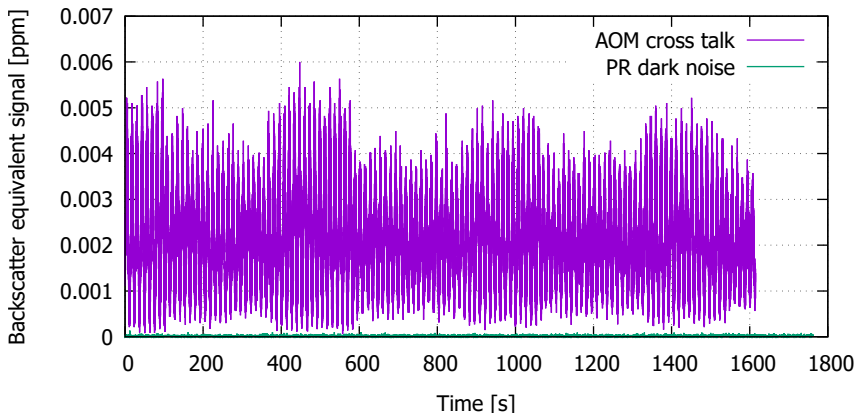
Figure 5.7: Cross-talk measurement of the PR in the primary interferometer: The measured signal is transformed into a backscatter equivalent value in ppm. In addition, this plot includes the dark noise limit of the signal, which is barely visible as it is close to the zero line.

dark noise is in the order of 10^{-5} ppm and lower and, as such, negligibly low. The peak of the backscatter equivalent signal of the cross talk is at 0.006 ppm over the measurement time and oscillating. In conclusion, this imposes a lower limit of the observable backscatter at 0.01 ppm, which is not limiting the measurements.

5.5.3 Amplitude stabilization

As the measurements of the backscattered power and its transformation into ppm-based values are dependent on the optical powers involved, it is advantageous to have relatively stable optical powers. Therefore, an amplitude stabilization was implemented into both versions of the backscatter setup. Depending on the beam, the stabilization is realized by changing the amplitude of the AOM driving signal (for the LO) or the transmission through the VOA (for the S beam). This results in differences in the response function of the stabilization systems, i. e. the stabilization of the S beam has a lower unity gain frequency because of
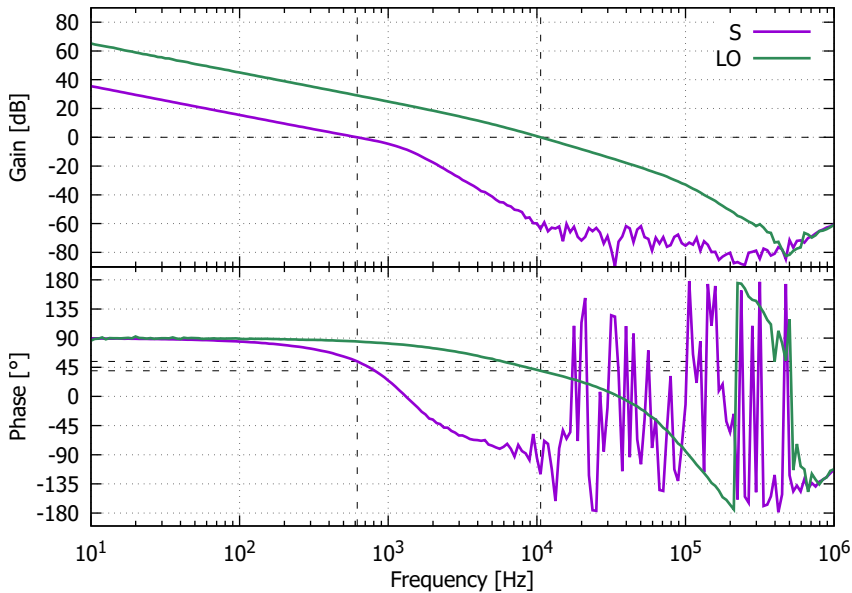
Figure 5.8: Bode plot of the open-loop transfer function of the amplitude stabilizations of the two beams. The dashed lines depict the unity gain frequencies. These are at 618 Hz and 10.6 kHz, respectively. Extending these lines into the phase plot shows the phase margins at 54.1° and 39.6°.

the use of a piezo mirror in the VOA. Figure 5.8 shows the measured transfer functions of the implemented stabilization systems in a Bode plot and reveals the unity gain frequencies at 618 Hz and 10.6 kHz for the S beam and the LO, respectively. The resulting phase margins of 54.1° and 39.6° and the passage of unity gain with a $1/f$-slope show that both stabilization systems are stable.

Figure 5.9 shows the power spectral densities of both stabilization systems, for in-loop and out-of-loop measurements. This shows that the power noise is drastically reduced, which allows a robust conversion of power values to ppm-values using the transmitted power. In the frequency range above 1 Hz, this also reveals that the measurement is limited or close to being limited by the DAQ. Observing the time-series of such a measurement shows that the power fluctuations are reduced from 7 % to only about 0.01 % which equals a reduction of about four orders of magnitude. This is depicted in figure 5.10.

Chapter 5
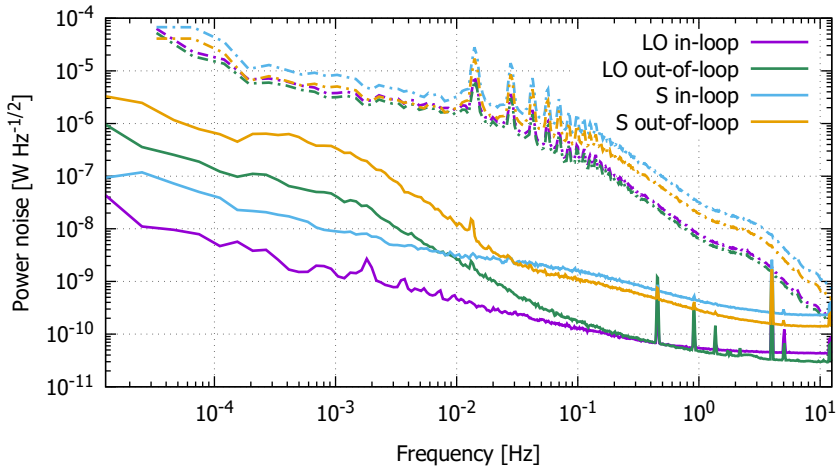
Figure 5.9: Power spectral densities of the power in the two beams. The solid lines show measurements with active stabilization and the dash-dotted line without amplitude stabilization.
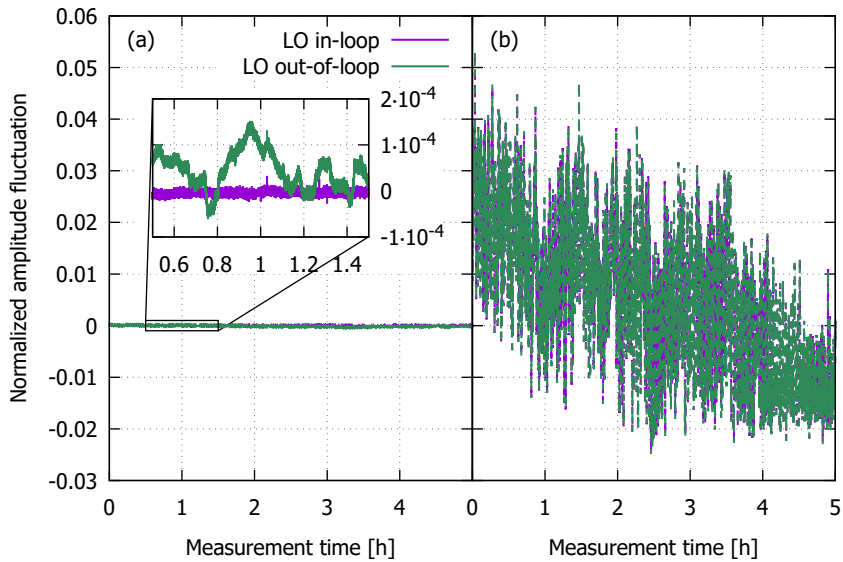
Figure 5.10: Time series comparing the amplitudes with (a) and without (b) stabilization: This example shows the data for the amplitude stabilization of the LO and shows that the fluctuations in the unstabilized case are about 7 % and with the stabilization active reduced to about 0.01 % (and in-loop even lower).

5.6 General measurements

The time series of a typical backscatter measurement is shown in figure 5.11 (a). This measurement is performed using a Nufern PM1060L fiber and shows a fluctuating behavior of the backscattered signal over time. Therefore, a measurement time of several minutes is necessary to prevent that the measurement remains entirely in a low backscatter regime and, thus, remaining significantly lower than the actual peak value. This is also visible in figure 5.11 (a): The first half features a significantly lower peak than the second half of the measurement. To address
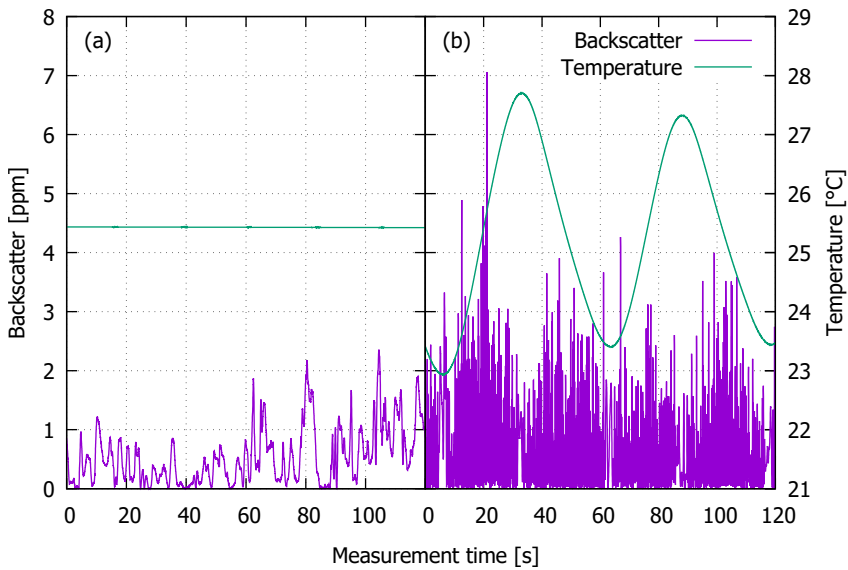
Figure 5.11: Time-series of two backscatter measurements of the same Nufern PM1060L fiber: Part (a) shows a measurement of a fiber in a normal laboratory environment and part (b) shows a measurement with activated temperature modulation. In the maxima and minima of the temperature the rate of change in the backscattered signal is lower.

this a modulation of the laser frequency was implemented, to change the interference condition between different scattering points along the fiber, as well as a temperature modulation of the fiber under test. However, the frequency modulation was dropped after the first radiation campaign as the effect of the temperature modulation was found to be stronger

and obscuring effects of the frequency modulation. Appendix section A.3 gives some information about the effects of the frequency modulation.

5.7 Temperature modulation

With the measurement approach described in the previous section, it is possible to remain in a condition where the backscattered power is low. This is problematic for estimating the maximum expected backscatter. Therefore, a temperature modulation of the fiber was implemented to accelerate the change of the interference condition between scattering points within the fiber and, thus, reduce the time required to obtain a reasonable estimate of the worst-case backscattered power which is crucial for the radiation campaigns. Comparing both parts of figure 5.11 shows the faster changing of the backscattered signal with the activated temperature modulation.

For the temperature modulation, a DA PowerCool Series DA-160-24-02 thermo-electric assembly by Laird™ [126] with a PR-59 temperature controller [127] was used. The fibers we mounted loosely to aluminium spools. The "loose" mounting was chosen to reduce the influence of induced mechanical stress. Thermally-induced mechanical stress hinders this mounting approach as it might cause an additional contribution to the backscattered power, which is not relevant for LISA. Nonetheless, this approach was chosen for its simplicity in handling the fibers.

Figure 5.12 (a) shows the prepared thermo-electric assembly with a mounted fiber spool. Later on, an approach without the aluminium spool was also used, as shown in figure 5.12 (b). The second mounting approach allows measuring the temperature coupling coefficients of the tested fibers without influences due to mechanical stress induced by the spool.

Overall, the inclusion of the temperature modulation results in a more conservative estimate of the backscattered power to be expected due to the mechanical stress. Furthermore, this approach also enables an additional way of evaluating the obtained data using speckle properties. This
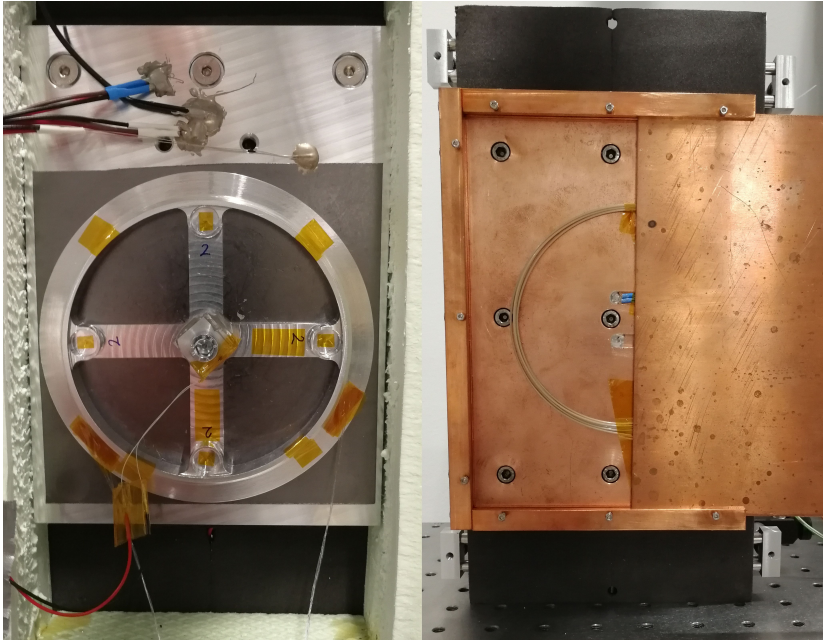
Figure 5.12: Peltier setups used for the temperature modulation: The left photograph (a) shows the way of temperature modulation during the radiation campaign and the right photograph (b) shows a way of modulating the fiber's temperature without adding mechanical stress.

approach is depicted in figure 5.13 for the time-series of figure 5.11 (b) and explained in more detail in section 4.5.

5.8 Length dependence - re-verified

The length dependence of the backscattered power in [119] was measured destructively by cutting the tested fiber shorter. The availability of many fibers of two meters length for the radiation tests with a fiber mating sleeve in the middle (see section 6.2) allowed to repeat such a measurement in a non-destructive way: by adding fiber after fiber, the total transmission length light was extended. The measurements were performed with several 2 m Nufern PM1060L fibers.

Figure 5.14 shows the result of several such measurements. The linear increase of the backscattered power with the fiber length is visible.

Chapter 5

Furthermore, the measurements can also be used to obtain a reflection coefficient for the fiber's face and the mating sleeves by fitting the data to the following equation

$$P_{\text{bs}} = r_{\text{bulk}} \cdot l + r_{\text{ms}} \cdot n_{\text{ms}} + r_{\text{face}}. \tag{5.4}$$

The factors r are the different reflectivities involved: r_{bulk} the resulting reflectivity per meter caused by the scattering within the fiber bulk, r_{ms} the reflectivity of the mating sleeves used to connect the fibers and r_{face} the reflectivity of the fiber's face used to couple the light into the fiber. The measurements are shown in figure 5.14, and the result of the fit using the highest backscatter values at each step is given in table 5.1. These values are lower than in the radiation measurements, but this is expected as these measurements were done without the temperature modulation.
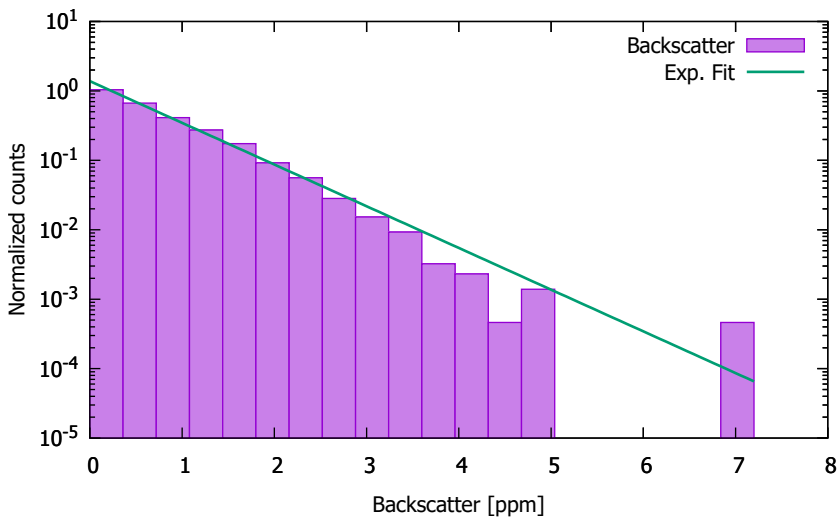
Figure 5.13: Typical histogram depiction of a backscatter measurement. The shown data origins from the measurement shown in figure 5.11 (b). The inverse exponential fit results in a mean value $\mu = 0.723$ ppm. The gap between about 5 ppm and the maximum indicates that values close to the maximum are relatively rare. Comparing figure 5.11 (b) to the simulated time-series (figure 4.4) shows that during the extrema in the temperature, the backscatter is relatively stable and low, which can be a reason for the low number of higher values.

Table 5.1: Fit results for the length dependence measurements when using Nufern PM1060L fibers

Parameter	Fit result	Comment
r_{bulk}	$0.85 \pm 0.06 \, \text{ppm/m}$	Reflectivity resulting from scattering in the fiber bulk
r_{ms}	$0.16 \pm 0.10 \, \text{ppm}$	Reflectivity of the mating sleeves
r_{face}	$0.85 \pm 0.26 \, \text{ppm}$	Reflectivity of the fiber face (APC)
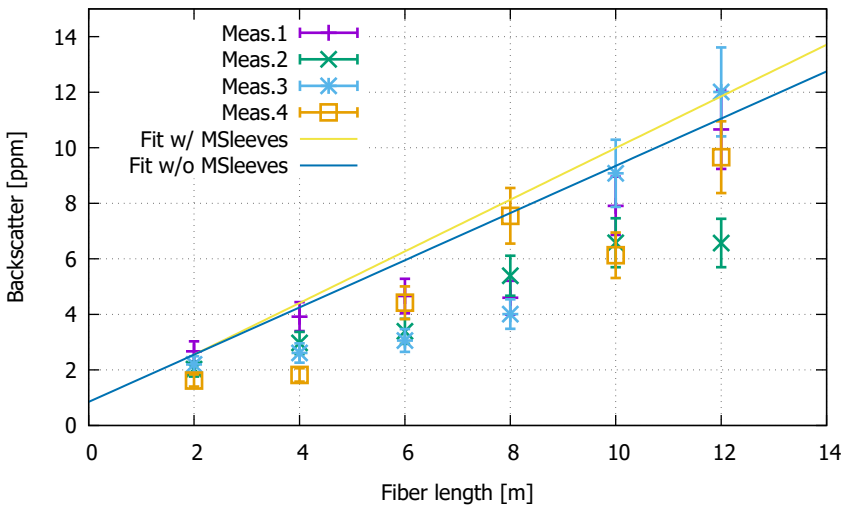
Figure 5.14: Measurements for the length dependence of the backscattered power: Two different fits are depicted, one including the mating sleeves and the other without. The fits were performed with the highest value for each combined fiber length in both cases. The values for 6 m fiber were excluded from the fit.

6

Backscatter Measurements under Radiation

In this chapter, we present the results of the backscatter measurement after the fibers were exposed to ionizing radiation. We present these measurements for four different types of fibers that were radiated in two radiation campaigns.

6.1 First radiation campaign

The first radiation campaign tested two different fiber types: a polarization-maintaining fiber (PMF) and a polarizing fiber (PZF). The tested PMF was the SM98-PS-U40D by Fujikura, and the PZF was the HB1060Z by Fibercore. This type of PMF is a heritage of LPF [30] with a minor difference, in the supplier of the UV acrylate coating [Fujikura, personal communication, November 5, 2018], while the PZF is an interesting alternative due to its polarizing properties. Being heritage of LPF, the PMF by Fujikura was intended for usage in the backlink if the performance would not degrade under exposure to ionizing radiation in levels representative for LISA.

As for the ionizing radiation, exposure to gamma radiation and neutrons was chosen due to better availability than protons. The exposure was performed at the Fraunhofer INT with a Co-60 source for the gamma radiation and a Thermo-Fischer D-T fusion neutron generator [128, 129].

With a worst-case assumption for the shielding of the fiber against ionizing radiation of 1 mm Al-equivalent shielding, the expected exposure over the extended mission lifetime a total ionizing dose (TID) of $0.63\,\mathrm{kGy}$ is expected. In terms of protons a flux of $1.08 \times 10^{12}\,/\mathrm{cm}^2$ is expected [72]. In this campaign, the original optical setup of the backscatter experiment as of section 5.2 was used.

To generate a larger dataset, several fibers of each type were tested at different levels of exposure up to the exposures stated above and beyond that. Table 6.1 gives an overview of the tested exposures. The exposure values in the neutron case are a result of an error in [130] and were anticipated to be about twice as high. Nonetheless, the expected dose for the extended mission duration was surpassed. The results of these measurements have also been published in [131]. Additional points are presented in this thesis, though. One of the tested PMFs was damaged during the measurements and is excluded from the evaluation presented in this section. However, the results of the broken fiber are presented in appendix section A.4.

Table 6.1: Tested exposures in the first radiation campaign as factors compared to the target exposures.

Radiation type	Exposure levels [%]						
Gamma	10	20	50	100	200	300	814
Neutrons	5.8	11.7	29.2	58.3	116.7		

6.1.1 Fujikura SM98-PS-U40D

The backscatter measurements of the Fujikura fibers are shown in the following figures: Figure 6.1 depicts the results in the peak-value description (i. e. the PBV), which is used for the performance evaluation of the backlink; this figure also includes transmission measurement done during the performance evaluation. On the other hand, figure 6.2 shows the result of the speckle description, the mean value from the inverse exponential fit (i. e. the MBV).
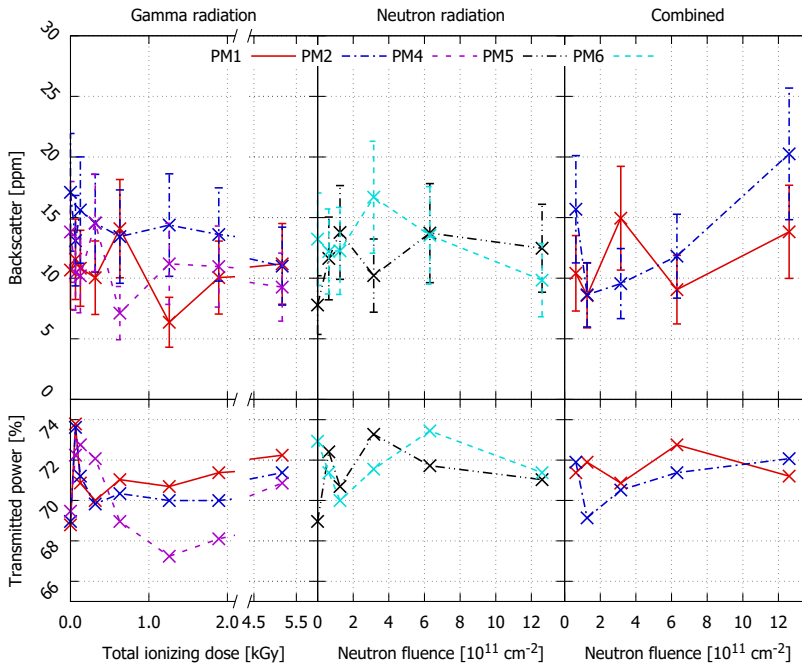
Figure 6.1: Results of the radiation measurements using the Fujikura SM98-PS-U40D fibers: The measurements show no significant increase of the PBV over the increasing exposure to either type of ionizing radiation. Furthermore, the transmission through the fibers also remains constant, within the limits of the manual fiber alignment to the measurement setup. The figure originates from [131].

Over the three measurement sets, the fibers show no significant increase in the backscattered power, which is shown in figure 6.1. Furthermore, the transmitted power remains constant, within the limits of the manual alignment of the fibers to the measurement setup, which is shown as the percentage of power transmitted to power sent to the fiber. The transmission of about 70 %, thus, includes the coupling efficiency into the fiber. The highest observed PBV for the Fujikura fibers is 20.3 ± 5.4 ppm. Taking the sum of the measurement and the error range as a worst-case estimate, this equals to about 6.4 ppm/m.

The inverse exponential fits result in MBVs in the range of around 1 to 3 ppm for the measurements with the highest value of 3.09 ppm and a confidence interval of 2.95 to 3.24 ppm. Like the peak measurements, no

Chapter 6
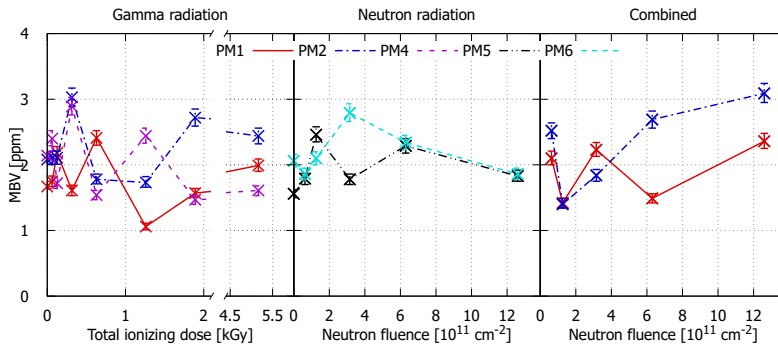
Figure 6.2: Results of the inverse exponential fit for the Fujikura SM8-PS-U40D fibers. The measurements show no significant change of the MBV over the increased exposure and lay in the range of about 1 to 3 ppm.

significant increase over the increasing exposure was observed. Therefore, both evaluations show that neither the PBV nor the MBV changed significantly after the fibers were exposed to increasing levels of ionizing radiation.

6.1.2 Fibercore HB1060Z

The backscatter measurements with the Fibercore fibers are depicted in the following figures in the same way as for the Fujikura fibers in the section before: Figure 6.3 shows the PBVs with the transmission measurements, and figure 6.4 shows the speckle description, i. e. the MBVs.

The Fibercore PZFs also show no significant increase in backscatter over the increasing exposure to ionizing radiation in the three sets of measurements. However, these fibers show a significantly higher backscatter values than the Fujikura fibers with the highest PBV over the measurements at 52.3 ± 16.2 ppm which equals to 17.1 ppm/m under the same assumption for the worst-case estimate as before.

The higher values are also expressed in the results of the fits in the inverse-exponential view. Here, the highest value of the MBVs is 12.09 ppm with a confidence interval of 11.55 to 12.67 ppm. The range of results is also
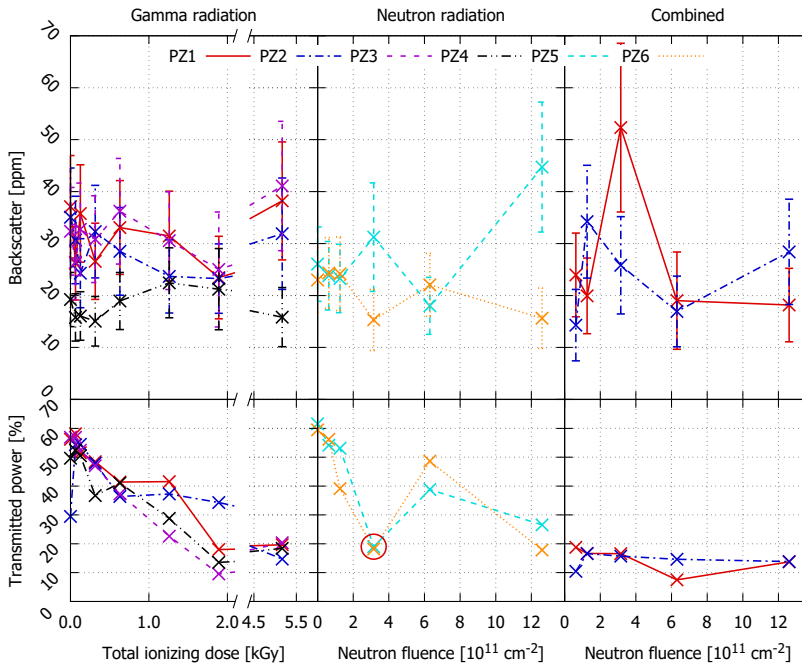
Figure 6.3: Results of the radiation measurements using the Fibercore HB1060Z fibers: The measurements show no significant increase in the PBV. However, the transmission degrades significantly over the increasing exposure. Excluding the measurement encircled in red for the neutron measurements, the decrease in transmission is similar to the decrease for the gamma case. The fibers in the combined case show only a slight decrease but these fibers were at the start already exposed to the maximum gamma level. The figure originates from [131].

larger compared to the Fujikura fibers ranging from about 2.5 ppm to the maximum value given before. Although higher, the backscattered power remains constant with the increasing exposure to ionizing radiation, both in peak and mean values, similar to the Fujikura fibers from the previous section. Nonetheless, the Fibercore HB1060Z fibers bear another problem: The measurements shown in figure 6.3 clearly depict that these fibers are not radiation-hard as the transmission degrades significantly with the increasing exposure to ionizing radiation. Both types, gamma and neutron exposure, show about the same decrease in transmission per exposure (excluding the marked measurement error).

Chapter 6
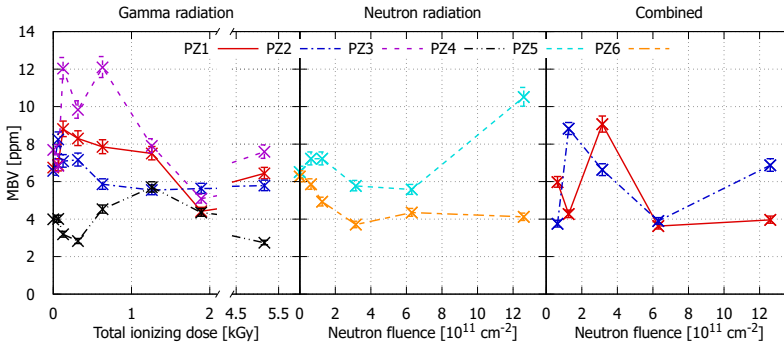
Figure 6.4: Results of the inverse exponential fit for the Fibercore HB1060Z fibers: Over the increasing exposure to ionizing radiation, the MBV is not increasing significantly. However, the amount of backscatter and its variance are higher than the Fujikura fibers' results.

6.2 Second radiation campaign

A second radiation campaign was needed as the laser and optical bench development concluded that a fiber with a larger core diameter than the Fujikura SM98-PS-U40D is required. Otherwise, the performance would be limited by SBS [99]. The fiber candidate chosen is the PM1060L by Nufern, which offers a core diameter of 8.5 μm. Additionally, the FUD-3561 by Nufern was tested since this fiber type closely resembles the active fiber of the fiber amplifier used in the laser head. However, the FUD-3561 is a passive fiber and features a core diameter of 10.5 μm. Both fibers are polarization-maintaining.

If the performance of the PM1060L is acceptable, a change of the backlink fiber is advantageous. The change of the backlink fiber would reduce the required effort to develop the FIOS for LISA as only one type of FIOS is then required. A reduction in backscatter can be expected as a larger core diameter reduces the scattering loss at the core-cladding interface [132].

For this second radiation campaign, ESA officials updated the spacecraft shielding assumption to 3 mm Al-equivalent shielding between the fiber and the space environment [L. Mondin, personal communication, September 2, 2019]. This amount of shielding results in an expected

exposure of $0.2\,\mathrm{kGy}$ TID or $1 \times 10^{10}\,\mathrm{protons/cm^2}$ at $60\,\mathrm{MeV}$. For these tests, ESA organized the proton radiation at the Cyclotron Resource Centre (at UCLouvain). Consequently, tests were performed with exposure to gamma radiation and protons. Following the COVID-19 outbreak, the proton part of this test was reduced to only the anticipated 100 %-level. The fibers were shipped to the radiation facility, irradiated, and shipped back for the performance measurements. In consequence, this was a de-risking approach. Originally it was planned to prepare a correlation between the two measurement sets to be able to test only with gamma radiation in the future.

The measurements were performed with the upgraded version of the backscatter setup as of section 5.4. Although the upgraded setup allows for polarization-dependent measurements, the following result section will focus on s-polarized light, which is the primary polarization state on the LISA OB. An in-depth analysis regarding polarization effects is given in section 7.1.

Table 6.2: Tested exposures in the second radiation campaign, relative to the target exposures. The proton measurements were reduced to just the 100 %-level as consequence of the outbreak of COVID-19

Radiation type	Exposure levels [%]				
Gamma	100	200	300	500	5000
Protons (planned)	50	100	200		

6.2.1 Nufern PM1060L

The gamma radiation measurements with the Nufern PM1060L fibers are depicted in figure 6.5. The left-most part of this figure shows the results of the reference spool "Ref." which was not radiated. The remainder of figure 6.5 shows the different configurations tested in the measurements: bare fibers, fibers with a splice connection along its length, and fiber pairs with a mating sleeve in the middle. These measurements show that the backscattered power remains constant, as observed in the previous radiation campaign. Although the transmission measurements in the bare

Chapter 6
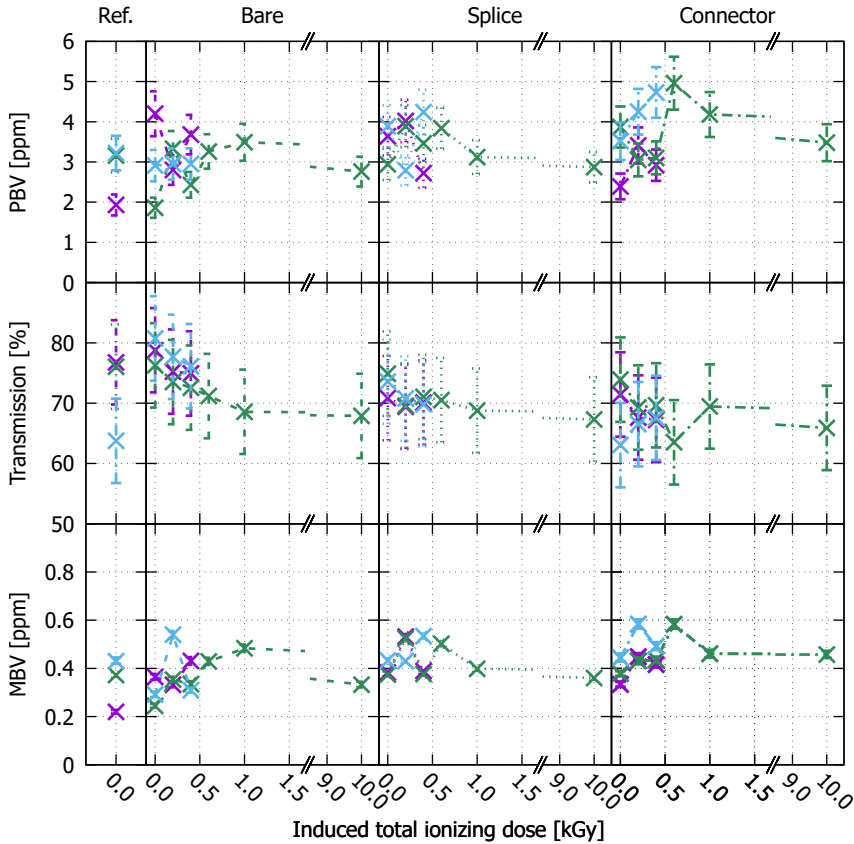
Figure 6.5: Results of the backscatter measurements with the Nufern PM1060L fibers: From top to bottom, the different properties of evaluation are shown: the PBV, the transmission, and the MBV. The fibers are grouped into the respective configurations (bare, spliced, and connectorized), also depicted in the different dash styles. The colors distinguish different specimens of the same configuration. For the leftmost column, the reference spool, each color depicts a different configuration correlated to the dash style. The reference spool was not exposed to radiation.

The measurements show that the backscattered power is not changing significantly over the increasing exposure to gamma radiation; this is valid for both PBV and MBV. The measurements in the bare configuration indicate an increase in attenuation over the increasing exposure. However, taking the remaining configurations and the reference spool into account, one concludes that the transmitted power remains constant within the measurement error.

Table 6.3: Measured PBVs in the different configurations for the Nufern PM1060L fibers for both radiation types; all values in ppm. The measurements show that a splice connection or a mating sleeve along a fiber connection adds a contributor to the backscattered signal.

Exposure	Bare	Splice	Connector
Gamma	4.29 ± 0.57	4.83 ± 0.64	4.96 ± 0.66
Proton	4.31 ± 0.57	4.01 ± 0.53	5.68 ± 0.76

fiber configuration indicate an increase in attenuation over the increasing exposure, it can be concluded that the transmission of these fibers remains constant over the tested dose since the fibers in the two other configurations show no increase in attenuation and the measurement errors of all measurements in the bare configuration overlap.

The highest PBVs observed over these measurements in the different configurations are assembled in table 6.3. The highest PBV observed for all tested configurations is 5.68 ± 0.76 ppm, significantly lower than the backscatter values observed while measuring the Fujikura fibers. Applying the previous way of generating a worst-case assumption, this equals a backscatter of about 1.6 ppm/m.

The bottom row of figure 6.5 shows the results of the measurements in the speckle view, thus, depicting the MBVs. This part of the figure also reveals no significant change in the backscattered power over the increased exposure to gamma radiation. So both, the PBVs and the MBVs, show that the backscattered power remains constant over the increasing exposure to gamma radiation.

Table 6.4 contains the averages of the observed MBVs. Applying equation (4.13) to these values, with the same limit as in section 4.5, results in CBVs lower than those in table 6.3. These CBV are given in brackets in table 6.4. However, using the peak values of the speckle evaluation results in lower deviations, similar to those in section 4.5, e. g. the MBV belonging to the connector-value in table 6.3 is 0.584 ppm which results in a CBV of 3.39 ppm.

The results of the measurements after the proton irradiation are depicted in figure 6.6. This shows that the backscattered signal remains constant

Chapter 6

Table 6.4: Average values of the observed MBVs for the different configurations and exposures for the Nufern PM1060L fibers. In brackets the resulting CBVs following equation (4.13) are given. All values are in ppm.

Exposure	Bare	Splice	Connector
Gamma	0.38 (2.21)	0.44 (2.56)	0.47 (2.73)
Proton	0.41 (2.38)	0.42 (2.44)	0.5 (2.9)

in the expected range under the exposure to protons. Here, the highest PBV is 5.68 ± 0.76 ppm. The speckle evaluation remains unchanged as well.
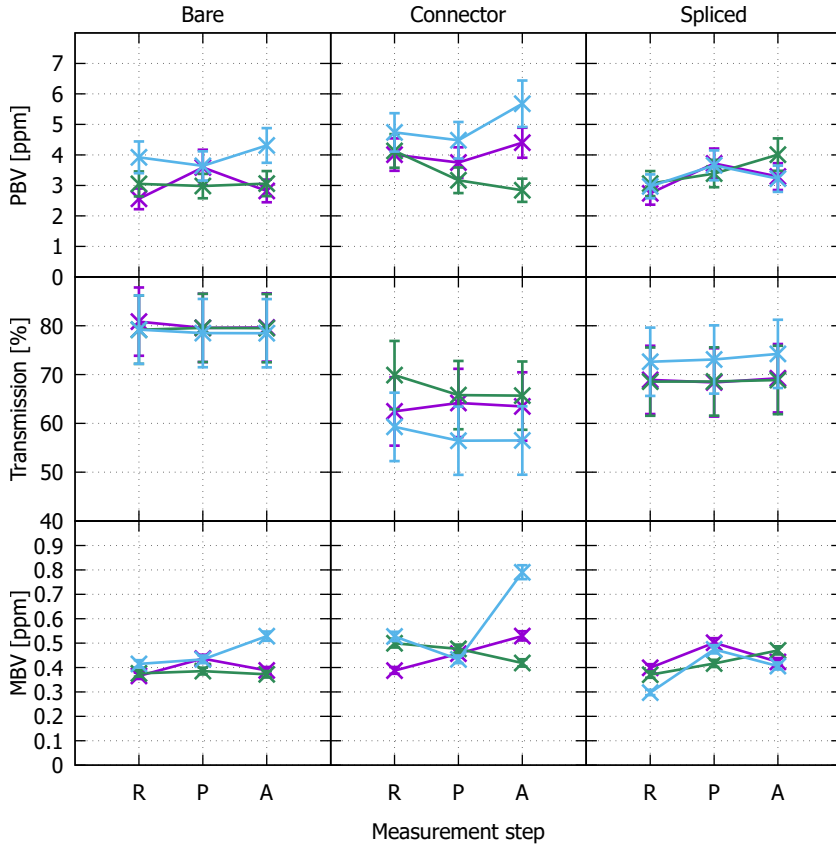
Figure 6.6: Results of the backscatter measurements for the proton radiation using the Nufern PM1060L fibers: The x-axis shows the measurement step, where "R" is the reference measurement, "P" is the measurement after the irradiation, and "A" another measurement after some annealing time. From top to bottom, the plot shows the measured PBVs, the transmission, and the result of the speckle evaluation, i. e. the MBVs. From left to right, the different fiber configurations are shown.

6.2.2 Nufern FUD-3561
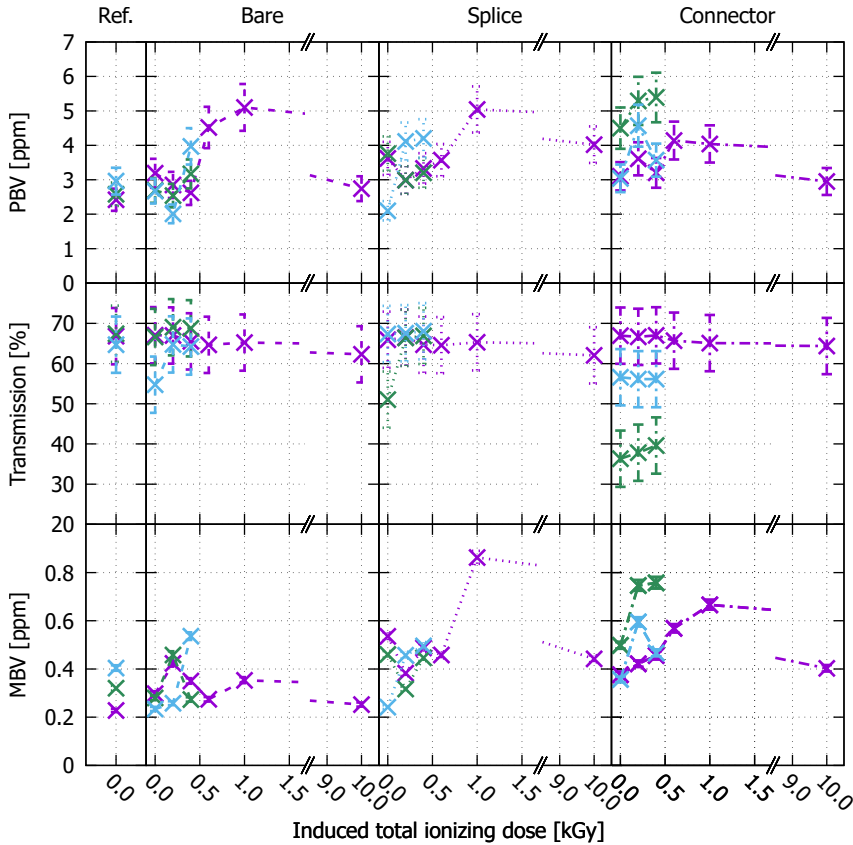
Figure 6.7: Results of the backscatter measurements with the Nufern FUD-3561: The plot is structured identically to figure 6.5. These measurements show in all three configurations that the backscattered and transmitted power remain constant with the increasing exposure to gamma radiation. One of the connectorized samples shows a bad connection, thus a lower transmission and higher backscatter.

Similar to the PM1060L fibers, figure 6.7 shows the results of the backscatter measurements using Nufern FUD-3561 fibers over increasing exposures to gamma radiation. In terms of backscatter and transmission, this fiber type shows no change with increasing exposure as well. Table 6.5 lists the highest measured PBVs for the different configurations that were tested, the overall highest PBV using the FUD-3561 is $7.84 \pm 1.04\,\mathrm{ppm}$.

This value is relatively high compared to the remaining measurements of the FUD-3561 fibers. However, no signs of a measurement problem resulting in this higher value were found. The second highest value was 5.86 ± 0.78 ppm, which better agrees with the remaining measurements. These measurements result in a worst-case assumption for the backscatter of 2.22 ppm/m (or 1.66 ppm/m for the second-highest measurement).

One of the connectorized fibers had a bad connection within the mating sleeve and thus has a significantly lower transmission than the remaining fibers. Nonetheless, backscatter and transmission remain constant for this fiber as well. However, the backscattered power is slightly higher than for the others, but not exceeding the other measurements significantly. Figure 6.7 also includes the results of the speckle view (in the

Table 6.5: Highest measured PBVs in the different configurations for the Nufern FUD-3561 fibers. All values in ppm.

Exposure	Bare	Splice	Connector
Gamma	5.28 ± 0.7	7.84 ± 1.04 (5.86 ± 0.78)	5.86 ± 0.78
Proton	4.49 ± 0.6	6.61 ± 0.88	6.08 ± 0.81

bottom row), which shows that the MBVs remain constant over the increasing exposure for all fibers tested. The averages of these are compiled in table 6.6. The resulting CBVs are given in brackets for each combination of radiation and configuration. These values are significantly lower than those in table 6.5, which results from the averaging and the general tendency that the calculated values are slightly lower than the measured ones with the chosen limit.

Table 6.6: Average of the MBVs for the different configurations and exposures for the Nufern FUD-3561 fibers. In brackets the resulting CBV following equation (4.13) is given. All values are in ppm.

Exposure	Bare	Splice	Connector
Gamma	0.43 (2.5)	0.47 (2.73)	0.51 (2.96)
Proton	0.51 (2.96)	0.66 (3.83)	0.60 (3.49)

Chapter 6

Figure 6.8 depicts the results of the measurements after proton irradiation. This figure shows - from top to bottom - the PBV, the transmission, and the MBV. These measurements show no significant change after the irradiation and the annealing steps compared to the unexposed step. This is valid for the three different configurations tested. The high PBV of the spliced violet fiber seems to be one of the rarer high results since the speckle evaluation shows a higher value which is still well within the range of the other measurements. The observed PBVs are compiled in table 6.5, while the averages of the MBVs are in table 6.6. These two tables show again that the CBVs calculated from the averages are lower than the measured peaks, similar to the case of gamma radiation.

6.2.3 Fiber configuration comparison

With the tests of the different fiber configurations - bare fibers, spliced fibers, and connectorized fibers - a comparison of these is possible. Interesting for the PRDS is whether the usage of a connector or splice increases the backscattered signal compared to a bare fiber and what amount of additional spurious backscatter occurs in different ways to realize the fiber connection. Nonetheless, a bare fiber is nearly impossible from an integration standpoint.

For the peak measurements, these values are given in tables 6.3 and 6.5, showing that both spliced and connectorized fibers show higher backscatter than bare fibers.

Table 6.7: Difference in the averages of the measured PBVs for the fibers of the second radiation campaign, compared to the bare fiber measurements. The averages are weighted by the number of measurements in each category. Values in ppm.

	PM1060L		FUD-3561	
Exposure	Splice	Connector	Splice	Connector
Gamma	0.56	0.49	0.3	0.61
Proton	0.01	0.81	0.33	0.45
Averaged	0.39	0.59	0.31	0.56
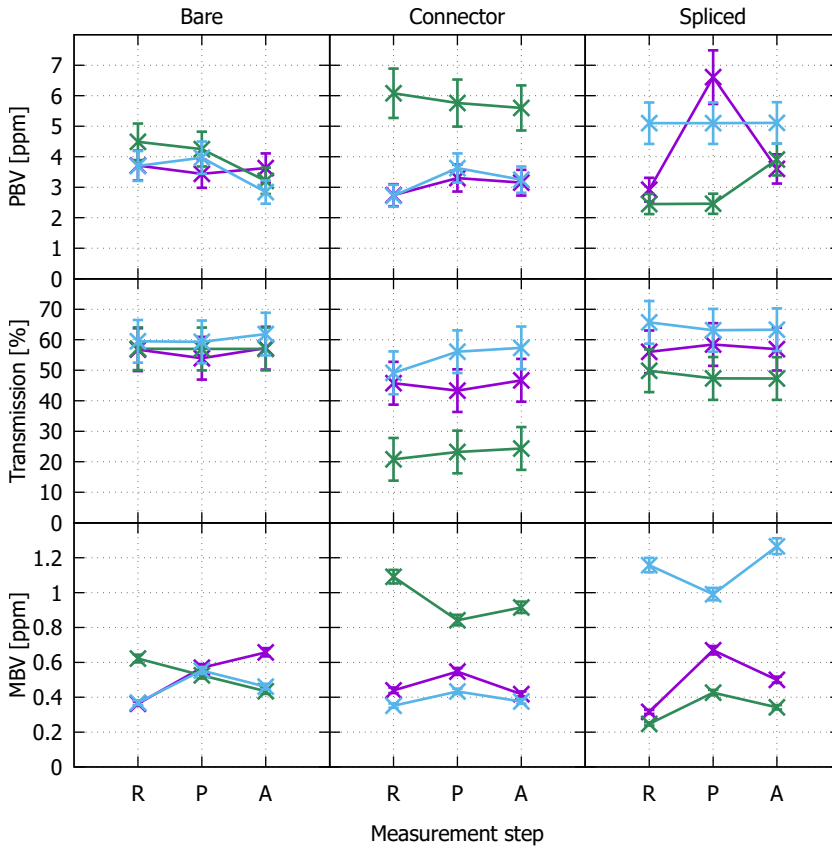
Figure 6.8: Results of the backscatter measurements over proton irradiation using the FUD-3561 fibers: This figure is set up in the same way as figure 6.6. Two specimens are noticeable here: The turquoise connectorized fiber and the blue spliced fiber: The connectorized fiber has a bad connection between the two parts, which is shown by the lower transmission. This also results in higher values in both backscatter evaluations. For the blue spliced fiber, the higher scatter values are likely a result of some damage that occurred during the splicing process. In consequence, this fiber is only 3 m long.

To estimate the additional "backscattered" signal induced by the splice or sleeve connection within the tested fiber specimen, the averages of the PBVs are compared to those of the "bare" fiber configuration. Strictly speaking, this is not a backscattered addition but a spurious reflection at the connection of the two fibers. Table 6.7 lists the results of these

comparisons for both fiber types tested. In all cases, the PBV is increased compared to the bare fiber. For the spliced PM1060L fibers under proton exposure, the difference is relatively small, which is probably a result of the low number of measurements. This indicates that an additional contribution of about 0.5 ppm in the PBV can be expected, which is slightly higher than the fit result in section 5.8 for connectorized fiber connections. The measurements show that the connector has a higher contribution than the spliced connection in most cases.

Therefore, assuming a worst-case contribution of the fiber connection of 1 ppm PBV seems reasonable and is valid for both mating sleeve and splice. For the final implementation, it is important to consider that the integration of a splice between the two optical benches within a spacecraft would be challenging due to space constraints. Therefore, a connector is preferable which is acceptable from the point of view of these measurements.

Additional Backscatter Measurements

In this chapter, we present further measurements related to backscatter. These include the polarization evaluation and the phase coupling induced by temperature changes. Lastly, we present results of backscatter and temperature coupling measurements using FIOSs that are foreseen for use in the PRDS EM.

7.1 Polarization effects

The upgraded setup as of section 5.4 allows investigating polarization effects in the backscattered signal (and the transmitted signal).

The first step to analyze polarization effects is to confirm that the heterodyne efficiency in both polarization axes is equal in a calibration measurement. Therefore, the S beam is changed to a 45° polarization state which should lead to roughly equal signals and heterodyne efficiencies in both channels. Figure 7.1 compares such a measurement to a measurement of the heterodyne efficiencies with a nominal S beam. This shows that the heterodyne efficiencies for both polarizations are indeed equal; the average for the p-polarized case in figure 7.1 (a) is 69 %. In addition, this also shows that the low power in the p-polarized state, for a nominal case, results in high noise, which can result in higher fluctuation and wrong values of the heterodyne efficiency (i. e. $\eta > 1$).

These measurements confirm that the heterodyne efficiency is equal for both polarization states, which is expected following equation (2.6) for observing interference between beams of the same polarization. The slight differences result from the imperfections in the polarizing beam splitter, which reflects a fraction of the p-polarized light into the PR used to measure the s-polarized contribution (and vice versa), and in the alignment of the optical components. Two series of tests were performed: In the first, the fiber collimator was rotated, while in the second, the incoming polarization was rotated, but the collimator was fixed. Both result in a mismatch between the slow axis of the fiber and the polarization of the beam. Figure 7.2 depicts this schematically. In both cases, the output collimator in the transmission port is fixed.

Figure 7.3 shows exemplary two time-series at different input polarization states (s-polarized and a 45°-polarization), thus, from measurements following the approach depicted in figure 7.2 (b). Comparing these time series shows that the backscatter contribution in the s-polarization decreases when changing the input polarization from s-polarized (0°) to 45°. In the same manner, the p-polarized contribution to the backscattered signal increases. On average, the 45°-input-polarization results in
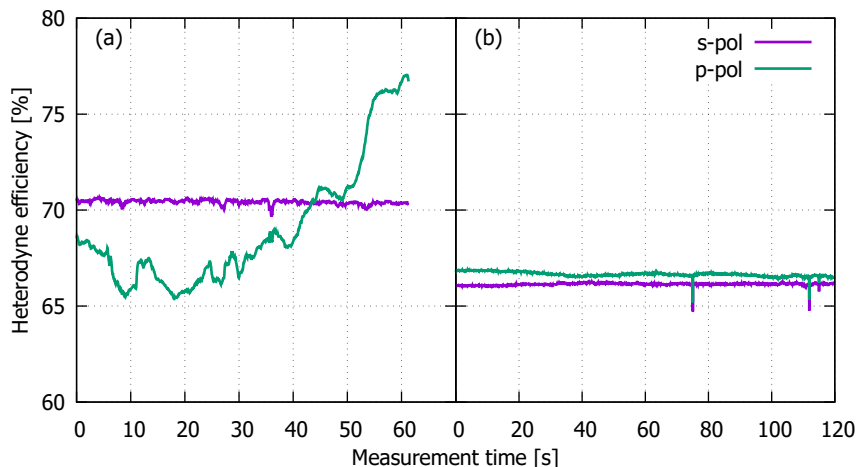
Figure 7.1: Comparison of the heterodyne efficiency for different polarization states of the S beam: (a) shows the heterodyne efficiencies with an s-polarized S beam and (b) with a 45°.
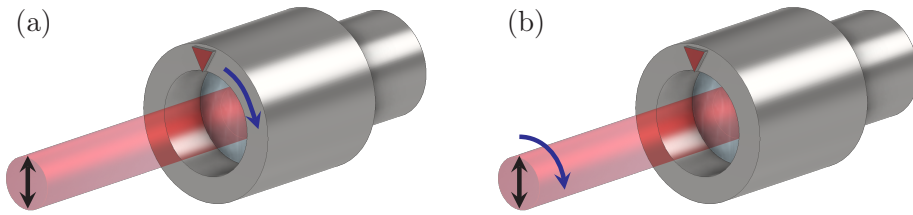
Figure 7.2: View onto the fiber collimator of the backscatter-polarization measurements. Part (a) shows measurements with a fixed input s-polarized input beam while turning the fiber collimator. On the other hand, part (b) shows measurements with a fixed fiber collimator position while turning the input polarization from s- to p-polarized.

backscatter amplitudes that are roughly equal. This is also visible in the speckle depiction shown in figure 7.4, which also shows the higher peak in the s-polarized channel than in the p-polarized one.
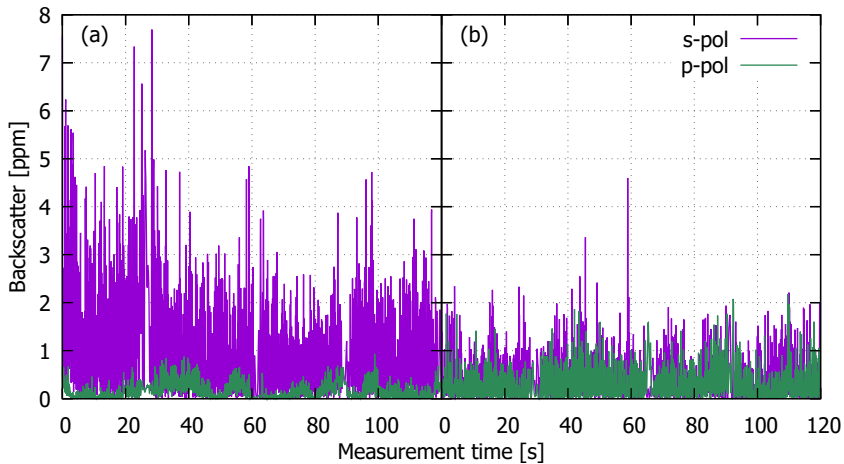
Figure 7.3: Exemplary time series of the backscatter measurement in different input polarizations of the S beam: (a) s-polarized and (b) a 45° polarization.

Several measurements following the scheme depicted in figure 7.2 have been performed, and the results of these are depicted in figure 7.5. The three parts show the different measurement approaches: parts (a) and (b) follow the approach depicted in figure 7.2 (a), i. e., rotating the fiber collimator while using a constant input polarization, while part (c) fol-

Chapter 7

75
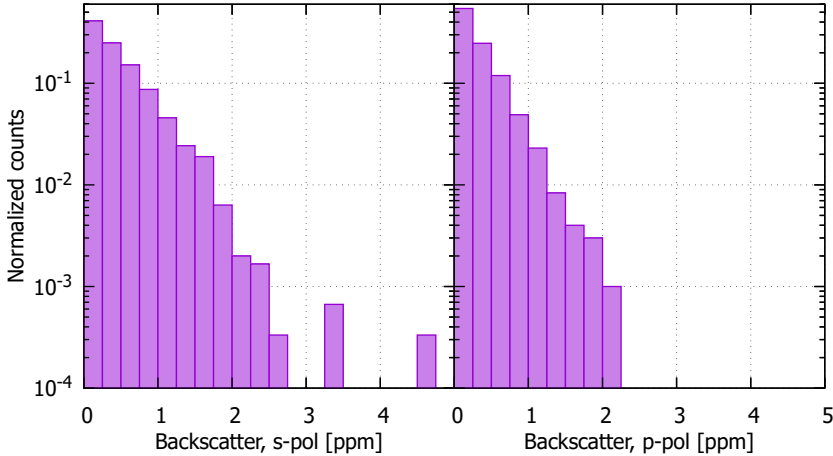
Figure 7.4: Histogram of the backscatter time series in figure 7.3 (b). This shows that the amount of backscatter in both polarization axes is about the same.

lows the approach in figure 7.2 (b), i. e. the input polarization is changed and the collimator is fixed. In all three cases, the transmitted polarization follows the expected case. In parts (a) and (b) from s-[p-]polarized to p-[s-]polarized depending on the input polarization. In part (c), the transmitted polarization equals the incident polarization as expected since the fiber collimator was not rotated.

The polarization behavior is different for the backscattered light: For the measurements with the rotating fiber collimator, the polarization of the backscattered light starts at the polarization of the incident beam and rotates over to 45° for a collimator angle of 45° and then returns to the incident polarization state. This is a result of the beam not propagating in one of the symmetry axes of the fiber and thus coupling of light between these. For the case of rotating the input polarization, however, the polarization of the backscattered light follows the input polarization, similar to the transmitted polarization.

Furthermore, these measurements show that the error in the polarization angle over the measurement, i. e. the fluctuations of the polarization over the measurement time, is larger for the backscattered than for the transmitted light.
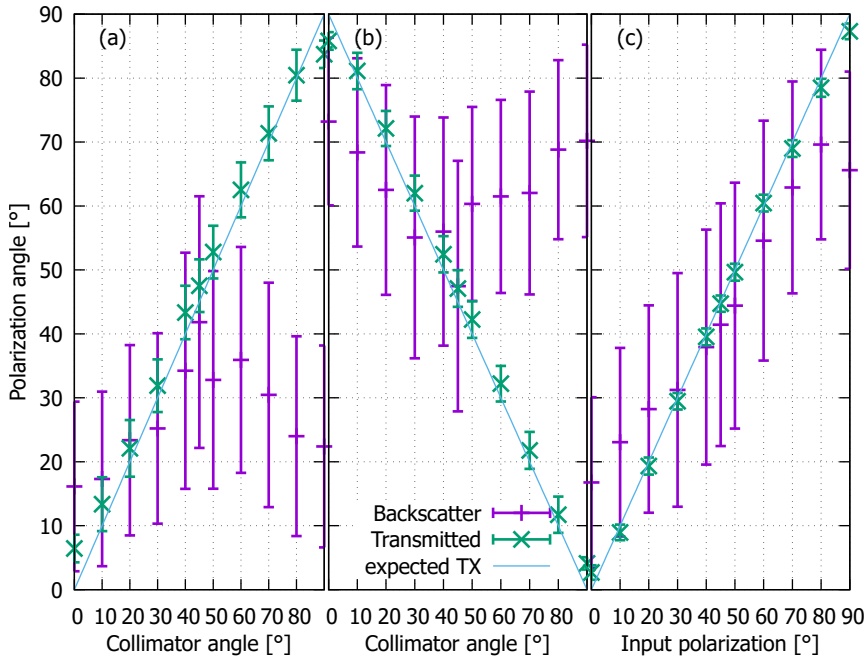
Figure 7.5: Results of the measurements while rotating collimator or polarization: Each part shows the measured polarization of the backscattered and transmitted beam, part (a) and (b) with a rotating fiber collimator and s- or p-polarized light incident onto the fiber, respectively. Part (c) shows the results for a fixed collimator with changing input polarization. Additionally, the expected polarization state of the transmitted light is shown.

Figure 7.6 shows the time series of figure 7.3 transformed into the measured polarization angle and a moving-average of that angle as the non-averaged angle fluctuates significantly. The figure shows again the time series with an s-polarized and a 45°-polarized S beam which agrees with the observations of figure 7.5 (c). However, it also shows that for some time spans, the backscattered polarization is nearly orthogonal to the incident polarization. Therefore, it is expected that the backscattered light induces additional polarization noise in a bidirectional fiber connection.

Applying this to the fiber connection of the PRDS, setting the power incident to the fiber to $P_{\text{in}} := 1$ in a nominal s-polarized state, and Assuming a worst-case of fully p-polarized backscatter of 10 ppm, this is
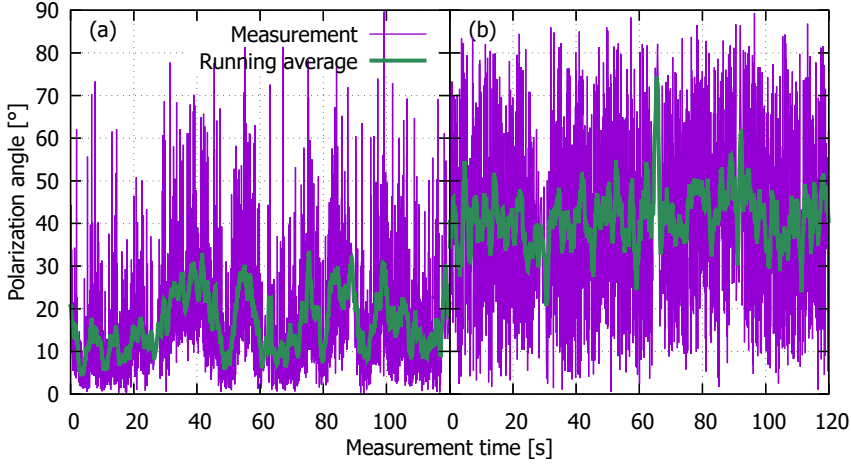
Figure 7.6: Time series of the polarization angle of the backscattered light with (a) an s-polarized or (b) 45°-polarized input beam. In both cases, the backscattered light has a varying polarization which, on average, is close to the state of the input beam's polarization.

an expected amount according to chapters 5 and 6, leads to a polarization change of

$$\Delta p = \mathrm{atan}\left(\frac{P_{\text{p-pol}}}{P_{\text{s-pol}}}\right) = \mathrm{atan}\left(\frac{10\,\mathrm{ppm}}{1}\right) \simeq 10 \times 10^{-6}\,\mathrm{rad} \simeq 5.73 \times 10^{-4\circ}. \tag{7.1}$$

In addition, the OB features a polarizing beam splitter (PBS) after the FIOS which suppresses at least 99.6 % of the p-polarized light and, thus, the change in polarization angle will be smaller:

$$\Delta p = \mathrm{atan}\left(\frac{0.04 \cdot P_{\text{p-pol}}}{P_{\text{s-pol}}}\right) \simeq 2.29 \times 10^{-6\circ}. \tag{7.2}$$

Fortunately, this contribution is lower than the expected polarization noise imposed by common PMFs with an expected cross-talk of about $-40\,\mathrm{dB}$, which results in a polarization noise of $\Delta p = 2.3 \times 10^{-4\circ}$ when including the PBS.

Concluding, these measurements show that the backscattered light returns primarily in the polarization state of the light injected into the fiber. Thus, the polarization state of the backscattered light on the LISA

OB is decided by the alignment of the coupling into the fiber. For this reason, and the inherent property of the polarization fluctuations of the backscattered light, a polarization cleaning stage, as planned, is advantageous.

7.2 Temperature coupling

With the implementation of the Peltier element to modulate the fiber temperature to accelerate the backscatter measurements, a measurement of the temperature-to-phase coupling is possible. In the original version of the backscatter experiment, such measurements were performed in the "calibration mode." As the upgraded backscatter experiment features an interferometer in the transmitted path, the measurement of backscatter and temperature-to-phase coupling was done simultaneously; see section 5.7 for details regarding the temperature modulation.
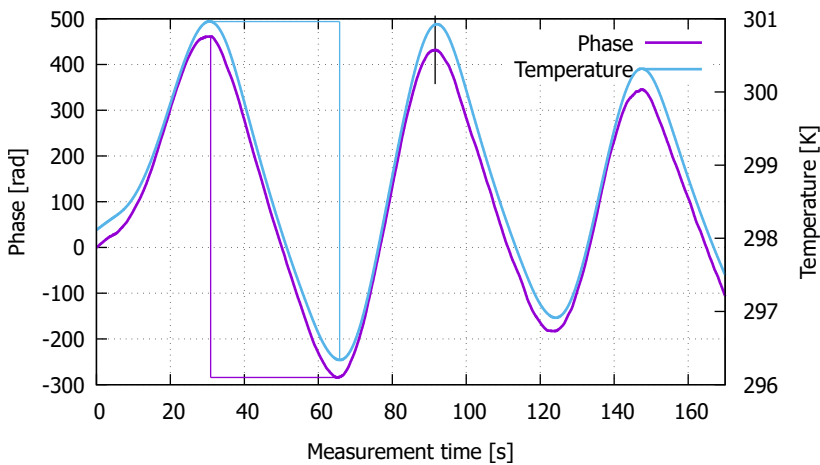
Figure 7.7: Time series of temperature and phase measurements for the temperature coupling measurements: The extrema of temperature and phase measurements are compared to obtain a value for the temperature-to-phase coupling. The plot also shows that the fiber has a faster reaction time, indicated by the black line at the second maximum, and a higher resolution.

Chapter 7

79

Figure 7.7 shows the time series of phase and temperature measurements for obtaining the temperature-to-phase coupling. The measurements show that the fiber measurement has a shorter reaction time and a higher resolution. The temperature-to-phase coupling is calculated by comparing both time series: The differences of the neighboring extrema in both time series are divided:

$$\frac{\Delta\varphi}{\Delta T} = \left| \frac{\varphi_{\text{ext}_1} - \varphi_{\text{ext}_2}}{T_{\text{ext}_1} - T_{\text{ext}_2}} \right|. \tag{7.3}$$

Dividing this value by the fiber length results in the desired coupling value in $\text{rad}/(\text{K}\,\text{m})$, in the shown example $46.03\,\text{rad}/(\text{K}\,\text{m})$.
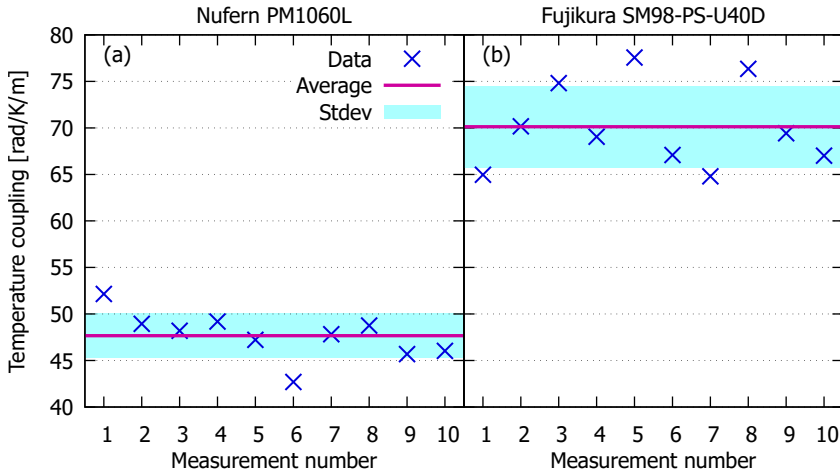
Figure 7.8: Several measurements of the temperature coupling for the same fiber were done for one fiber of the types (a) Nufern PM1060L and (b) Fujikura SM98-PS-U40D each. The Fujikura fiber shows higher coupling and a higher variance than the Nufern fiber.

The first measurement set was performed to determine the repeatability of the measurements. For this, a single Nufern PM1060L fiber was aligned to the setup and repeatedly moved on the heating element between the different measurements. A modulation of $\pm 2\,\text{K}$ was applied to the fiber. The results of this are shown in figure 7.8 (a). A comparison measurement was performed using a spare of the Fujikura fibers tested in section 6.1.1, shown in figure 7.8 (b).

These measurements show that the measured coupling factor varies only by about 2.4 rad/K/m (standard deviation) around the average of the measurements (here 47.7 rad/K/m). For the Fujikura fibers, the observed values are 4.4 rad/K/m around an average of 70.1 rad/K/m. These values are used as an error estimate for the subsequent measurements.

To see how much effort is required to characterize flight fibers and to compare the temperature coupling of the different fiber types, measurements with the different types were performed. The results of these measurements are depicted in figure 7.9.
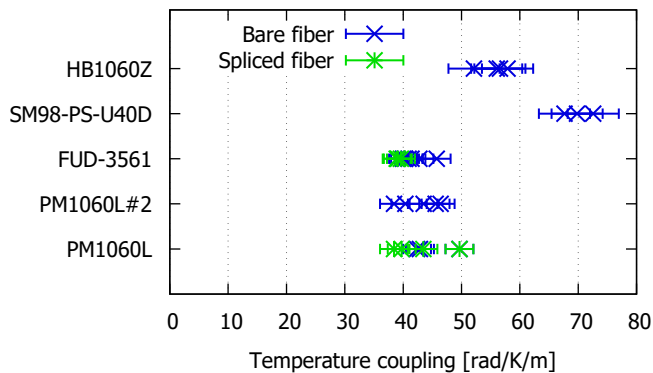
Figure 7.9: Temperature coupling measurements of several fibers of different types: The Fujikura fibers (type SM98-PS-U40D) show the highest temperature coupling of the tested fiber types, the Fibercore fibers (type HB1060Z) show a slightly lower coupling, and all the Nufern fibers (types PM1060L and FUD-3561) show a lower coupling. Fibers from two batches were tested for the type Nufern PM1060L, which shows no significant difference between the batches. These measurements reveal that a splice along the fiber does not change the temperature coupling significantly.

Here, results for three different fiber types in four different fiber batches are shown. The Nufern PM1060L fibers originate from two different batches; consequently, the results are split into two columns. The distribution of the measurements within a single batch is similar to the observed distribution in figure 7.8 (a). Furthermore, all Nufern fibers show values in the same order of magnitude, lying in the range 35 to 50 rad/K/m. On the other hand, the measurements with the Fujikura

fibers are higher by about a factor of two, in the range 65 to 75 rad/K/m. The single type of non-PMFs tested, the PZF HB1060Z by Fibercore, shows a coupling between the other fibers in the range 50 to 60 rad/K/m.

This shows that the coupling values for different fibers from the same batch are within a small range. Thus, a badge characterization appears to be reasonable. The results of the Nufern fibers also indicate that the core diameter of the fibers is not the driving factor in the difference of the temperature coupling as the two types feature different core diameters. The primary geometric difference, apart from the core diameters, between the Nufern and Fujikura fibers is the coating diameter which is $245 \pm 7\,\mu\text{m}$ for the former and $400 \pm 15\,\mu\text{m}$ for the latter (all fibers have the same cladding diameter of $125\,\mu\text{m}$). In the case of the HB1060Z, the intermediate coupling can be explained in two steps: The coating diameter is the same as for the Nufern fibers, thus the lower coupling than the Fujikura fibers. However, the coupling is higher than the Nufern fibers' due to the bow-tie geometry.

The temperature coupling values measured throughout this thesis agree with other research results found in [133–135]. It is important to consider that the fibers tested here were jacket-less. Jacketed fiber shows higher temperature coupling compared to jacket-less specimen, as shown in [134].

7.3 FIOS tests

The engineering model (EM) (see section 3.2.5) will feature several fiber injection optical systems (FIOSs). As these were built not directly onto the optical bench of the EM but as separate entities which are bonded onto the optical bench, it is possible to characterize these beforehand using the backscatter setup. To do so, the fiber collimator in port A was replaced by a two-axis alignable mount for the FIOS. Figure 7.10 shows a FIOS mounted in the backscatter setup, which was held by a clamping piece around the strain relief of the FIOS. The FIOS was mounted such that no other surface was in contact with the mount. The measurement
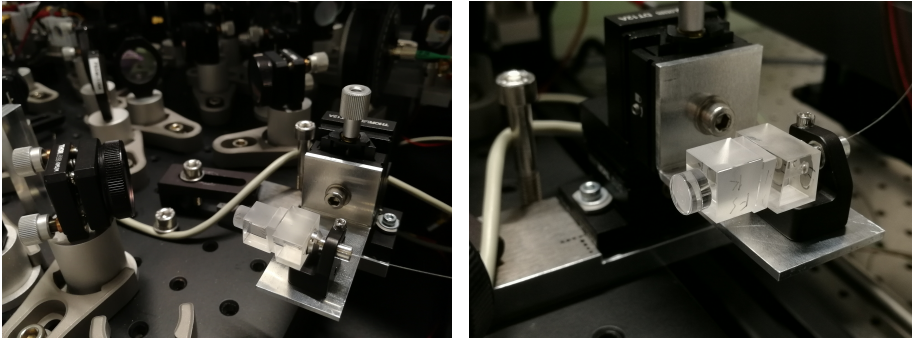
Figure 7.10: FIOS mounted to the backscatter setup for characterizing its scattering properties. A clamp holds the FIOS at its strain relief, and the clamp is mounted onto a xy-stage. This allows a pre-adjustment before the beam is mode-matched to the fiber using the two mirrors leading to the FIOS.

process of characterizing the FIOS is the same as the backscatter measurements described in section 5.2. In addition, the phase measurement in the TX interferometer was used to measure the temperature-to-phase coupling of the fiber attached to the FIOS. This was done by comparing the phase measurement across the fiber to the temperature measurement of the heater, as described in section 7.2.

Each of the FIOS consists of a lens, three fused silica pieces, and a fiber of a length of 1 m ending in an FC/APC connector (for more information regarding these FIOSs see [136]).

The measurements of the FIOSs show that the temperature coupling is on the upper end of the reference values, and some exceed the reference values. There are two possible explanations for this: In the reference measurements fibers of 4 m were used, resulting in several overlapping fiber loops on the heating plate and thus reducing the measured coupling by worse heat transfer to the length of the fiber. The other option is the possibility of measurement errors while measuring the fiber length and modulated length, i. e. the part of the fiber in contact with the Peltier element. When using shorter fibers, these errors are larger in relation to the fiber length. If the modulated length is underestimated, the obtained coupling value will be too high.

Chapter 7
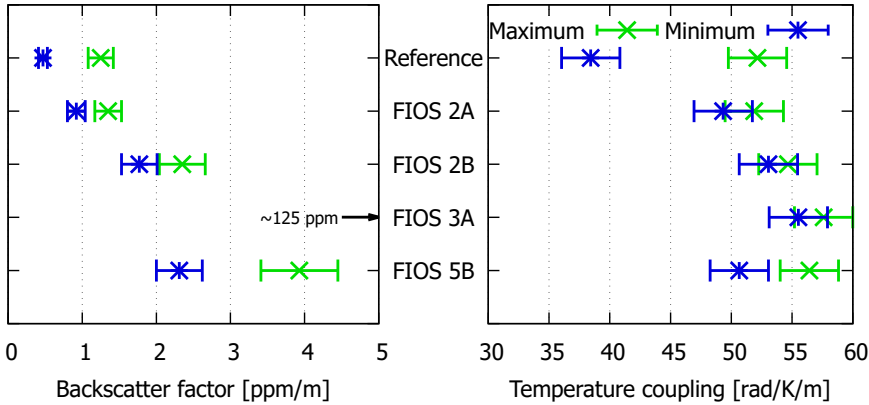
Figure 7.11: Comparison of the backscatter and temperature coupling measurements to the values obtained with the PM1060L fibers in the radiation and temperature measurements: The range from the lowest obtained value to the highest is shown for each FIOS and the reference. FIOS 3A is explained in more detail in the text. The FIOSs are ordered in the sequence of measurements, starting from the top.

In terms of backscatter only, FIOS 2A is within the measurement range of the reference measurements. The backscatter values reach as high as 3.9 ppm/m for FIOS 5B. FIOS 3A has no visible backscatter value in figure 7.11 as this would make a differentiation between the others impossible. The first measurement of FIOS 3A showed a backscatter of 26.29 ± 2.50 ppm/m, and the remaining measurements were in the range 114.3 ppm/m to 125.3 ppm. An investigation of the fibers using an IR-viewer revealed leaking light from the cladding, which indicated damage to the fiber's core. However, the temperature coupling values are within the range of the other measurements, albeit high. One of the temperature measurements with FIOS 3A was comparably high, at $73.5 \, \mathrm{rad \, K^{-1} \, m^{-1}}$. This measurement was excluded from the evaluation as the upper copper plate of the Peltier oven (see figure 5.12 (b)) was not mounted.

With the current implementation plan of the PRDS, PBVs in the single-digit ppm-region up to a few tens of ppm for the fiber connection are acceptable to achieve the required performance. Therefore, the values observed for the FIOSs tested here are promising. Chapter 9 shows this

in more detail using performance simulations of the PRDS with the values observed here.

8

Contributions of Moving Fibers

In this chapter, we introduce the "motion mock-up," a device that allows the measurement of coupling of fiber motion into the measured phase. Subsequently, we show the measured backscatter effects, phase coupling, and polarization effects. Lastly, we compare different fiber mounting approaches in terms of phase coupling.

8.1 The motion mock-up

In LISA, the backlink fiber will be routed through the satellite to interconnect the two optical benches. The MOSAs will move over the mission to compensate for the angular breathing [29], and, in consequence, the fibers interconnecting the two optical benches will undergo movement as well.

As optical fibers are good sensors for numerous effects [82, 83], and fiber-based inclinometers and goniometers exist [137, 138], it is clear that motion affects the fiber's transmission properties. Although these sensors are based on the transmission of SMFs, it is expected that movement of the fibers couples into the phase readout. This gets apparent when including the fact that fringe-based measurement methods of fiber bending exist [139] and periodic micro bends induce phase shifts [68].

As per mission design the fiber motion within the spacecraft will happen with a period of once per year and thus be outside of the LISA measurement band [46]. However, harmonics of the motion frequency could appear in the phase that could reach into the LISA measurement band. In case of a high coupling from the fiber motion into the phase, corrective measures might be required.

The motion mock-up was set up to address this and obtain a coupling factor between LISA-like motion and the optical phase. Figure 8.1 shows the motion mock-up. The coupling factors are implemented into the performance simulations of the backlink, and the resulting performance is explained in chapter 9.
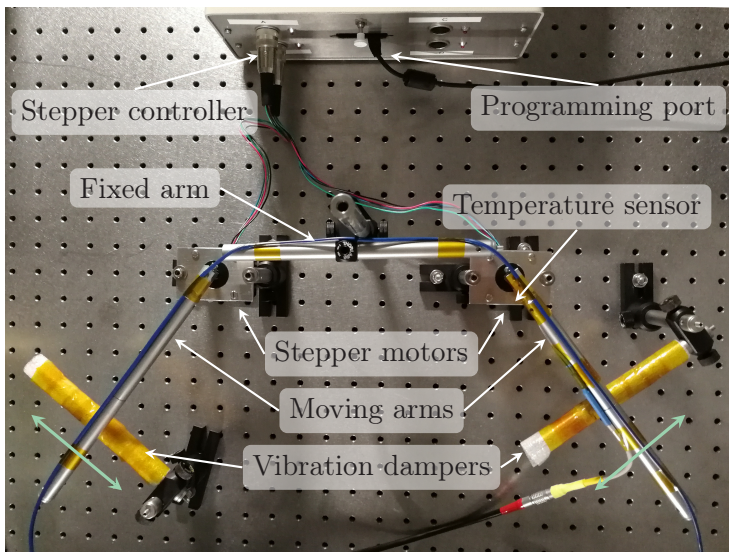
Figure 8.1: Photograph of the motion mock-up: Two stepper motors move two lever arms in a LISA-like manner to which a fiber is mounted. The lever arms are supported on foam to reduce vibrations originating from the arms.

The motion mock-up consists of two stepper motors, two rotatable lever arms, and a fixed lever arm. A fiber (type PMCONN-3-622 by Lightcomm which uses a Fujikura SM98-PS-U25D) is routed along these lever arms, and the stepper motors rotate these to simulate MOSA actuation within a LISA spacecraft. Therefore, the fixed lever simulates the truss connecting

the two MOSA where the fiber is routed. The motion is performed in a sinusoidal manner, as the change in inter-spacecraft angle in LISA will be in that manner when neglecting higher order contributions which are shown in [140]. In consequence, we describe the motion angle for our experiments as

$$\alpha(t) = \alpha_{\mathrm{max}} \cdot \sin(2\pi f_{\mathrm{mot}} t) \qquad (8.1)$$

where α_{max} is the motion amplitude, i. e. half the opening angle of the motion mock-up, and f_{mot} the frequency of the motion. Two different sets of measurements were performed: Motion at a fixed frequency but changing angle (motion amplitude) and motion with a fixed angle but changing frequency. In the phase evaluation, a third type of measurement was introduced: Measurements with a constant mean angular velocity $\bar{\omega} = \alpha_{\mathrm{max}} \cdot f_{\mathrm{mot}}$.

The following sections present the results of the motion measurements. Most of these measurements were performed using the upgraded backscatter setup, see section 5.4, where the motion mock-up is placed in the position of the fiber under test. Evaluations are performed in terms of backscatter, polarization, and phase effects.

8.2 Motion effects on backscatter

Similar to the temperature modulation, the movement of the fiber under test "accelerates" the backscatter measurement, i. e. there is a higher fluctuation in the measurement's time series. In this case, this depends on the motion speed. Figure 8.2 shows typical time series of the backscattered signal during motion for slower and faster motion, i. e. $\pm 5°$ at $0.02\,\mathrm{Hz}$ and $5\,\mathrm{Hz}$, respectively.

The backscattered power lies within the range observed in the unmoved backscatter measurements for the lower motion frequency. Compared to figure 5.11 (a), more substantial fluctuations are visible in the case of motion shown here. Nonetheless, the temperature modulated case (figure 5.11 (b)) shows similar if not stronger fluctuations of the backscattered signal compared to the measurement under slow motion. However,
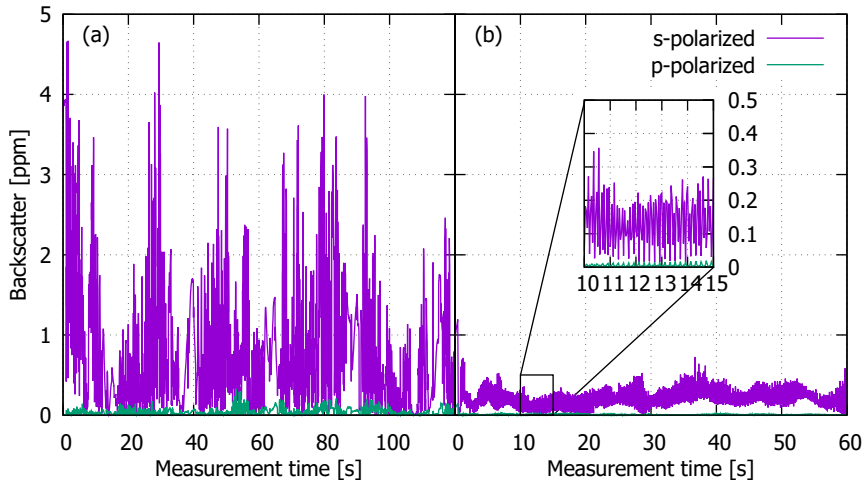
Figure 8.2: Time-series of the backscattered signal during motion: Part (a) shows a backscatter measurement with a slower motion ($\pm 5°$ at $0.02\,\mathrm{Hz}$), which is similar to the time series of a temperature-modulated measurement. Part (b) shows a typical measurement at faster motion ($\pm 5°$ at $5\,\mathrm{Hz}$), which shows a significantly suppressed backscatter. The zoom-in reveals that substantial changes appear at the motion frequency.

for faster motion, as shown in figure 8.2 (b), the observed backscattered power is significantly lower and shows strong spikes within the time-series repeating with the motion frequency. The fast motion either suppresses the scattering or disturbs the interference resulting in a signal collapse. This signal reduction is also visible in the phase, as shown in section 8.3, indicating that this effect is likely a strong disturbance suppressing the desired signal. Since the unmoved and the slowly moved case show similar amounts of backscatter, no effect of the fiber motion in terms of backscatter is expected for the PRDS.

8.3 Phase coupling

To obtain the coupling between motion angle and the measured phase, in rad/°, the measured heterodyne phase passing through the fiber and the

phase in the reference interferometer are compared. The resulting phase difference

$$\varphi_{\text{fiber}} = \varphi_{\text{TX}} - \varphi_{\text{Ref}} \qquad (8.2)$$

is detrended (i. e., to remove thermal drifts), an exemplary time-series of the resulting phase is depicted in figure 8.3 that shows a contributions at the motion frequency and its harmonics, and demodulated a second time using the IQ-demodulation as described in section 2.3. The demodula-
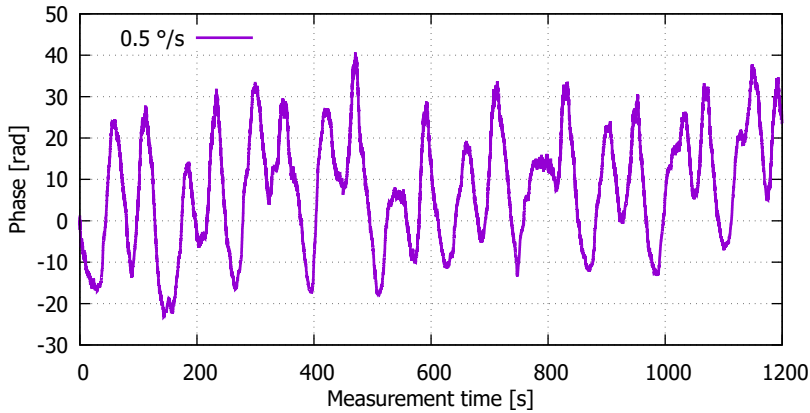
Figure 8.3: Exemplary time-series of the phase signal measured across the fiber under motion after detrending: The time-series shows contributions at the motion frequency and at its second harmonic. This example shows a motion with a mean angular velocity of 0.5 °/s.

tion is performed at the excitation frequency. Measurements at different frequencies with a constant motion amplitude and measurements with constant motion frequencies but different angles were performed. Figure 8.4 shows the results of such an approach which interestingly shows that the coupling is constant for different angles but (non-linearly) increasing with decreasing frequency. However, the measurements show a larger coupling for small angles than the limit reached above 5°, at around 4 rad. The angular velocity of the motion increases when the motion angle is increased, and the angle remains the same. Similarly, the higher the motion frequency at the same motion angle, the higher the angular velocity. Combining this with the fact that both measurement series reach a limit at the upper end indicates that the coupling can only

Chapter 8

be measured when the angular velocity of the motion is the same for all tested angles.
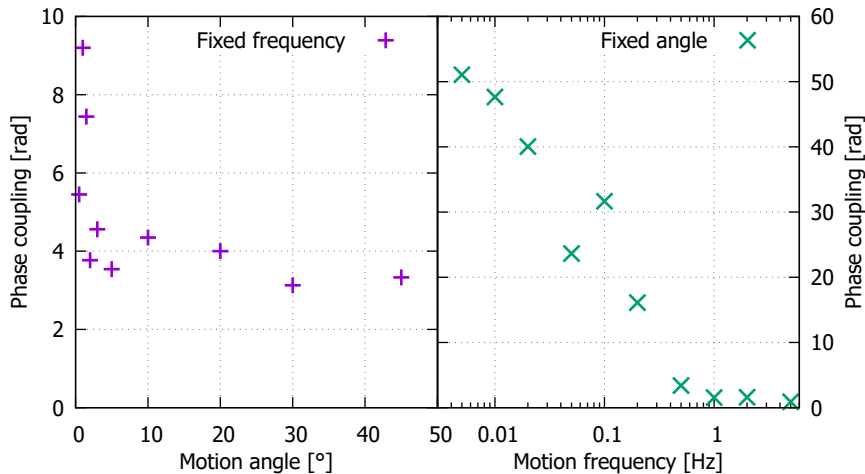
Figure 8.4: Examples of motion measurement series with fixed frequency or angle: The fixed frequency measurement was performed at 5 Hz and showed no significant dependence of the phase coupling on the motion angle. On the other side, the fixed angle measurement was performed with a motion angle of 5° and showed a non-linear decrease of the coupling with increasing frequencies.

A series of measurements with different motion angles at a constant mean angular velocity is exemplarily shown in figure 8.5. A linear function of the form $f(x) = m \cdot x$ is fitted to the measured phase data to evaluate such measurements. The function was chosen without an offset parameter as a motion angle of 0°, which means no motion, induces no phase signal. m is then the desired coupling factor in rad/°. In the shown example, this factor is given as 0.3 rad/°.

Figure 8.6 shows the results of all measurements at different mean angular velocities combined plotted over the angular velocity. The fit results form two groups, fitting to the different measurement series of 4 °/s and 6 °/s, respectively. This is likely a result of slightly different fiber routing of the "loose end," which connects the motion mock-up to the backscatter experiment and, thus, different contributions to the phase of unintended
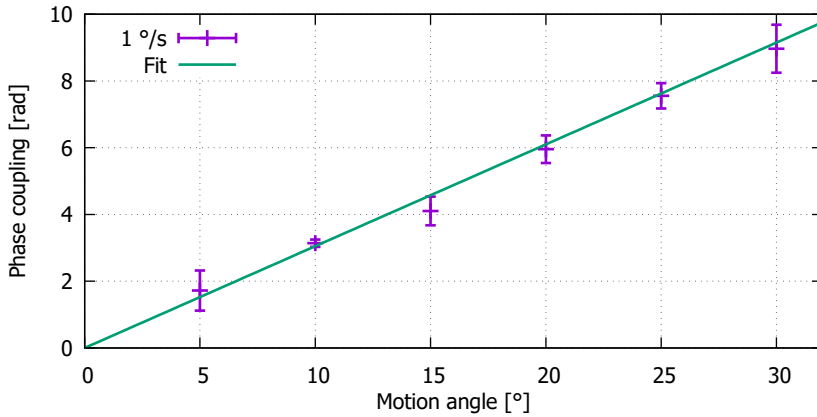
Figure 8.5: Example of a series motion measurements with constant mean angular velocity, here of $1\,°/s$. The linear fit results in a coupling factor of $0.3\,rad/°$

fiber motion. Therefore, we can assume that the measurements resemble a worst-case estimate as this additional motion will not exist in LISA.
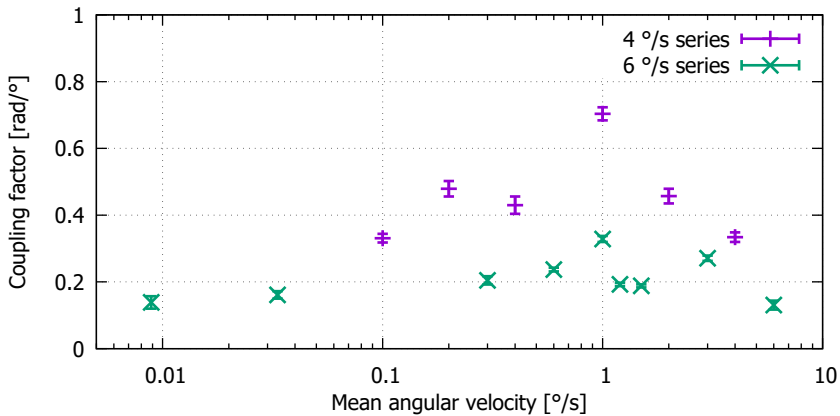
Figure 8.6: Motion coupling factors at different mean angular velocities: A difference between the two measurement series is visible, which was likely caused by different routing of the "loose" fiber end connected to the backscatter experiment.

Both series, however, have the highest coupling at a mean angular velocity of $1\,°/s$, and the coupling decreases towards both, lower and higher angular velocities. As all measurements are in the same order of magni-

tude an upper limit of the coupling can be estimated. Here, a limit of $1\,\mathrm{rad}/°$ seems reasonable when adding some additional error margin to the highest observed value.

8.4 Polarization

Using the upgraded backscatter setup to measure the fiber effects induced by the motion mock-up allows to measure polarization effects by comparing the interference amplitudes in the two linear polarization states (with the corresponding PRs) and calculating the resulting polarization angle. Since figure 7.6 (a) shows that the polarization fluctuations in the backscatter port are generally high, the effects of the motion on the polarization were monitored in the transmission port. Similar to the phase measurements, the polarization measurements show features resembling the motion in frequency and shape; figure 8.7 shows this.
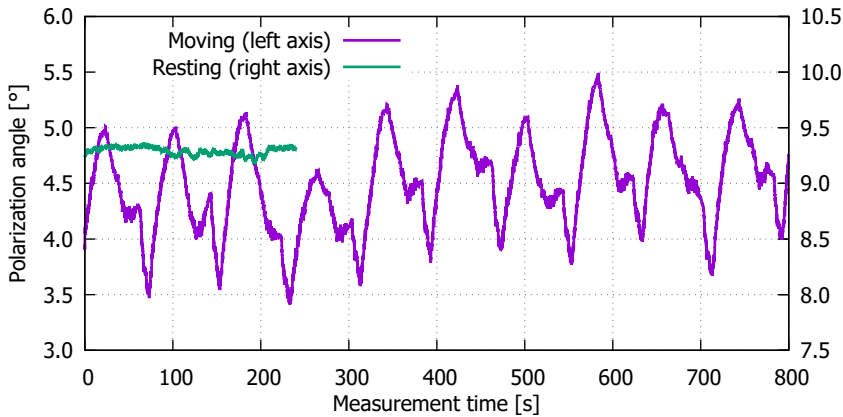
Figure 8.7: Time-series of the polarization angle of the transmitted beam during the motion measurements: In this example, the motion was performed at a mean angular velocity of $0.5\,°/\mathrm{s}$ over an angle of $20°$. Here, the motion induces a change in polarization of about $2°$ peak-to-peak, and the motion cycle is visible in the polarization angle. In comparison, a shorter measurement without motion is shown. This measurement is at a worse polarization angle, but the fluctuations are about an order of magnitude lower.

In this example, a motion over 20° was performed at a mean angular velocity of 0.5 °/s, resulting in an amplitude of about 2 °$_{\text{pp}}$ of polarization angle change. In comparison, the albeit shorter measurement with the fiber resting shows fluctuations in the polarization angle in the order of 0.1°. The higher (i. e. worse) polarization angle of the fiber in the resting case is a result of the alignment in this example. The fluctuations, however, are usual for the setup.

Combining several of such measurements at the same mean angular velocity and different angles allows fitting a linear function to the data resulting in a coupling factor between motion amplitude and polarization change.
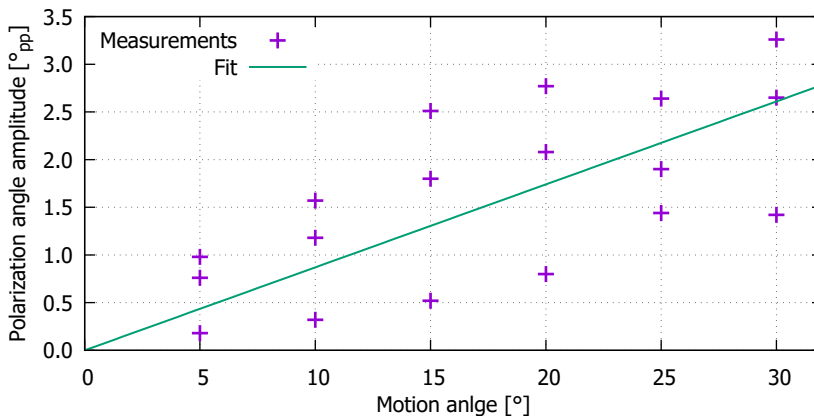
Figure 8.8: Example of the polarization view of a measurement series with constant mean angular velocity: In this case, the mean angular velocity was 0.5 °/s. A slight increase of the change in the polarization angle can be observed with larger motion amplitudes. Here the increase is fitted to a linear function with a slope of 0.087 °/°.

Figure 8.8 shows this exemplary. Measurements at the same angle show slightly different polarization changes, but it is clear that, for a constant mean angular velocity, the polarization coupling towards larger motion angles increases. In the example shown, the linear fit results in a coupling factor of 0.087 ± 0.009 °/°.

Performing such measurements at different mean angular velocities results in a dependence of the coupling factor to the angular velocity. This
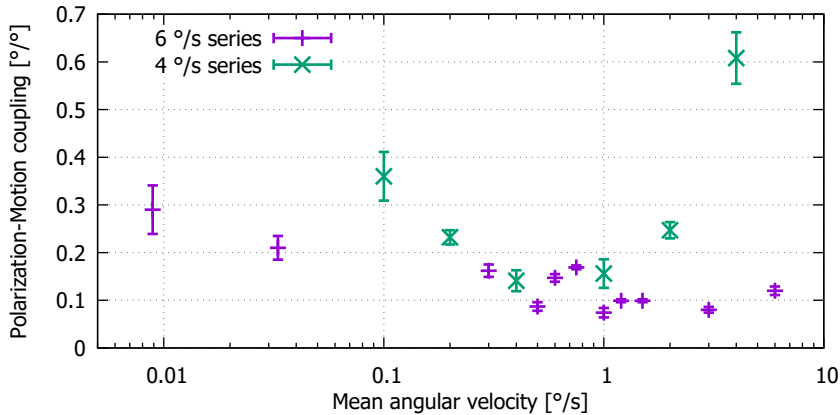
Figure 8.9: Results of the polarization evaluation of the motion measurements at different mean angular velocities: Most measurements show a relatively small coupling. However, the measurements with the lowest mean angular velocities and the highest one in the 4 °/s-series show higher coupling and larger errors (and the residuals of the fits are significantly higher).

is shown in figure 8.9. All measurements show a coupling factor below 0.4 °/° with one exception: The measurement at 4 °/s in the 4 °/s-series. Although this measurement did not show any abnormalities in the phase evaluations, it is worth noting that this measurement set was the first and included another motion angle at 45° that was not achieved in the motion. A too tight mounting might have been the reason for this which ultimately resulted in the higher polarization coupling. The mounting was altered afterwards, and thus, this measurement is shown for completeness.

A note to the polarization alignment of the fibers: The polarization propagating to the fiber of the motion mock-up was optimized using a polarimeter to a PER $< -60\,\mathrm{dB}$ which is the measurement limit of the polarimeter used. The fiber's alignment was performed using the two PRs TX_s and TX_p: By minimizing the signal on TX_p and maximizing the signal on TX_s the desired polarization along the slow axis of the fiber is achieved. However, this method is not as accurate as the polarimeter and does not resolve circular contributions induced by the

fiber. Therefore, it is possible that imperfect alignment contributes to the polarization coupling induced by motion shown here.

8.5 Different fiber mounting approaches

In addition to measuring the coupling factors during movement of the fibers, measurements with different approaches mounting the fiber to the motion mock-up were performed. Such measurements can determine in which differences these result in terms of phase coupling. The different mounting options were tested with a fixed mean angular velocity of the motion. For a good visibility in the measurement $\bar{\omega} = 1\,°/s$ was chosen. Again, measurements were performed at different angles to obtain coupling factors for different mounting approaches. This enables a comparison of these.

The tested approaches are: Kapton tape, cable-ties, cable-ties with a Viton tube around the fiber (this approach was used in LPF) and a looped fiber instead of a straight fiber. These mounting approaches are shown in figure 8.10.
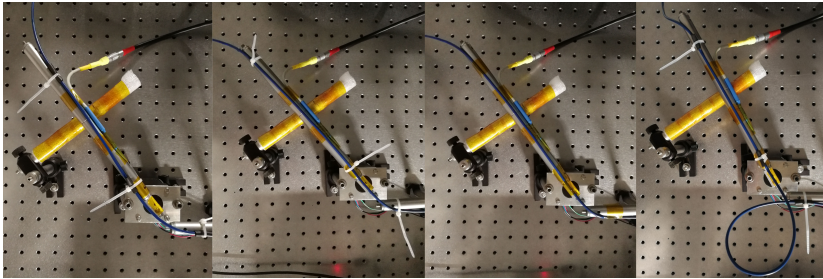
Figure 8.10: Overview of the different fiber mounting approaches tested. From left to right: Cable-ties with additional Viton tube (most tests were done this way), cable-tie only, Kapton tape, fiber loop at the bending position (uses the first mounting approach).

Figure 8.11 depicts the results of such measurements. Here, we can see that the different approaches have an influence on the measured coupling. Table 8.1 lists the fitted coupling factors from these measurements. The fit results show differences in the coupling for the different mounting ap-

Chapter 8

proaches. The measurements with only cable-ties or Kapton tape are within the range of the measurements before. Surprisingly, the measurements with cable-ties supported by a Viton tube show significantly higher coupling than before (at $3.11 \, \text{rad}/°$). Furthermore, the measurement implementing a fiber loop at the rotation point shows significantly reduced coupling ($0.063 \, \text{rad}/°$). Combining these results points to the fact that the coupling strongly depends on how the fiber is mounted. A possible explanation of the high coupling in the case of the cable-tie+Viton mounting is a tighter fit of the cable-ties than before or a smaller bending radius as a result of different placement of the cable-ties.
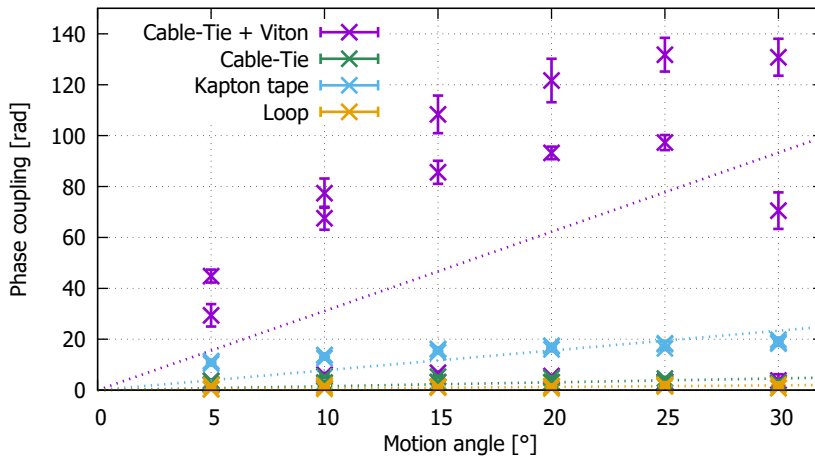
Figure 8.11: Results of the motion-coupling measurements with different fiber mounting approaches: The measurement with the standard mounting approach from before (Cable-Tie + Viton) shows significantly higher values than before, but not for all measurements. This indicates that this mounting approach is dependent on the tightness of the cable-ties. On the contrary, the approach utilizing a looped fiber at the bending point show significantly reduced coupling.

Table 8.1: Fit results for the different mounting methods

Mounting	Cable-Tie	Cable-Tie + Viton tube	Kapton tape	Fiber loop
Coupling [rad/°]	0.15 ±0.02	3.11 ±0.6	0.78 ±0.06	0.063 ±0.008

Taking the simulations performed in chapter 9 and appendix B into account, even the highest value observed while testing the different mounting approaches is uncritical for the performance of the backlink.

Chapter 8

9

Implications for the Backlink

In this chapter, we apply the measured phase dynamics to the simulation that models the noise performance of the PRDS. This results in a realistic phase noise projection for the backlink.

The performance of a DFBL implementation for the EM, as shown in a simplified form in figure 3.7, was simulated in [30] and the PRDS point design [141]. These simulations were performed assuming a total backscatter of 30 ppm and a temperature coupling of $400 \, \mathrm{rad} \, \mathrm{K}^{-1}$. Using a beam splitter of high reflectivity as the last beam splitter before the backlink fiber ($R_{\mathrm{BS4}} = 99.5 \, \%$) shows that the stray light power, and thus, its phase influence can be suppressed such that the requirement is achievable when applying balanced detection which suppresses the stray light contribution from the fiber as explained in section 3.2.4. Figure 9.1 shows this performance. In this simulation, a conservative noise suppression factor of 10 from balanced detection was assumed. Two additional simulations were added, in which the reflectivity of BS4 was reduced to $98 \, \%$ and $50 \, \%$, respectively; these show the increasing performance with the higher reflectivities, as expected, from the resulting increase in the ratio between nominal and straylight beam. This effect is explained in section 3.2.4. The former fulfills the requirement when applying the same balanced detection reduction with the same restriction around $1 \, \mathrm{mHz}$. Similar to these two simulations, the noise correction due to balanced detection is not shown from here onward but applied to a shifted performance goal.
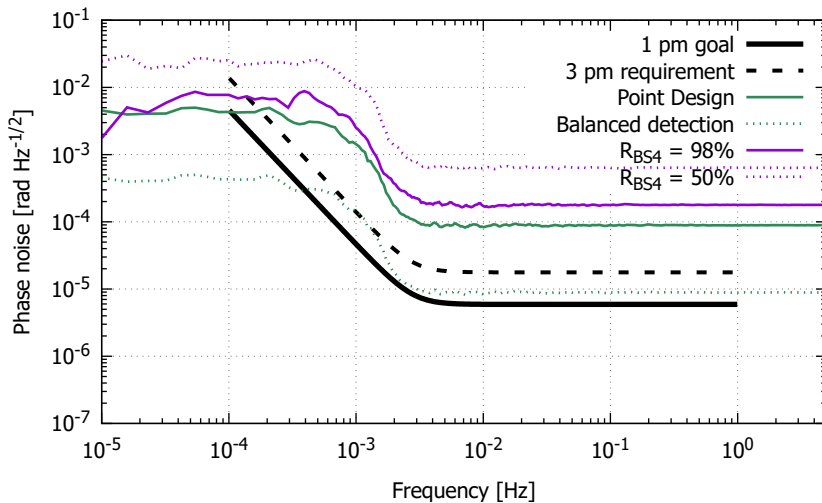
Figure 9.1: Simulated backlink performances using PRDS point design parameters: The simulated performance (green) and the performance after applying a balanced detection correction with a factor of 10 (dotted green) are shown. Using balanced detection fulfills the requirement with a minor break around 1 mHz. Two more performance simulations with less challenging values of BS4 are shown.

From these simulations, a requirement for the thermal stability of the backlink fiber was derived which was set to

$$s_{\text{thermal, backlink}}(f) = 1.4\,\text{mK}/\sqrt{\text{Hz}} \cdot \sqrt{1 + \left(\frac{2.8\,\text{mHz}}{f}\right)^4}, \qquad (9.1)$$

see [141]. Similarly, a requirement for the optical bench was set but with a white noise level of $10\,\mu\text{K}/\sqrt{\text{Hz}}$ [142].

The simulations can be refined with the measured values of the temperature coupling and backscatter for the Fujikura fibers, $80\,\text{rad}\,\text{K}^{-1}\,\text{m}^{-1}$, and $6.5\,\text{ppm/m}$, as observed in chapters 6 and 7. In this simulation, the fiber has an assumed length of 4 m and the fiber interfaces add 1 ppm of additional backscatter.

The refined simulation was performed in reverse: A phase model is derived from the temperature requirement using the temperature-to-phase coupling value measured in this thesis (see section 7.2). Figure 9.2 shows
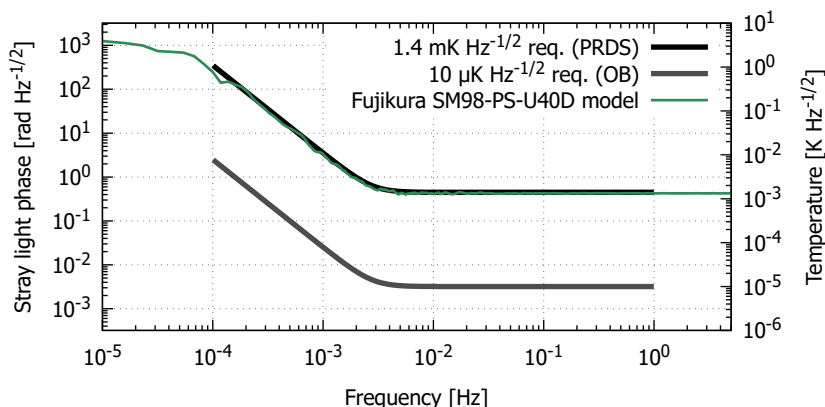
Figure 9.2: Phase noise model for the Fujikura fiber and the backlink temperature requirement. No model for the OB temperature requirement was derived since it is not applicable to the PRDS point design. The temperature induced straylight phase in the order $10^{-1}\,\mathrm{rad}/\sqrt{\mathrm{Hz}}$ is acceptable due to the suppression in the backlink implementation.

the temperature requirement transformed to a phase noise requirement when applying the parameters of the Fujikura fiber as stated above. The result of the refined simulation is a slight decrease in the white noise level and a minimal reduction of the non-linearity around $1\,\mathrm{mHz}$ which is shown figure 9.3. When applying balanced detection with noise suppression of factor 10, we can shift the $1\,\mathrm{pm}/\sqrt{\mathrm{Hz}}$-goal upwards and observe, that the refined simulation is still unable to reach the goal. But in its better performance than the point design, it is clear that the $3\,\mathrm{pm}/\sqrt{\mathrm{Hz}}$-requirement is achieved.

Simulation with the new fiber - Nufern PM1060L

Since a new fiber candidate, the Nufern PM1060L, was chosen for the backlink, such simulations with the new fiber's parameters were performed. This fiber type shows lower temperature coupling $(55\,\mathrm{rad\,K^{-1}\,m^{-1}})$ and backscatter $(2.5\,\mathrm{ppm/m})$, see chapters 6 and 7. In consequence, a performance improvement is expected. The phase model for this simulation is depicted in figure 9.4, here for both temperature requirements. Figure 9.5 depicts the resulting performance of the backlink and com-
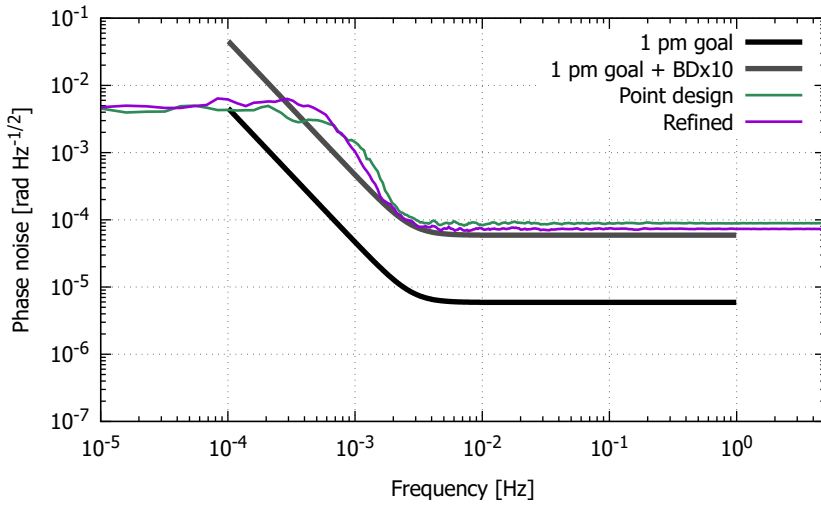
Figure 9.3: Refined simulation with the experimentally verified parameters for a point design-like setup: The simulation with the refined values shows a slightly better noise performance than the assumption in the point design and, in consequence, a fulfilling of the requirement under the application of a noise correction through balanced detection. Nonetheless, the plot shows that the $1\,\mathrm{pm}/\sqrt{\mathrm{Hz}}$-goal is not reached.
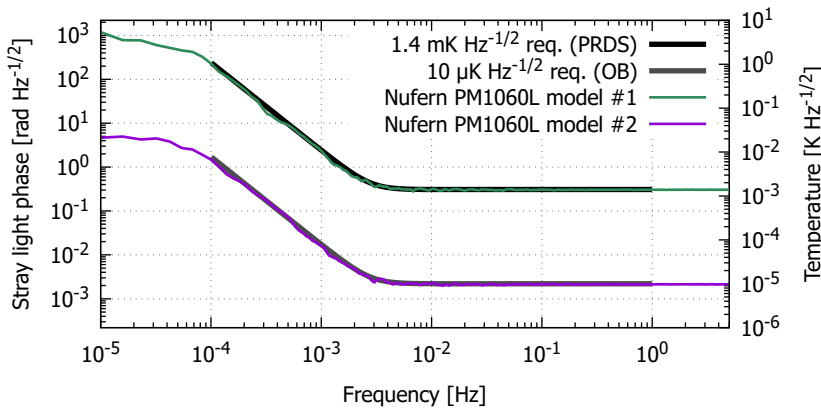
Figure 9.4: Phase noise models for the Nufern PM1060L and both temperature requirements.

pares it to the result from the point design. The simulation shows an improvement of the performance by about a factor of three in the white noise range and a reduction in the non-linear contribution around $1\,\mathrm{mHz}$
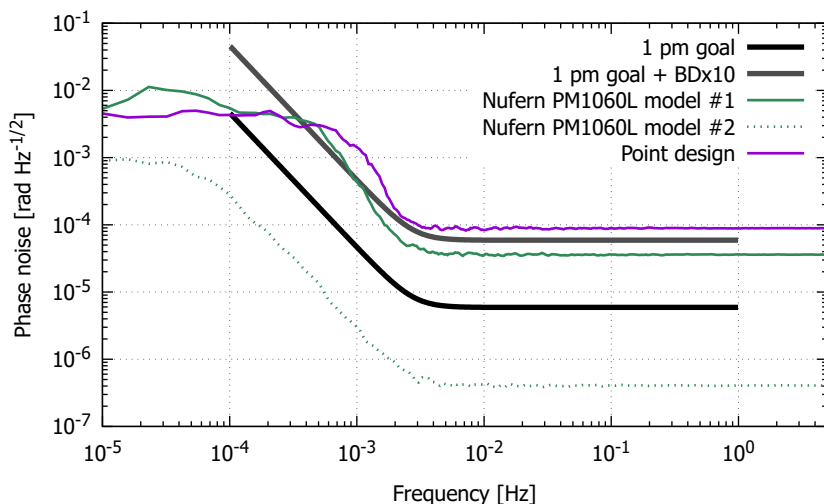
Figure 9.5: Simulated performance of the backlink with the parameters of the Nufern PM1060L for the backlink and the OB temperature requirements. In both temperature regimes, the non-linear contribution is reduced compared to the point design. The performance requirement is not reached without balanced detection for the backlink temperature requirement; with balanced detection, the performance-goal is mostly achieved except for the non-linear contribution which here is around 500 µHz. Compared to the PRDS point design, this plot shows an increase in performance by about a factor of two.

which moves down to around 500 µHz with the Nufern PM1060L. When applying the noise reduction from balanced detection with a factor of 10, the simulations show that the $1\,\mathrm{pm}/\sqrt{\mathrm{Hz}}$ goal is achieved when using the Nufern PM1060L fiber except for the range 400 to 800 µHz as a result of the non-linear coupling; although the goal is not achieved in this range, this simulation shows a significantly improved performance compared to the point design.

Another approach to achieve the $1\,\mathrm{pm}/\sqrt{\mathrm{Hz}}$ goal is tightening the temperature requirements of the backlink fiber. Figure 9.5 shows this when applying the OB requirement to the backlink fiber. The associated phase model is depicted in figure 9.4. The two orders of magnitude stricter requirement improves the expected performance by these two orders of magnitude and overfulfills the $1\,\mathrm{pm}/\sqrt{\mathrm{Hz}}$ goal by about an order of mag-

nitude. This shows that a stricter temperature requirement for the back-link fiber is a fallback option if the desired noise suppression through balanced detection is not achieved. Beyond the overall noise reduction of the stricter temperature requirement, the non-linear contribution around 1 mHz vanishes.

Adding motion into the simulation

Furthermore, the motion coupling that the MOSA actuation induces onto the fiber is added to the simulation. By design, this will happen outside of the measurement band, at $f = 1\,\mathrm{a}^{-1} = 3.17 \times 10^{-8}\,\mathrm{Hz}$, but a noise up-conversion may happen reaching into the frequency band of interest. The motion is added to the simulation with the observed coupling of 1 rad/° at the expected angular change in LISA, i. e. $\pm 1.1°$ [55]. Figure 9.6 compares the result of such a simulation when applying the stricter OB temperature requirement, as a low contribution from the motion seems reasonable due to the low coupling factor between motion and phase. Fortunately, this shows no additional coupling with the expected motion and the observed coupling. Therefore, the motion is negligible in the current design. Appendix B gives an overview of simulations with increased motion coupling, which supports this decision.

Simulations with LISA-like FIOSs

Lastly, the values of a pair of the characterized FIOSs can be used to create a phase model. Figure 9.7 shows the phase model for the pair consisting of FIOS 2A and FIOS 2B (see section 7.3). This model was derived with the combined temperature coupling of the two FIOSs of $106.6\,\mathrm{rad\,K^{-1}}$. For the performance calculation with this model, a total backscatter of 4.7 ppm was assumed, resulting from adding their measured values and the respective measurement error for a conservative estimate. Additionally, 0.5 ppm were added to address the mating sleeve connecting these. The total fiber length in this configuration is 2 m. In addition to the temperature requirements for PRDS and OB, a third model was derived for a temperature level of $0.6\,\mathrm{mK}/\sqrt{\mathrm{Hz}}$. Figure 9.8

shows the resulting performance, which is better than the performance with the Nufern fibers. This results from the shorter total fiber length
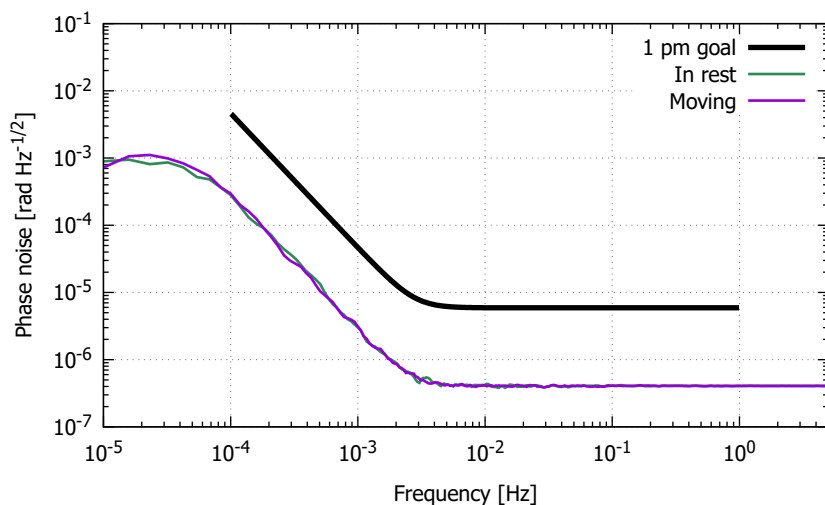
Figure 9.6: Comparison of the performance for the static and moving cases: With motion values as observed in chapter 8, no significant change in performance is observed and, thus, the motion induced phase error is negligible. In the here shown comparison with the stricter OB temperature requirement no balanced detection is necessary to achieve the performance goal.
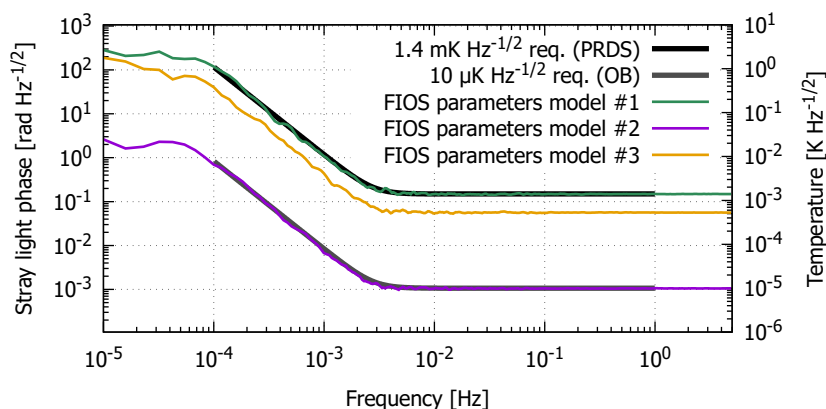
Figure 9.7: Phase models for the FIOS pair 2A+2B for both temperature requirements. Additionally, the orange line shows a phase model for a temperature level of $0.6\,\mathrm{mK}/\sqrt{\mathrm{Hz}}$.
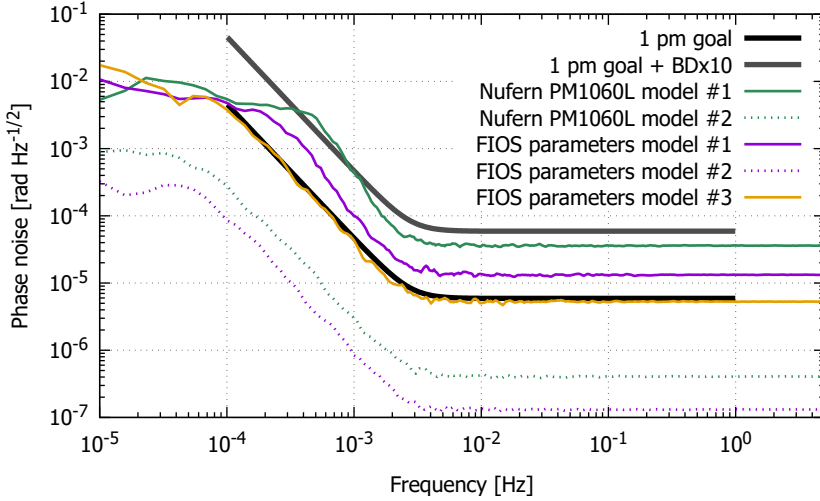
Figure 9.8: Simulated performance of the backlink with the FIOS pair 2A+2B: Compared to the performance with the Nufern fibers, an increase in performance is observed. This is a result of the shorter fiber connection with the FIOS pair. Balanced detection is still required to meet the $1\,\mathrm{pm}/\sqrt{\mathrm{Hz}}$-goal. The expected performance with the $0.6\,\mathrm{mK}/\sqrt{\mathrm{Hz}}$ temperature level is shown in orange which fulfills the performance goal without balanced detection.

and shows that it is favorable to keep the backlink connecting as short as possible. In the case shown here, the performance fulfills the $3\,\mathrm{pm}/\sqrt{\mathrm{Hz}}$-requirement and with $1.3 \times 10^{-5}\,\mathrm{rad}/\sqrt{\mathrm{Hz}}$ is close to the $1\,\mathrm{pm}/\sqrt{\mathrm{Hz}}$-goal without factoring in balanced detection. When applying the usual factor of ten noise suppression by balanced detection, the FIOS pair fulfills the $1\,\mathrm{pm}/\sqrt{\mathrm{Hz}}$-goal over the desired frequency range. With the tighter OB temperature requirement, the performance surpasses the $1\,\mathrm{pm}/\sqrt{\mathrm{Hz}}$-goal significantly, similar to the Nufern fibers shown before. In the simulations with the FIOS pair, the non-linear contribution around $1\,\mathrm{mHz}$ vanishes. Furthermore, the third phase model shows that the $1\,\mathrm{pm}/\sqrt{\mathrm{Hz}}$-goal can be reached without balanced detection when applying a temperature level of $0.6\,\mathrm{mK}/\sqrt{\mathrm{Hz}}$ along the PRDS fiber.

We can conclude for this simulation chapter, that the experimentally observed values result in a slightly better performance than the assumptions of the point design. However, balanced detection remains necessary to

achieve the required and targeted performance with the given temperature requirement. With the new fiber, the Nufern PM1060L, another increase in performance is shown that meets the performance goal of $1\,\mathrm{pm}/\sqrt{\mathrm{Hz}}$ except for a minor non-linear contribution around $500\,\mathrm{\mu Hz}$. Additionally, the simulations reveal that a stricter temperature requirement is a fallback option to achieve the performance goal in the case of less noise suppression by balanced detection.

Summary and Outlook

Fiber dynamics are one of the primary factors limiting the performance in a fiber-based implementation of the LISA backlink. In previous works, fiber backscatter and temperature-related effects were found as the main contributors to this. This thesis introduced a new optical measurement setup to measure the critical fiber dynamics.

The primary aim was to check whether the amount of backscattered power remains constant when the fibers are exposed to ionizing radiation, which will happen when the LISA spacecraft are in orbit. It was deemed necessary to change the fibers connected to the LISA OB. Therefore, radiation measurements were performed twice to verify that the replacement fibers are a valid option. The measurements show that exposure to ionizing radiation does not change the backscattered power for both fiber candidates. This is also true for other fibers of interest, which were tested alongside.

The implementation of the measurement setup of the backscatter dynamics also allows measuring the other relevant fiber dynamics by utilizing additional modulators acting upon the fibers under test. Therefore, the dynamics imprinted on the phase by external temperature and motion influences were studied. For both cases, coupling factors were obtained, which describe the phase change induced by a given amount of temperature change or motion. For the temperature coupling, coupling factors in

the range 35 to 75 ppm were found, depending on the fiber type. Here it is worth noting that the new baseline fiber for the LISA OB shows better performance (i. e., lower coupling) than the previously envisioned fiber. In terms of motion coupling, the coupling was found to be in the order of 1 rad/°. Furthermore, it was found that the motion coupling is highly dependent on the way the fibers are mounted.

Additionally, the polarization states of the backscattered and transmitted beams were analyzed in the linear polarization states. This has shown that the backscattered light features higher polarization fluctuations than the transmitted beam. Mostly, the polarization of the backscattered light equals the polarization launched into the fiber. However, it is possible that the backscattered polarization is orthogonal to the original polarization for short time frames. For LISA, this is uncritical by design as only a single polarization state is planned on the OB after the fiber redundancy units. PBSs will be used to clean the polarization after the fiber connections, thus, reducing the impact of the polarization fluctuations. Nonetheless, high suppression of the "wrong" polarization is required. Otherwise, the backscattered light can introduce small-vector noise.

The temperature and backscatter measurements were also performed with several FIOSs, which will be installed to the PRDS EM. These measurements were in the range of values the fiber-based measurements showed. This verifies that the fiber measurement approach is a valid approach to estimate the performance of the FIOSs beforehand.

With the obtained values for the dynamics, an existing simulation that used estimated values was updated to include the experimentally obtained coupling values. Furthermore, the motion effects were implemented into said simulation resulting in more complete and accurate results. The altered simulations show that switching to the new fiber type is beneficial for the overall performance of the PRDS and that the contribution of the motion is negligibly low or can be removed by post-processing.

The ongoing and future experiments for the PRDS, the TBE and EM, which will show the performance of the PRDS, can be used to measure the fiber dynamics in a more stable environment than in the backscatter

setup, especially the thermal and motion contributions. Furthermore, it seems useful to implement a new setup to refine the motion coupling. Appendix C shows possible setups allowing an improved measurement of the motion coupling.

Appendix

Backscatter Experiment - Additional Informations

A.1 Full setup overviews

This section gives a short overview of the complete setups of the backscatter experiment described in section 5.2 and section 5.4, which is not reduced to the functional principle shown in the aforementioned section. The laser preparation for the original and the upgraded setup is shown in the respective section. In both cases, the S beam is drawn in orange, the LO in violet, the backscattered light in turquoise, and the beam that would result in the calibration beam in pink. Both cases depict the respective setup in the backscatter mode.

A.1.1 Original setup

The LO had only one function in the original setup: Interfering with the backscattered light. Thus the LO propagates only to the recombination beamsplitter. The S beam, on the other hand, hits a beam splitter as the first component that divides the beam into the two paths: The nominal path towards the fiber side of the backscatter measurement (here the beam is depicted orange) and the path that results in the calibration beam in pink. This beam leads in the opposite direction through the fiber. This is depicted in figure A.1. Four PRs measure different signals:
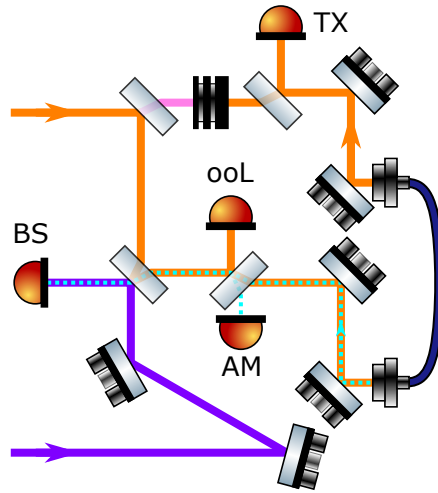
Figure A.1: Interferometer overview of the original backscatter setup:
The LO is depicted in violet, the signal beam in orange, and the backscattered power dotted in turquoise.

BS measures the heterodyne signal from which the backscattered signal
is reconstructed, TX the transmitted power to scale the backscattered
power, and AM offers another approach to measure the backscattered
signal by applying amplitude modulation to the S beam. This was, how-
ever, not used in the end as the backscattered signal was too small for a
DC-type measurement. The last PR, ooL, is an out-of-loop measurement
of the S beam's amplitude stability, thus, an auxiliary signal.

A.1.2 Upgraded setup

In the upgraded setup, the LO feeds three interferometers instead of one
and thus is split into several beams. Most of the power is sent into the
backscatter interferometer consisting of the PRs BS_s and BS_p. For
the S beam, the out-of-loop detector was moved to the laser preparation,
the original port, where this PR was placed, is free and, thus, used to
feed the reference interferometer. This approach has the disadvantage
that the reference interferometer is not available in the calibration mode
but results in a higher power in the fiber under test and retains the
AM port for the backscatter measurement. In the transmit port, an

interferometer was added as well, allowing measurements of power (on PR TX) and phase (on the PRs TX_s and TX_p). The AM measurements
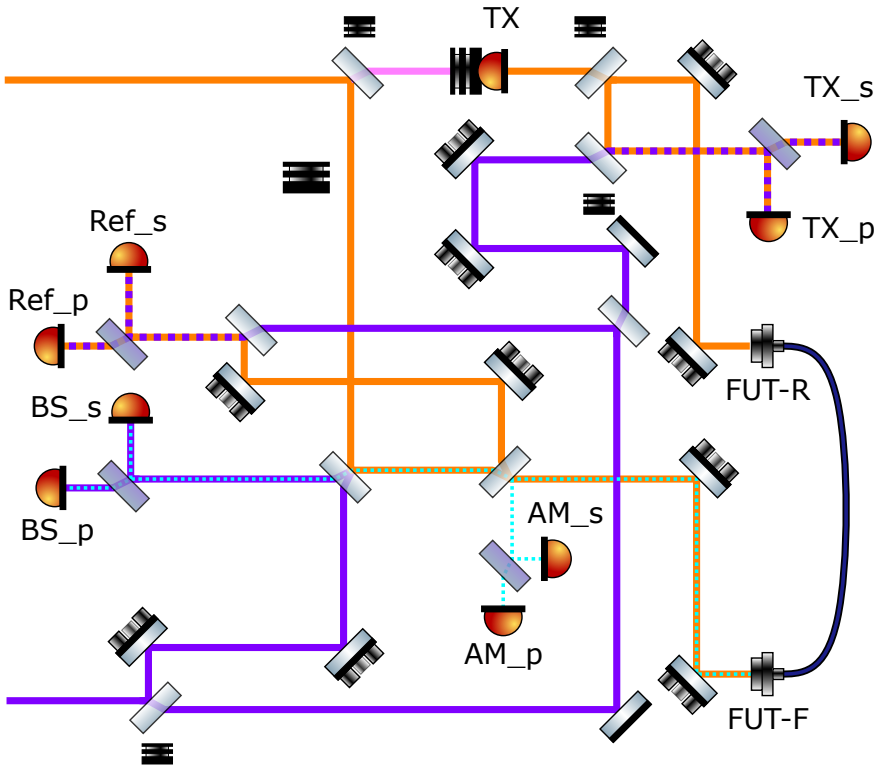
Figure A.2: Interferometer overview of the upgraded backscatter setup

were, however, not performed as the exchanged two-stage TIA with signal splitting into AC and DC parts was too noisy. Thus, no usable signal was observable. Furthermore, the strong fluctuations in the backscatter signal indicate that an amplitude modulation might not be resolvable and, therefore, the backscattered power is not measured.

A.2 Error derivation

This section derives the error calculus for the backscattered power in equation (5.2). We start with the general formula of the propagation of uncertainty [143, 144], given as

$$s_X = \sqrt{\sum_k \left(\frac{\partial X}{\partial v_k}\right) s_{v_k}^2}. \tag{A.1}$$

Here, s_X is the standard deviation of the variable X which depends on the variables v_k. Lastly, s_{v_k} is the standard deviation belonging to the variable v_k.

First, we have to estimate the error of the heterodyne efficiency, see equation (5.1), as the calculus to obtain the backscattered power requires this value. As the resulting equation is relatively long, we list the derivative terms in table A.1.

Table A.1: Derivative terms in the error formula for the heterodyne efficiency.

Variable X	$\frac{\partial X}{\partial v_k}$
$U_{\mathrm{AC,cal}}$	$\frac{1}{R^2 \mathcal{R}^2} \frac{U_{\mathrm{AC,cal}}}{2 P_{\mathrm{LO}} P_{\mathrm{cal}} \rho^2 \tau^2}$
P_{LO}	$-\frac{1}{R^2 \mathcal{R}^2} \frac{U_{\mathrm{AC,cal}}^2}{4 P_{\mathrm{LO}}^2 P_{\mathrm{cal}} \rho^2 \tau^2}$
P_{cal}	$-\frac{1}{R^2 \mathcal{R}^2} \frac{U_{\mathrm{AC,cal}}^2}{4 P_{\mathrm{LO}} P_{\mathrm{cal}}^2 \rho^2 \tau^2}$
ρ	$-\frac{1}{R^2 \mathcal{R}^2} \frac{U_{\mathrm{AC,cal}}^2}{2 P_{\mathrm{LO}} P_{\mathrm{cal}} \rho^3 \tau^2}$
τ	$-\frac{1}{R^2 \mathcal{R}^2} \frac{U_{\mathrm{AC,cal}}^2}{2 P_{\mathrm{LO}} P_{\mathrm{cal}} \rho^2 \tau^3}$
R	$-\frac{1}{R^3 \mathcal{R}^2} \frac{U_{\mathrm{AC,cal}}^2}{2 P_{\mathrm{LO}} P_{\mathrm{cal}} \rho^2 \tau^2}$
$\mathcal{R}$	$-\frac{1}{R^2 \mathcal{R}^3} \frac{U_{\mathrm{AC,cal}}^2}{2 P_{\mathrm{LO}} P_{\mathrm{cal}} \rho^2 \tau^2}$

After obtaining the error of the heterodyne efficiency, we can apply the propagation of uncertainty to equation (5.2) and obtain the error of the backscattered power. Again, we list the resulting derivative terms in table A.2.

Table A.2: Derivative terms in the error formula for the backscattered power.

Variable X	$\frac{\partial X}{\partial v_k}$
$U_{\mathrm{AC,bs}}$	$\frac{1}{R^2\mathcal{R}^2}\frac{U_{\mathrm{AC,bs}}}{2P_{\mathrm{LO}}\eta\rho^2\tau^2\tau_{\mathrm{pp}}^2}$
P_{LO}	$-\frac{1}{R^2\mathcal{R}^2}\frac{U_{\mathrm{AC,bs}}^2}{4P_{\mathrm{LO}}^2\eta\rho^2\tau^2\tau_{\mathrm{pp}}^2}$
η	$-\frac{1}{R^2\mathcal{R}^2}\frac{U_{\mathrm{AC,bs}}^2}{4P_{\mathrm{LO}}\eta^2\rho^2\tau^2\tau_{\mathrm{pp}}^2}$
ρ	$-\frac{1}{R^2\mathcal{R}^2}\frac{U_{\mathrm{AC,bs}}^2}{2P_{\mathrm{LO}}\eta\rho^3\tau^2\tau_{\mathrm{pp}}^2}$
τ	$-\frac{1}{R^2\mathcal{R}^2}\frac{U_{\mathrm{AC,bs}}^2}{2P_{\mathrm{LO}}\eta\rho^2\tau^3\tau_{\mathrm{pp}}^2}$
τ_{pp}	$-\frac{1}{R^2\mathcal{R}^2}\frac{U_{\mathrm{AC,bs}}^2}{2P_{\mathrm{LO}}\eta\rho^2\tau^2\tau_{\mathrm{pp}}^3}$
R	$-\frac{1}{R^3\mathcal{R}^2}\frac{U_{\mathrm{AC,bs}}^2}{2P_{\mathrm{LO}}\eta\rho^2\tau^2\tau_{\mathrm{pp}}^2}$
$\mathcal{R}$	$-\frac{1}{R^2\mathcal{R}^3}\frac{U_{\mathrm{AC,bs}}^2}{2P_{\mathrm{LO}}\eta\rho^2\tau^2\tau_{\mathrm{pp}}^2}$

A.3 Frequency modulation

In the beginning stages of the backscatter experiment, a modulation of the laser frequency was implemented to alter the phase relation between scattering points within the fiber. Thus, to use the fiber's etalon properties. Figure A.3 shows an exemplary time-series of a backscatter measurement with laser frequency modulation. In this example, the laser frequency was modulated with a repetition frequency of 0.1 Hz. In comparison to figure 5.11 (a), this shows a distinct feature with the repetition frequency (and one on the harmonic of it) which results in a strong modulation of the backscattered signal (note: the fiber used in the frequency modulated case was of the Fujikura type). It is important to note that this deviates from the response of a cavity to scanning the laser frequency.

In addition to this deviation, the modulation strength varies between different fibers, which is likely a result of slight differences in the fiber length and results in some cases in no noticeable impact on the measured time-series. Compared to the strong and reliable modulation of the backscattered signal as a result of the temperature modulation, the frequency modulation is not beneficial and, therefore, it was decided to
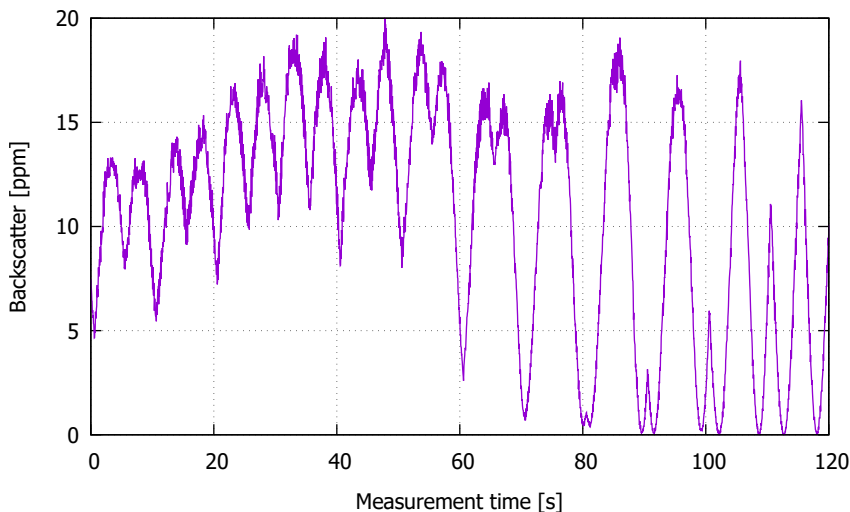
Figure A.3: Exemplary time-series of a frequency modulated backscatter measurement: The frequency modulation results in a oscillation of the backscattered signal with the repetition frequency and some harmonic contribution.

not utilize the frequency modulation and only to rely on the temperature modulation.

A.4 Radiation No 1: Broken Fujikura fiber

In the first radiation campaign, four Fujikura fibers were originally tested. However, in the evaluation of these measurements in section 6.1.1, only three were considered for evaluation. This was done as one of the fibers was damaged over the measurements. Figure A.4 shows the evolution of this fiber over the different steps. The first measurements, reference, and the first two radiation steps agree with the remaining fibers. Before or after the third radiation step, the fiber was damaged during handling. This is depicted in the figure by the turquoise vertical dashed line. After that, the transmission dropped by about 15 %, and the backscattered power did not agree with the measurements of the remaining fibers.
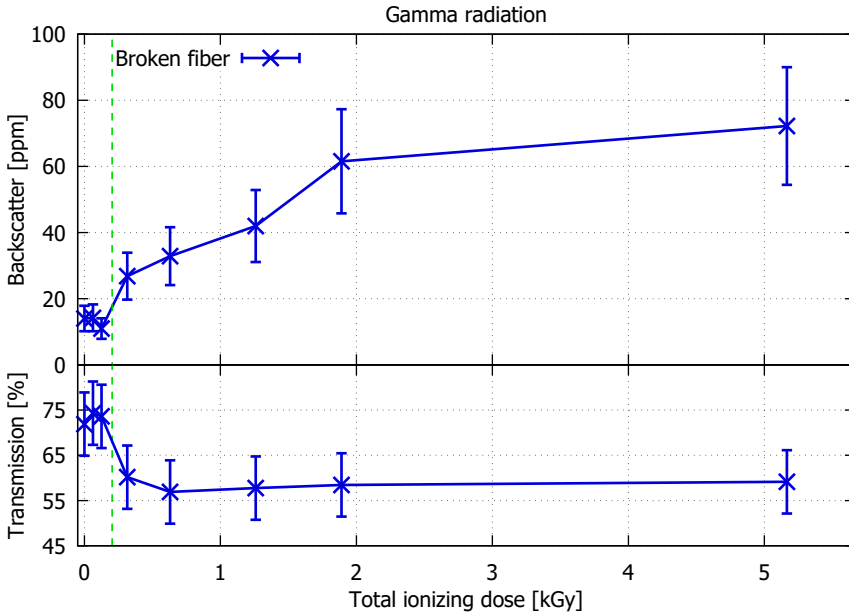
Figure A.4: Measurement results for the broken Fujikura PMF: The dashed green line indicates between which measurement the damage occurred. Before that the measurements are within range of the measurement with the other fibers. However, after that the backscattered signal increases significantly while the transmission decreased.

After the damaging occurred, the backscattered power subsequently increased with each step. It is unclear if this increase is caused by additional radiation-induced damages or a settling effect of the damage within the fiber.

Before the damage occurred, the highest backscatter value here was 14.2 ± 4.1 ppm which is lower than the highest value observed in section 6.1.1 and thus in agreement with the other measurements.

Appendix A

$\mathcal{B}$

Performance Simulation with Higher Coupling

This chapter presents simulation results with an increased motion-to-phase coupling. These altered simulations were performed since the measurements of the motion coupling are just an estimate of the coupling's order of magnitude and might deviate significantly from the actual coupling depending on the mounting and the general routing of the fiber. The increased coupling in these additional simulations ranges from an increase by a factor of ten to a thousand.

Figure B.1 shows the phase models for the simulations with higher motion coupling. These models are derived from the phase model of the motion-including simulation in chapter 9. However, the motion contribution is added into the model after a filter that removes long-term drifts to make it more visible. The resulting phase models show similar white noise for all cases, but an increasing contribution in the lower frequency range as the motion coupling is increased.

Figure B.2 shows the resulting performance when applying these phase models. The shape remains unchanged in the requirement's frequency range when increasing the motion coupling. However, a non-linear contribution arises below the requirement's frequency range (below 10^{-4} Hz), which increases with stronger motion coupling. None of the shown results violates the requirement. Furthermore, the motion shows itself in the phase as a slow, long-term drift. Therefore, post-processing can remove
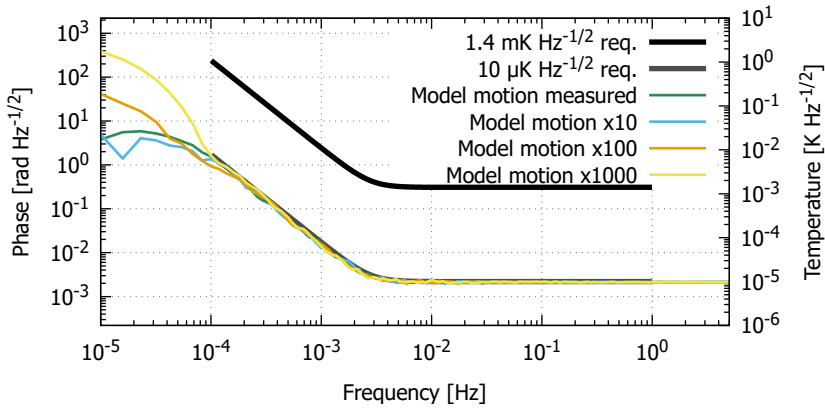
Figure B.1: Phase models for the simulations with increased motion coupling: The models are derived from the OB temperature requirement and show similar white noise but different contributions in the lower frequency range.
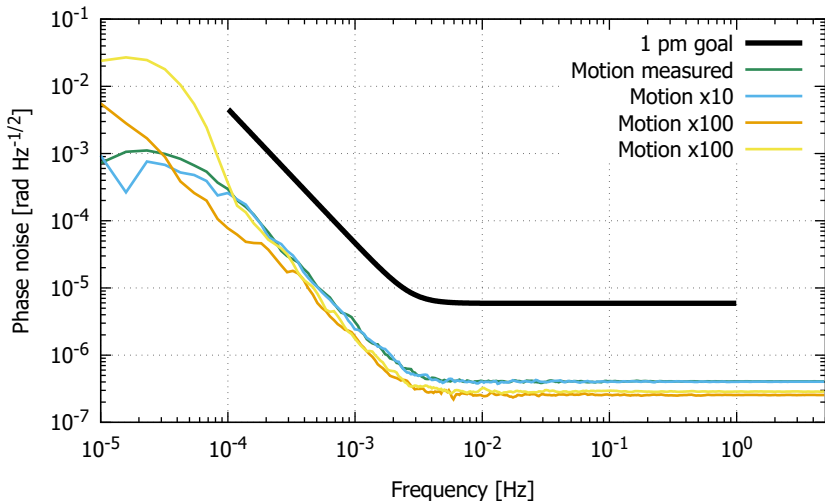
Figure B.2: Comparison of the performance with different amounts of motion coupling. The increase in motion needs to be significant to cause a distinct change in the noise performance. The difference in the white noise level results from spectral estimation.

the influence on the phase signal (i. e., linear detrending as the sinusoidal term results in a linear contribution due to its tiny amplitude). It is important to note that all cases with increased motion values were per-

formed with the same set of parameters describing the white and $1/f^2$ noise contributions. Therefore, the difference in the white noise levels shown in figure B.2 results from the spectral evaluation methods.

Appendix B

C

Improved motion measurement setup

This chapter proposes improved setups to measure the motion-to-phase coupling, which was measured with the motion mock-up (see chapter 8). The primary aim of these setup ideas is to remove the not obtainable influence of the "loose" fiber ends in the motion mock-up.
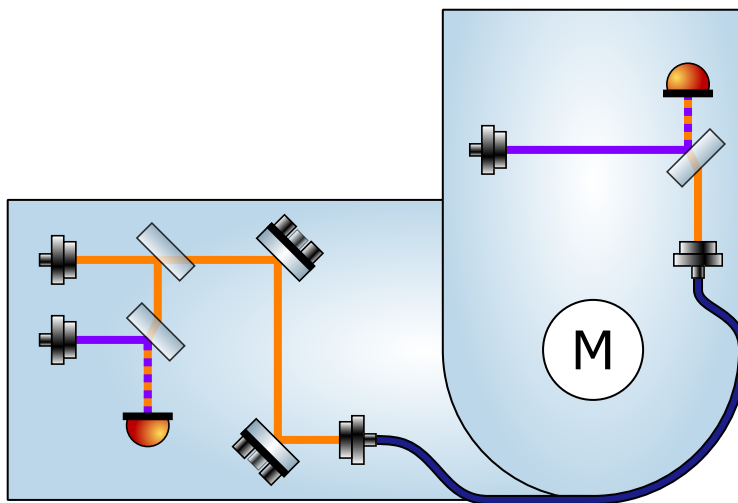
Figure C.1: Motion setup - Alternative 1: A bread board is rotated with respect to the primary part by a stepper motor. The phase effect of the fiber's motion is observed on the moving part. This removes the "loose" end of the fiber under motion but adds another source of spurious motion in the delivery fiber of the LO.

Figure C.1 shows an approach using two breadboards, one of which rotates with relative to the other using a stepper motor. The fiber under test is mounted to the corner between the two breadboards. The LO is distributed to both breadboards using fibers and a fiber beam splitter. The problem with this approach is that the fiber connection delivering the LO to the moving breadboard will also undergo motion and, therefore, introduce a spurious phase contribution from this delivery fiber's motion.
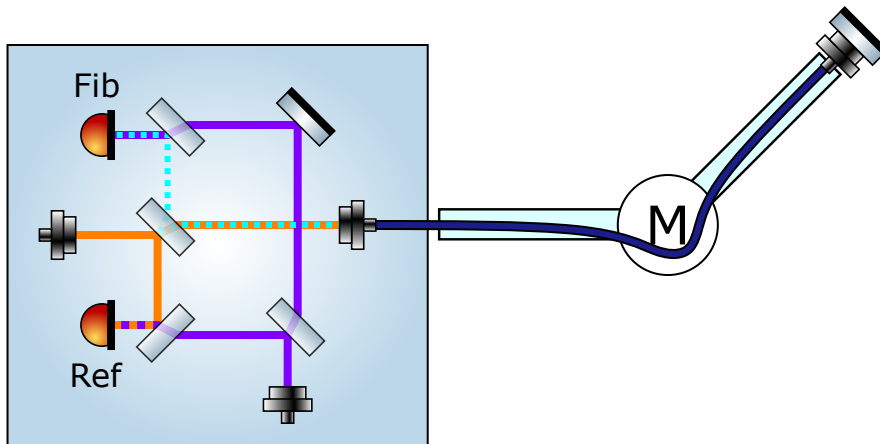
Figure C.2: Motion setup - Alternative 2: All interferometers are located on a single bread board and the fiber is routed over two lever arm, one fixed and one moving. At the end of the fiber, a mirror is placed such that the beam is reflected back into the fiber.

The approach in figure C.2 resolves this problem by replacing the second breadboard with a fiber coupler and a mirror. In this configuration, the beam transmitted through the fiber is directly reflected back into the fiber. An additional benefit of this approach is that it is more similar to the LISA backlink's fiber configuration regarding the motion/bending points. Although this approach has only one bending point along the fiber, two are in the optical path.

Continuing this approach leads to figure C.3: Instead of the pair of fiber coupler and mirror at the end of the moving arm, the fiber is routed back along both arms to the launching breadboard. This results in the LISA
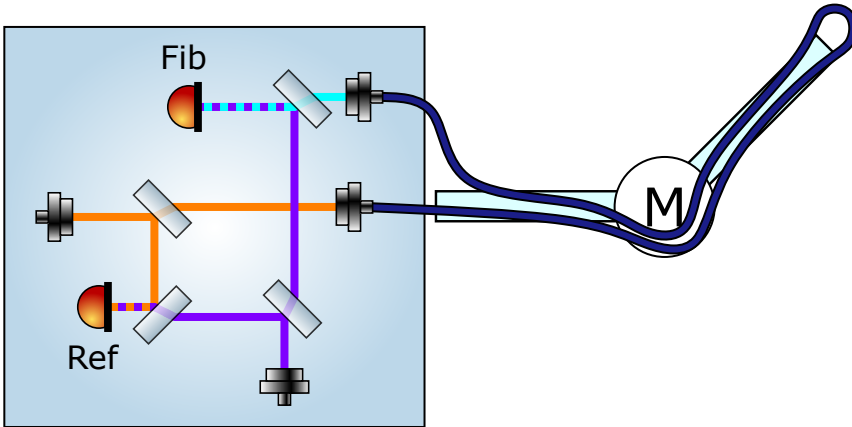
Figure C.3: Motion setup - Alternative 3: An evolution of alternative 2, instead of placing a mirror at the fibers end, the fiber is routed over the lever arms twice and a second fiber coupler is placed onto the bread board to create the post-fiber interferometer (Fib).

backlink-like fiber configuration of two bending points. In this setup, no spurious fiber motion is induced.

$\mathcal{D}$

Motion measurements in the LDPN experiment

D.1 The laser test stand

The laser differential phase noise (LDPN) experiment, or the laser test stand, is an experiment to measure and verify the phase fidelity of the LISA laser candidates. In consequence, the LDPN experiment is capable of accurately measuring phases.

In the laser test stand, the device under test, i. e. the LISA laser candidate, consists of three parts: A seed laser (L1), an electro-optic modulator (EOM) and a fiber amplifier. The EOM imprints a 2.4 GHz sideband onto the beam, and a second laser (L2) is offset locked to L1's beam with an offset of 1.6 kHz. Each PR has two signal outputs, one for the 2.4 GHz signal, called UHF, and one for the 1.6 kHz signal, called AF. Combinations of different PR signals on the same or different outputs reveal the desired information about the phase fidelity. This is described in-depth in [145, 146].

For the motion measurements using the laser test stand only the capability of accurate phase measurements is necessary. Instead of implementing a fiber amplifier, the motion mock-up was inserted at its position.
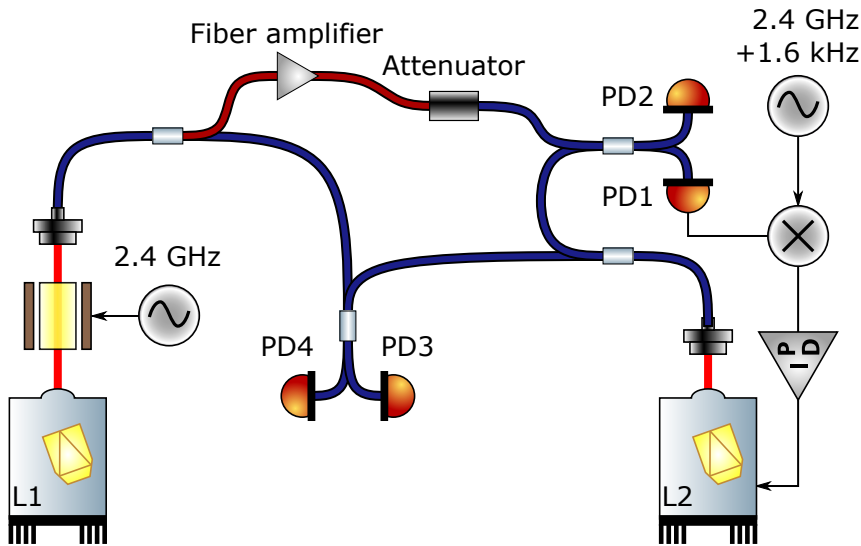
Figure D.1: Simplified overview of the measurement setup of the LDPN experiment, laser L1, the EOM, and the fiber amplifier form the device under test, i. e., the LISA laser candidate. The fiber amplifier is depicted in red.

D.2 Phase contributions

The usual evaluation of the LDPN experiment happens as spectral analysis in the LISA frequency band. Figure D.2 shows such spectra of the differential phase noise comparing the moved to the resting case. The motion shows itself in a peak at the motion frequency, here at about 0.4 Hz. In addition, harmonics of that are visible in the phase signal. Furthermore, figure D.3 shows excerpts of the measurements as a time series. Although the motion-induced signal is in the same order of magnitude as the phase noise in the resting case, the measurement depicts the sinusoidal contribution of the motion. This time-series shows a coupling of about 0.4 mrad peak-to-peak for a motion amplitude of about 6°. This is significantly lower than the coupling observed in section 8.3. Furthermore, section 8.5 has shown that the coupling is strongly dependent on the mounting approach. The measurement shown here was performed with an older iteration of the motion mock-up. In this iteration, the moving lever is not directly moved by the stepper motors but over a conrod.
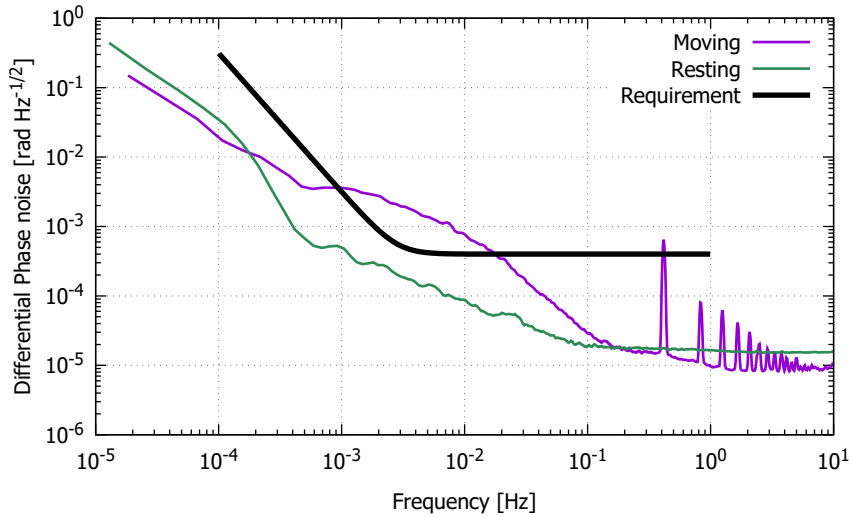
Figure D.2: Spectral evaluation of the phase in the LDPN experiment in the moved and resting cases: Compared to the unmoved case, the measurement under motion shows an increase in noise around the corner of the requirement and a peak at the motion frequency. Furthermore, peaks at the harmonics of the motion frequency are also visible in the spectrum.

The fiber mounting was done using Kapton tape with a wide separation of the fixing points around the bending point. All this can explain the relatively low coupling here, as these factors reduce the stress on the fiber as a result of the motion.

Appendix D
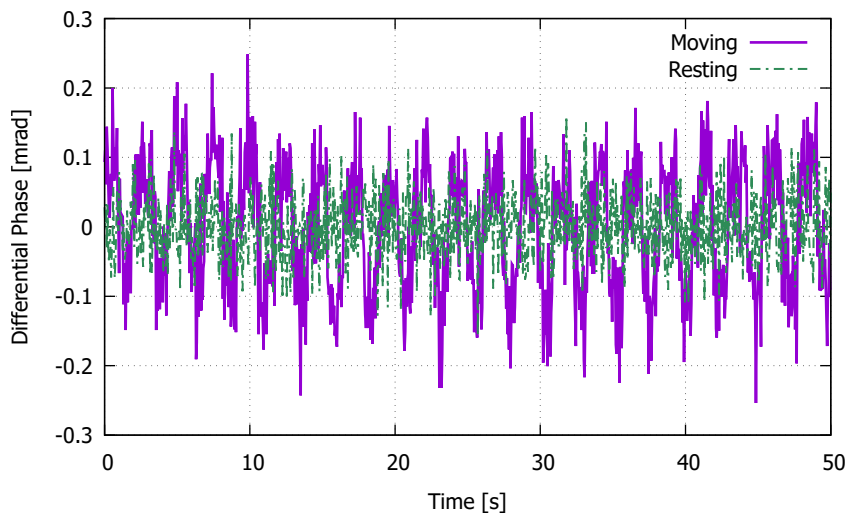
Figure D.3: Time-series of the phase in the LDPN experiment in the moved and resting cases: Although the signal in the moving case is in the same order of magnitude as the noise in rest, the motion frequency is clearly visible in the time-series of the motion measurement. A motion coupling of about 0.4 mrad peak-to-peak is observed.

$\mathcal{E}$

Fiber Frequency Stabilization

E.1 Idea

Many optical experiments require a stable optical frequency of the laser light in use [147–149]. However, the laser frequency will fluctuate depending on environmental conditions [150]. There are different approaches to stabilize the laser frequency: Very commonly used is the Pound-Drever-Hall technique using a cavity as frequency reference [151]. Another approach is to use a Mach-Zehnder interferometer (MZI) with unequal armlength, which is susceptible to laser frequency noise. This can be used to measure the laser frequency noise and, by stabilizing the interferometer's output, reduce the laser frequency noise, as done in [152].

The idea behind the fiber Mach-Zehnder interferometer (FMZI) is an easy to implement and lightweight approach with a fiber-based implementation. This was started by interference problems in the backscatter setup (see chapter 5) which ultimately was not required in said experiment. However, the investigations continued since a lightweight approach is interesting for space-flight which is given by choice of the fiber based approach. This approach is also interesting for its simplicity in implementation and subsequently could be used in other experiments that use bonded MZIs for frequency stabilization.

Other approaches to create a lightweight, fiber-based frequency stabilization exist [153, 154], which use a fiber-based Michelson interferometer to create a frequency reference.

E.2 Setup
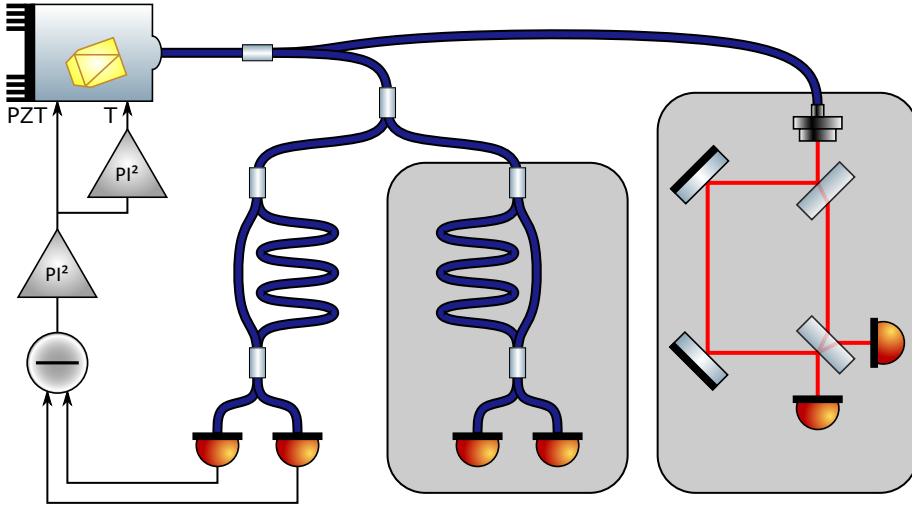
Figure E.1: Experimental setup of the fiber frequency stabilization: A small part of the laser light to stabilize is split off and sent to the stabilization interferometers with different arm lengths. The primary interferometer is used to stabilize the laser, and the secondary interferometer acts as an out-of-loop sensor. The controller consists of two stages, one controlling the fast piezo and the other one the temperature of the laser crystal for slower actuation.

A fiber tap-off is implemented into the beam to stabilize and, subsequently, a small fraction of the beam's power is sent to the MZIs of unequal arm-length. The setup features an arm length difference of

$$\Delta L_{\text{geometric}} = 5\,\text{m} \rightarrow \Delta L_{\text{optical}} = n_{\text{Fiber}} \cdot \Delta L_{\text{geometric}} \simeq 7.25\,\text{m}$$

with a refractive index $n \simeq 1.4496$ for the silica fiber (refractive index calculated according to [155]). Two interferometers are used to have an out-of-loop measurement of the stabilization system. The remaining light,

which was not sent into the stabilization interferometers, is sent to the application requiring the stabilized light.

A PI^2-style controller is used to drive the laser's piezo, resulting in a change of the frequency in the emitted beam. This controller features two integrators to increase the gain in the lower frequencies. In addition, the signal going to the laser piezo is split and passed through a low-frequency controller acting on the temperature of the laser crystal. This can create a large frequency change and is used to compensate for long-term frequency drifts, which, in consequence, allows that the piezo is only driven with low voltages and not required to be largely offset from its idle position. This setup is depicted in figure E.1.

E.3 Maths

The laser frequency noise couples into the phase readout over the difference in arm-length [152]. Using equation (2.2) and adding laser frequency noise (in its angular description) $\delta\omega$ to it results in

$$E(\vec{r}, t) = \vec{E}_0 \exp\left(i(\vec{k} \cdot \vec{r} - (\omega + \delta\omega)t + \varphi)\right).$$ (E.1)

Here, the opto-geometrical factor is consumed into the amplitude $\vec{E}_0$, which, in consequence, is complex. Interfering two such amplitudes, $\vec{E}_1$ and $\vec{E}_2$, which are generated from a source beam using a beamsplitter, after propagating these over different paths with a length difference ΔL results in

$$\begin{pmatrix} \vec{E}_3 \\ \vec{E}_4 \end{pmatrix} = M_{\text{bsp}} \cdot \begin{pmatrix} \vec{E}_1 \cdot e^{-i(\omega+\delta\omega)\frac{L}{c}} \\ \vec{E}_2 \cdot e^{-i(\omega+\delta\omega)\frac{L+\Delta L}{c}} \end{pmatrix}$$

$$= \begin{pmatrix} \rho_2 \cdot \vec{E}_1 \cdot e^{-i(\omega+\delta\omega)\frac{L}{c}} + i\tau_2\vec{E}_2 \cdot e^{-i(\omega+\delta\omega)\frac{L+\Delta L}{c}} \\ i\tau_2 \cdot \vec{E}_1 \cdot e^{-i(\omega+\delta\omega)\frac{L}{c}} + \rho_2\vec{E}_2 \cdot e^{-i(\omega+\delta\omega)\frac{L+\Delta L}{c}} \end{pmatrix}.$$ (E.2)

Detectors placed in each output port of the beamsplitter measure the following power:

$$
\begin{pmatrix} P_3 \\ P_4 \end{pmatrix} \propto \begin{pmatrix} |\vec{E_3}|^2 \\ |\vec{E_4}|^2 \end{pmatrix}
$$
$$
= |\vec{E_0}|^2 \begin{pmatrix} \rho_1^2\rho_2^2 + \tau_1^2\tau_2^2 - 2\rho_1\rho_2\tau_1\tau_2 \cos\left(\frac{\Delta L(\omega + \delta\omega)}{c}\right) \\ \rho_2^2\tau_1^2 + \rho_1^2\tau_2^2 + 2\rho_1\rho_2\tau_1\tau_2 \cos\left(\frac{\Delta L(\omega + \delta\omega)}{c}\right) \end{pmatrix} . \quad \text{(E.3)}
$$

The difference of the - to a voltage converted - powers contains the frequency noise:

$$
\Delta U = U_4 - U_3 = \kappa \cos\left(\frac{\Delta L(\omega + \delta\omega)}{c}\right) \quad \text{(E.4)}
$$

where $U_{3,4}$ correspond to the converted signal from the powers $P_{3,4}$ and κ is a constant combining the starting power and the properties of the PR. As ω is in the THz-range, a standard photodiode cannot resolve the contribution thus the measured signal is given by

$$
\Delta U = \kappa \cos\left(\frac{\Delta L \delta\omega}{c}\right). \quad \text{(E.5)}
$$

Applying the arcus-cosine to this function results in an expression for the frequency noise:

$$
\delta\omega = \frac{c}{\Delta L} \arccos\left(\frac{\Delta U}{\kappa}\right). \quad \text{(E.6)}
$$

E.4 Results

Figures E.2 and E.3 show measurement results for the setup as shown in figure E.1. These measurements are about half an hour or a day-long, respectively, and show that the noise is reduced when the controller is active. In the case of the out-of-loop measurement, the noise is reduced by 1-2 orders of magnitude. In the shorter measurement, the in-loop measurement shows a noise suppression of up to six orders of magnitude, down to about $30\,\mathrm{Hz}/\sqrt{\mathrm{Hz}}$ at the higher frequency end of the measurement. However, in the longer measurement, this performance was not

reached and was not reached overall again. Performance-wise, the longer measurement shows the same noise reduction above 2×10^{-3} Hz by up to two orders of magnitude in the out-of-loop measurement. However, the in-loop noise is significantly higher, in the order of 20 kHz.
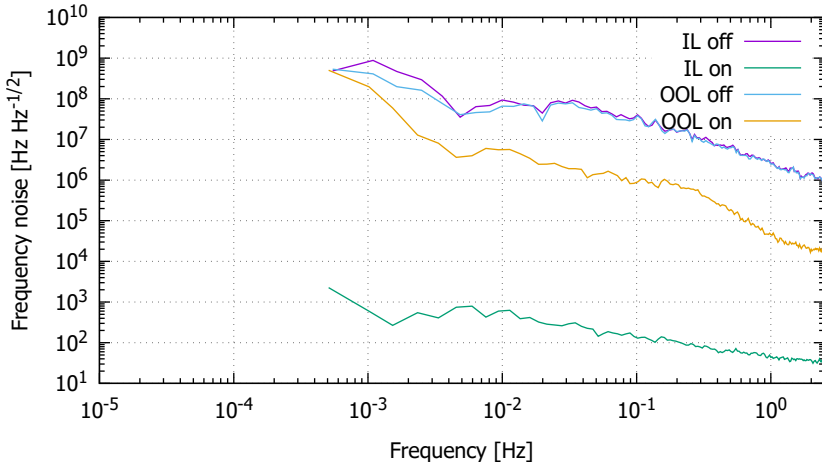
Figure E.2: Frequency noise of two 30 min measurements with active and inactive controller: The out-of-loop (OOL) noise is suppressed by up to two order of magnitude, in-loop (IL) the suppression reached up to six orders of magnitude.

Furthermore, comparing the shape of the out-of-loop noise curves to the temperature noise measured with an NTC sensor within the insulating box indicates that temperature noise limits the performance. Figure E.4 shows the temperature stability in the lab and the insulating box.

Concluding, this shows that a frequency stabilization using a fiber-based Mach-Zehnder interferometer with mismatched arm lengths can be used to stabilize the frequency of a laser. However, the measurements presented here show several problems with the current setup: The controller is not working properly at all times, thus, resulting in too high in-loop noise. The optical setup is not sufficiently shielded from temperature effects within the insulating box and, thus, is limited in performance by temperature noise. As this stabilization was not required to run the backscatter setup and other measurements were more urgent, the development of the FMZI was halted.

Appendix E
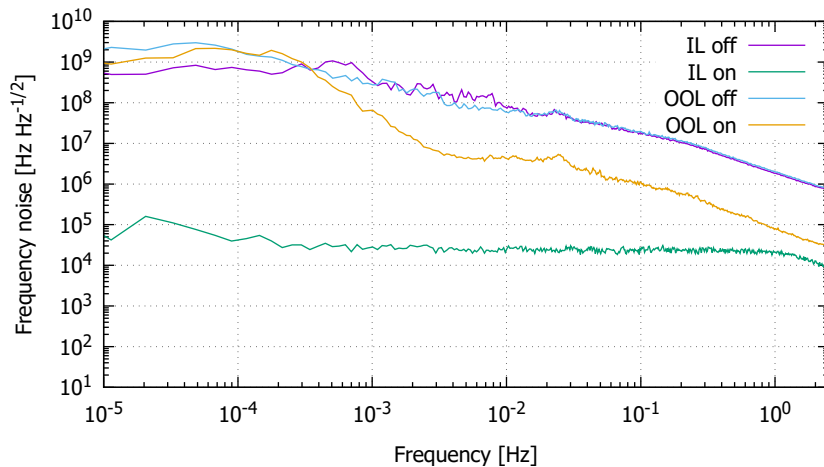
Figure E.3: Frequency noise of two measurements, of about a day, with active and inactive controller: The out-of-loop noise suppression is about the same as for the shorter measurement before, however, the in-loop suppression is significantly less.
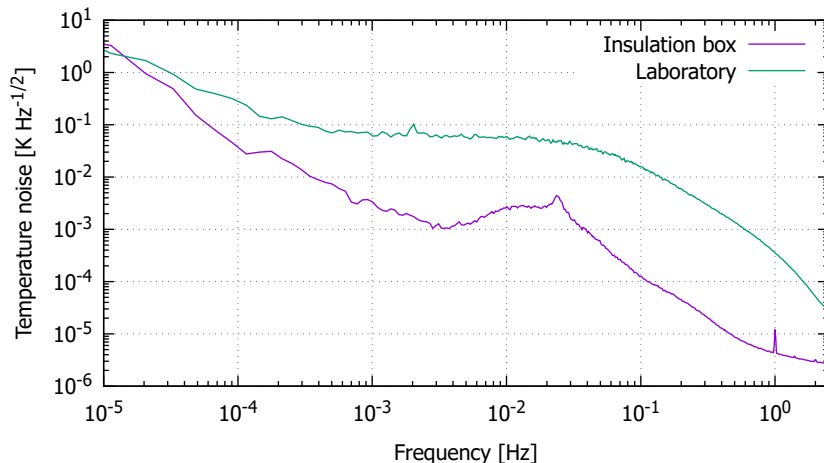
Figure E.4: Temperature noise in the laboratory and the insulating box.

$\mathcal{F}$
Software Phasemeter

This chapter gives a short overview of the essential parts of the code required to run the software phasemeter of the backscatter setup.

In the dual DAQ configuration, the data acquisition is started in two threads. Not shown in the code excerpt are some lines defining the data saving location and the input of some information regarding the measurement over the command line.

```
1  /* This is an excerpt of the int main() */
2  con.generateGUI();
3  // Start data acquisition
4  std::thread t1(&DAQ::continuosMeasure, daq0),
5    t2(&DAQ::continuosMeasure, daq1);
6  // Loop until a key was pressed: refresh the values shown
7  while (!_kbhit()) {
8    for (int c = 0; c < 8; c++) {
9      con.update(0, c, daq0->conOut[c]);
10     con.update(1, c, daq1->conOut[c]);
11   }
12 }
13 daq0->stop();
14 t1.join();
15 daq1->stop();
16 t2.join();
```

The actual data acquisition is based on the Universal Library shipped with the DAQ [123]. The different DAQ are registered over the board-Num, and each one is an object for itself.

```
1  int DAQ::initialize() {
2    // Initialize the board
3    ulStat = cbDeclareRevision(&rev);
4    // Initiate error handling - from example ULAI01.c
5    // Write all ERRORs and WARNINGs, run the program "forever
        "
6    cbErrHandling(PRINTALL, DONTSTOP);
7    // load A/D resolution
8    cbGetConfig(BOARDINFO, boardNum, 0, BIADRES, &adRes);
9
10   if (adRes != DEFINED_ADRES)
11     return -1;
12   return 0;
13 }
```

The actual read function for the DAQ is relatively short, the readout is mostly defined by the options opts given:

```
1  int DAQ::read(long bufferSize, int opts) {
2    mh = cbScaledWinBufAlloc(bufferSize);
3    if (mh == 0) {
4      return -1;
5    }
6    // Scan from channel 0 to nCHAN -1
7    ulStat = cbAInScan(boardNum, 0, nCHAN - 1, bufferSize, &
        samplingRate, gain, mh, opts);
8    data = (WORD*)mh;
9    return 0;
10 }
```

The continuous readout is then started, and while the readout is running in the background, the demodulation is performed:

```
1  void DAQ::continuosMeasure() {
2    /* variable declarations skipped */
3    int r = read(bufferSize, SCALEDATA + CONTINUOUS +
        BACKGROUND + BLOCKIO);
4    /* save location skipped */
5    while (active && status == RUNNING) {
```

```
6      // Get new data
7      cbGetStatus(boardNum, &status, &currCount, &currIndex,
          AIFUNCTION);
8
9      // if there is new data, do . . .
10     if (currCount >= prevCount + nCHAN * AVERAGING) {
11       double sums[nCHAN] { 0 },
12         sumsQ[nCHAN][nFREQ]{ 0 },
13         sumsI[nCHAN][nFREQ]{ 0 };
14
15       // Check if going through the samples will remain
            within buffer bounds
16       if (handleIndex + nCHAN * AVERAGING < bufferSize) {
17         // Go through all channels
18         for (int c = 0; c < nCHAN; c++) {
19           // Go through the amount of samples to be averaged
                over
20           for (int s = 0; s < AVERAGING; s++) {
21             double val = voltage[handleIndex + c + nCHAN * s
                ];
22             sums[c] += val / AVERAGING;
23             // Go through demodulation frequencies
24             for (int df = 0; df < nFREQ; df++) {
25               sumsQ[c][df] += val * cos(2. * M_PI * freqs[df
                  ] / SAMPLING * cosCount[c][df]++) /
                  AVERAGING;
26               sumsI[c][df] += val * sin(2. * M_PI * freqs[df
                  ] / SAMPLING * sinCount[c][df]++) /
                  AVERAGING;
27             }
28           }
29         }
30         handleIndex += nCHAN * AVERAGING;
31       }
32       else {
33         // Go through all channels
34         for (int c = 0; c < nCHAN; c++) {
35           // initialize variables for buffer overrun
36           bool hit = false;
37           int offset = 0;
38           // Go through the amount of samples to average
39           for (int s = 0; s < AVERAGING; s++) {
```

```
40              double val = 0;
41              // Check for buffer overrun and get sample
42              if (handleIndex + c + nCHAN * s >= bufferSize) {
43                if (!hit) {
44                  hit = true;
45                  offset = s * nCHAN;
46                }
47                val = voltage[c + nCHAN * s - offset];
48              }
49              else {
50                val = voltage[handleIndex + c + nCHAN * s];
51              }
52              sums[c] += val / AVERAGING;
53              // Go through demodulation frequencies
54              for (int df = 0; df < nFREQ; df++) {
55                sumsQ[c][df] += val * cos(2. * M_PI * freqs[df
                      ] / SAMPLING * cosCount[c][df]++) /
                      AVERAGING;
56                sumsI[c][df] += val * sin(2. * M_PI * freqs[df
                      ] / SAMPLING * sinCount[c][df]++) /
                      AVERAGING;
57              }
58            }
59          }
60          handleIndex += nCHAN * AVERAGING;
61          if (handleIndex >= bufferSize)
62            handleIndex -= bufferSize;
63        }
64        // Write data to the output buffers console and (if
              activated) to output files
65        for (int c = 0; c < nCHAN; c++) {
66          conOut[c][0] = sums[c];
67          if (saving)
68            fprintf(file[c], "%-11f", sums[c]);
69          // Go through demodulation frequencies
70          for (int df = 0; df < nFREQ; df++) {
71            double ampl = 2. * sqrt(pow(sumsQ[c][df], 2.) +
                  pow(sumsI[c][df], 2.)),
72              phase = atan2(sumsQ[c][df], sumsI[c][df]);
73            conOut[c][1 + 2 * df] = ampl;
74            conOut[c][2 + 2 * df] = phase;
75            if (saving)
```

```
76              fprintf(file[c], "%-11f%-11f", ampl, phase);
77          }
78          if (saving)
79            fprintf(file[c], "\n");
80        }
81
82        prevCount = currCount;
83        prevIndex = currIndex;
84      }
85    }
86  }
```

Bibliography

[1] A. Einstein. "Die Grundlage der allgemeinen Relativitätstheorie". In: *Annalen der Physik* 354.7 (1916), pp. 769–822. DOI: `10.1002/andp.19163540702`.

[2] M. Bailes et al. "Gravitational-wave physics and astronomy in the 2020s and 2030s". In: *Nature Reviews Physics* (2021). DOI: `10.1038/s42254-021-00303-8`.

[3] C J Moore et al. "Gravitational-wave sensitivity curves". In: *Classical and Quantum Gravity* 32.1 (2014), p. 015014. DOI: `10.1088/0264-9381/32/1/015014`.

[4] B. S. Sathyaprakash and Bernard F. Schutz. "Physics, Astrophysics and Cosmology with Gravitational Waves". In: *Living Reviews in Relativity* 12.1 (2009). DOI: `10.12942/lrr-2009-2`.

[5] Joel M. Weisberg et al. "Gravitational Waves from an Orbiting Pulsar". In: *Scientific American* 245.4 (1981), pp. 74–82. DOI: `10.1038/scientificamerican1081-74`.

[6] J. H. Taylor and J. M. Weisberg. "A new test of general relativity - Gravitational radiation and the binary pulsar PSR 1913+16". In: *The Astrophysical Journal* 253 (1982), p. 908. DOI: `10.1086/159690`.

[7] J. M. Weisberg and J. H. Taylor. "The Relativistic Binary Pulsar B1913+16". In: (Nov. 2002). arXiv: `astro-ph/0211217 [astro-ph]`.

[8] Ingrid H. Stairs. "Testing General Relativity with Pulsar Timing". In: *Living Reviews in Relativity* 6.1 (2003). DOI: `10.12942/lrr-2003-5`.

[9]   B. P. Abbott et al. "Observation of Gravitational Waves from a Binary Black Hole Merger". In: *Physical Review Letters* 116.6 (Feb. 2016). DOI: `10.1103/physrevlett.116.061102`.

[10]   Inductiveload. *PSR B1913+16 period shift graph*. Retrieved 2021-12-17. 2010. URL: `https://commons.wikimedia.org/wiki/File:PSR_B1913+16_period_shift_graph.svg`.

[11]   J. M. Weisberg and J. H. Taylor. "Relativistic Binary Pulsar B1913+16: Thirty Years of Observations and Analysis". In: (July 2004). arXiv: `astro-ph/0407149 [astro-ph]`.

[12]   LIGO Scientific Collaboration. *Data release for event GW150914*. 2016. DOI: `10.7935/K5MW2F23`.

[13]   B. P. Abbott et al. "GWTC-1: A Gravitational-Wave Transient Catalog of Compact Binary Mergers Observed by LIGO and Virgo during the First and Second Observing Runs". In: *Physical Review X* 9.3 (2019), p. 031040. DOI: `10.1103/physrevx.9.031040`.

[14]   R. Abbott et al. "GWTC-2: Compact Binary Coalescences Observed by LIGO and Virgo during the First Half of the Third Observing Run". In: *Physical Review X* 11.2 (2021), p. 021053. DOI: `10.1103/physrevx.11.021053`.

[15]   B. P. Abbott et al. "GW190425: Observation of a Compact Binary Coalescence with Total Mass $\sim$ 3.4 M$\odot$". In: *The Astrophysical Journal Letters* 892.1 (2020), p. L3. DOI: `10.3847/2041-8213/ab75f5`.

[16]   R. Abbott et al. "Observation of Gravitational Waves from Two Neutron Star–Black Hole Coalescences". In: *The Astrophysical Journal Letters* 915.1 (2021), p. L5. DOI: `10.3847/2041-8213/ac082e`.

[17]   B. P. Abbott et al. "GW170817: Observation of Gravitational Waves from a Binary Neutron Star Inspiral". In: *Physical Review Letters* 119.16 (2017). DOI: `10.1103/physrevlett.119.161101`.

[18]   B. P. Abbott et al. "Multi-messenger Observations of a Binary Neutron Star Merger". In: *The Astrophysical Journal* 848.2 (2017), p. L12. DOI: `10.3847/2041-8213/aa91c9`.

[19] B P Abbott et al. "LIGO: the Laser Interferometer Gravitational-Wave Observatory". In: *Reports on Progress in Physics* 72.7 (2009), p. 076901. DOI: 10.1088/0034-4885/72/7/076901.

[20] J Aasi et al. "Advanced LIGO". In: *Classical and Quantum Gravity* 32.7 (2015), p. 074001. DOI: 10.1088/0264-9381/32/7/074001.

[21] F Acernese et al. "Virgo status". In: *Classical and Quantum Gravity* 25.18 (2008), p. 184001. DOI: 10.1088/0264-9381/25/18/184001.

[22] F Acernese et al. "Advanced Virgo: a second-generation interferometric gravitational wave detector". In: *Classical and Quantum Gravity* 32.2 (2014), p. 024001. DOI: 10.1088/0264-9381/32/2/024001.

[23] D. V. Martynov et al. "Sensitivity of the Advanced LIGO detectors at the beginning of gravitational wave astronomy". In: *Physical Review D* 93.11 (2016), p. 112004. DOI: 10.1103/physrevd.93.112004.

[24] Diego Bersanetti et al. "Advanced Virgo: Status of the Detector, Latest Results and Future Prospects". In: *Universe* 7.9 (2021), p. 322. DOI: 10.3390/universe7090322.

[25] Stefan Hild et al. "Pushing towards the ET sensitivity using 'conventional' technology". In: (Oct. 2008). arXiv: 0810.0604 [gr-qc].

[26] David Reitze et al. "Cosmic Explorer: The U.S. Contribution to Gravitational-Wave Astronomy beyond LIGO". In: *2019 BAAS 51(7) 035* (July 2019). arXiv: 1907.04833 [astro-ph.IM].

[27] Matthew Pitkin et al. "Gravitational Wave Detection by Interferometry (Ground and Space)". In: *Living Reviews in Relativity* 14.1 (July 2011). DOI: 10.12942/lrr-2011-5.

[28] Karsten Danzmann. "LISA — An ESA cornerstone mission for the detection and observation of gravitational waves". In: *Advances in Space Research* 32.7 (2003), pp. 1233–1242. DOI: 10.1016/s0273-1177(03)90323-1.

[29]   Pau Amaro-Seoane et al. "Laser Interferometer Space Antenna".
       In: (Feb. 2, 2017). arXiv: 1702.00786v3 [astro-ph.IM].

[30]   Oliver Gerberding et al. *TN 1: Design Report*. Tech. rep. LISA-
       AEI-PRDS-TN1-2019. 2019.

[31]   Vitali Müller. "Design considerations for future geodesy missions
       and for space laser interferometry". PhD thesis. Gottfried Wilhelm
       Leibniz Universität Hannover, 2017. DOI: 10.15488/9029.

[32]   Frank Träger, ed. *Springer Handbook of Lasers and Optics*. Springer
       New York, 2007. DOI: 10.1007/978-0-387-30420-5.

[33]   Andreas Freise and Kenneth Strain. "Interferometer Techniques
       for Gravitational-Wave Detection". In: *Living Reviews in Relativity*
       13.1 (2010). DOI: 10.12942/lrr-2010-1.

[34]   Oliver Gerberding. "Phase readout for satellite interferometry".
       PhD thesis. Leibniz Universität Hannover, 2014.

[35]   Vladimir V. Protopopov. *Laser Heterodyning*. Springer Berlin Hei-
       delberg, 2009. DOI: 10.1007/978-3-642-02338-5.

[36]   Günter Winstel and Claus Weyrich. *Optoelektronik II*. Springer
       Berlin Heidelberg, 1986. DOI: 10.1007/978-3-642-82640-5.

[37]   Christoph Mahrdt. *Contrast and heterodyne efficiency*. LRI-AEI-
       TN-012. 2011.

[38]   Juan José Esteban et al. "Ranging and phase measurement for
       LISA". In: *Journal of Physics: Conference Series* 228 (2010), p. 012045.
       DOI: 10.1088/1742-6596/228/1/012045.

[39]   Frank L. Pedrotti et al. *Introduction to Optics*. Cambridge Uni-
       versity Press, 2017. DOI: 10.1017/9781108552493.

[40]   Bahaa Saleh. *Optik und Photonik*. Newark: John Wiley & Sons,
       Incorporated, 2020. ISBN: 9783527825912.

[41]   Dennis Goldstein. *Polarized light*. Boca Raton, FL: CRC Press,
       2011. ISBN: 9781439830406.

[42] Thomas S. Schwarze et al. "Picometer-Stable Hexagonal Optical Bench to Verify LISA Phase Extraction Linearity and Precision". In: *Physical Review Letters* 122.8 (2019). DOI: `10.1103/physrevlett.122.081104`.

[43] Katharina-Sophie Isleif. "Laser interferometry for LISA and satellite geodesy missions". PhD thesis. Hannover: Gottfried Wilhelm Leibniz Universität Hannover, 2018. DOI: `10.15488/3526`. URL: `https://www.tib.eu/de/suchen/id/TIBKAT%3A1030356750`.

[44] Dieter Meschede. *Optik, Licht und Laser*. Vieweg+Teubner, 2008. DOI: `10.1007/978-3-8348-9288-1`.

[45] G. W. Day. "Birefringence Measurements In Single Mode Optical Fiber". In: *Single Mode Optical Fibers*. Ed. by A. D. Pearson. SPIE, 1983. DOI: `10.1117/12.936216`.

[46] K. Danzmann and The LISA Consortium. "The Gravitational Universe". In: (May 24, 2013). arXiv: `1305.5720v1 [astro-ph.CO]`.

[47] K. Danzmann for the LISA Study Team. "LISA - an ESA cornerstone mission for a gravitational wave observatory". In: *Classical and Quantum Gravity* 14.6 (1997), pp. 1399–1404. DOI: `10.1088/0264-9381/14/6/002`.

[48] Scott A. Hughes. "A brief survey of LISA sources and science". In: *AIP Conference Proceedings*. AIP, 2006. DOI: `10.1063/1.2405017`.

[49] Rhondale Tso et al. "Optimizing LIGO with LISA forewarnings to improve black-hole spectroscopy". In: *Physical Review D* 99.12 (2019), p. 124043. DOI: `10.1103/physrevd.99.124043`.

[50] LISA Instrument Group. *LISA Payload Definition Document*. Tech. rep. ESA-L3-EST-INST-DD-001. European Space Agency, 2018.

[51] Peter F. Gath et al. "Challenges in the Measurement and Data-Processing Chain of the LISA Mission". In: *Space Science Reviews* 151.1-3 (2009), pp. 61–73. DOI: `10.1007/s11214-009-9604-8`.

[52]   Yan Wang et al. "First stage of LISA data processing. II. Alternative filtering dynamic models for LISA". In: *Physical Review D* 92.4 (2015), p. 044037. DOI: 10.1103/physrevd.92.044037.

[53]   Hubert Halloin. "Optimizing orbits for (e)LISA". In: *Journal of Physics: Conference Series* 840 (2017), p. 012048. DOI: 10.1088/1742-6596/840/1/012048.

[54]   E. D. Fitzsimons et al. "eLISA technology consolidation study overview". In: *International Conference on Space Optics — ICSO 2014*. Ed. by Bruno Cugny et al. SPIE, 2017. DOI: 10.1117/12.2304251.

[55]   Waldemar Martens and Eric Joffre. "Trajectory Design for the ESA LISA Mission". In: *The Journal of the Astronautical Sciences* 68.2 (2021), pp. 402–443. DOI: 10.1007/s40295-021-00263-2.

[56]   Ulrich Johann et al. "Novel payload architectures for LISA". In: *International Conference on Space Optics — ICSO 2006*. Ed. by Errico Armandillo et al. SPIE, 2017. DOI: 10.1117/12.2308123.

[57]   K-S Isleif et al. "Suppressing ghost beams: Backlink options for LISA". In: *Journal of Physics: Conference Series* 840 (May 2017), p. 012016. DOI: 10.1088/1742-6596/840/1/012016.

[58]   Katharina-Sophie Isleif et al. "Towards the LISA backlink: experiment design for comparing optical phase reference distribution systems". In: *Classical and Quantum Gravity* 35.8 (Mar. 2018), p. 085009. DOI: 10.1088/1361-6382/aaa879.

[59]   Jens Reiche et al. *Technical Proposal Prepared in response to ESA ITT AO/1-8586/16/NL/BW*. Tech. rep. eLISA-AEI-PROP-2016-01-01. 2016.

[60]   Markus Otto. "Time-delay interferometry simulations for the laser interferometer space antenna". eng. PhD thesis. Gottfried Wilhelm Leibniz Universität Hannover, 2015. DOI: 10.15488/8545.

[61]   Massimo Tinto and Sanjeev V. Dhurandhar. "Time-delay interferometry". In: *Living Reviews in Relativity* 24.1 (2020). DOI: 10.1007/s41114-020-00029-6.

[62] Roland Fleddermann et al. "Measurement of the non-reciprocal phase noise of a polarization maintaining single-mode optical fiber". In: *Journal of Physics: Conference Series* 154 (Mar. 2009), p. 012022. DOI: 10.1088/1742-6596/154/1/012022.

[63] Roland Fleddermann. "Interferometry for a space-based gravitational wave observatory: Reciprocity of an optical fiber." PhD thesis. Leibniz Universität Hannover, 2012.

[64] Roland Fleddermann et al. "Sub-pm$\sqrt{\text{Hz}}^{-1}$ non-reciprocal noise in the LISA backlink fiber". In: *Classical and Quantum Gravity* 35.7 (Feb. 2018), p. 075007. DOI: 10.1088/1361-6382/aaa276.

[65] Christian Diekmann. *Development of core elements for the LISA optical bench : electro-optical measurement systems and test devices.* eng. 2013. DOI: 10.15488/8036.

[66] Jan-Simon Henning. "Mitigation of Stray Light Eects in the LISA Backlink". MA thesis. Leibniz Universität Hannover, 2013.

[67] J. Matsuoka et al. "Temperature dependence of refractive index of SiO2 glass". In: *Journal of Non-Crystalline Solids* 135.1 (1991), pp. 86–89. DOI: 10.1016/0022-3093(91)90447-e.

[68] H. Taylor. "Bending effects in optical fibers". In: *Journal of Lightwave Technology* 2.5 (1984), pp. 617–628. DOI: 10.1109/jlt.1984.1073659.

[69] Bahaa Saleh. *Grundlagen der Photonik*. Weinheim: Wiley-VCH, 2008. ISBN: 9783527406777.

[70] E.J. Daly. "The radiation belts". In: *Radiation Physics and Chemistry* 43.1-2 (1994), pp. 1–17. DOI: 10.1016/0969-806x(94)90198-8.

[71] David F. Medina. "Solar Radiation and Spacecraft Shielding". In: *Handbook of Cosmic Hazards and Planetary Defense*. Springer International Publishing, 2015, pp. 295–314. DOI: 10.1007/978-3-319-03952-7_10.

[72] Mark Millinger and Piers Jiggens. *LISA Environment Specification*. Tech. rep. ESA-L3-EST-MIS-SP-001, ESA-TEC-SP-00666. European Space Agency, 2017.

[73] Francis Berghmans et al. "An Introduction to Radiation Effects on Optical Components and Fiber Optic Sensors". In: *Optical Waveguide Sensing and Imaging*. Springer Netherlands, 2008, pp. 127–165. DOI: `10.1007/978-1-4020-6952-9_6`.

[74] S Babani et al. "Comparative study between fiber optic and copper in communication link". In: *Int. J. Tech. Res. Appl* 2.2 (2014), pp. 59–63.

[75] Biswanath Mukherjee et al., eds. *Springer Handbook of Optical Networks*. Springer International Publishing, 2020. DOI: `10.1007/978-3-030-16250-4`.

[76] Ajoy Ghatak and K. Thyagarajan. *Introduction to fiber optics*. Cambridge University Press, 1998. DOI: `10.1017/cbo9781139174770`.

[77] Rongqing Hui. *Introduction to fiber-optic communications*. Amsterdam: Academic Press, 2019. ISBN: 9780128053454.

[78] Mingjie Ding et al. "Basics of Optical Fiber Measurements". In: *Handbook of Optical Fibers*. Springer Singapore, 2019, pp. 1099–1137. DOI: `10.1007/978-981-10-7087-7_57`.

[79] K. Kyuma et al. "Fiber-Optic Instrument for Temperature Measurement". In: *IEEE Transactions on Microwave Theory and Techniques* 30.4 (1982), pp. 522–525. DOI: `10.1109/tmtt.1982.1131092`.

[80] G. Betta and A. Pietrosanto. "An intrinsic fiber optic temperature sensor". In: *IEEE Transactions on Instrumentation and Measurement* 49.1 (2000), pp. 25–29. DOI: `10.1109/19.836303`.

[81] B.D Gupta and Ratnanjali. "A novel probe for a fiber optic humidity sensor". In: *Sensors and Actuators B: Chemical* 80.2 (2001), pp. 132–135. DOI: `10.1016/s0925-4005(01)00899-1`.

[82] Shizhuo Yin. *Fiber optic sensors*. Boca Raton, FL: CRC Press, 2008. ISBN: 9781420053654.

[83] Eric Udd and William B. Spillman, eds. *Fiber Optic Sensors*. John Wiley & Sons, Inc., 2011. DOI: 10.1002/9781118014103.

[84] D. R. Biswas. "Optical fiber coatings". In: *Fiber Optics Reliability and Testing: A Critical Review*. SPIE, 1993. DOI: 10.1117/12.181374.

[85] Niloy Dutta. *Fiber amplifiers and fiber lasers*. Hackensack New Jersey: World Scientific, 2015. ISBN: 9789814630399.

[86] Fibercore. *Zing™ Polarizing Fiber*. Tech. rep. TN09/2. Fibercore, 2014.

[87] Fibercore. *Zing™ fiber*. Tech. rep. AN22/1. Fibercore, 2018.

[88] Tomasz R Wolinski and Agnieszka Szymanska. "Polarimetric optical fibres with elliptical liquid-crystal core". In: *Measurement Science and Technology* 12.7 (2001), p. 948. DOI: https://doi.org/10.1088/0957-0233/12/7/335.

[89] Lixian Wang and Sophie LaRochelle. "Design of eight-mode polarization-maintaining few-mode fiber for multiple-input multiple-output-free spatial division multiplexing". In: *Optics Letters* 40.24 (2015), p. 5846. DOI: 10.1364/ol.40.005846.

[90] B Hillerich and E. Weidel. "Polarization noise in single mode fibres and its reduction by depolarizers". In: *Opt Quant Electron* 15 (1983), pp. 281–287. DOI: https://doi.org/10.1007/BF00619897.

[91] J. Noda et al. "Polarization-maintaining fibers and their applications". In: *Journal of Lightwave Technology* 4.8 (1986), pp. 1071–1089. DOI: 10.1109/jlt.1986.1074847.

[92] M. E. Lines. "The Search for Very Low Loss Fiber-Optic Materials". In: *Science* 226.4675 (Nov. 1984), pp. 663–668. DOI: 10.1126/science.226.4675.663.

[93] Rongqing Hui and Maurice O'Sullivan. "Optical Fiber Measurement". In: *Fiber Optic Measurement Techniques*. Elsevier, 2009, pp. 365–479. DOI: 10.1016/b978-0-12-373865-3.00004-5.

[94]   D. Gloge. "Bending Loss in Multimode Fibers with Graded and Ungraded Core Index". In: *Applied Optics* 11.11 (1972), p. 2506. DOI: `10.1364/ao.11.002506`.

[95]   Jun ichi Sakai and Tatsuya Kimura. "Bending loss of propagation modes in arbitrary-index profile optical fibers". In: *Applied Optics* 17.10 (1978), p. 1499. DOI: `10.1364/ao.17.001499`.

[96]   Min Gu et al. "Scattering of Light by Small Particles". In: *Microscopic Imaging Through Turbid Media*. Springer Berlin Heidelberg, 2015, pp. 15–23. DOI: `10.1007/978-3-662-46397-0_2`.

[97]   Andrey Kobyakov et al. "Stimulated Brillouin scattering in optical fibers". In: *Advances in Optics and Photonics* 2.1 (2009), p. 1. DOI: `10.1364/aop.2.000001`.

[98]   R. H. Stolen et al. "Raman Oscillation in Glass Optical Waveguide". In: *Applied Physics Letters* 20.2 (1972), pp. 62–64. DOI: `10.1063/1.1654046`.

[99]   Alasdair Taylor. *Delivery Fiber Options*. Presentation in the LISA Laser WG. June 2019.

[100] Xinyu Fan. "Distributed Rayleigh Sensing". In: *Handbook of Optical Fibers*. Springer Singapore, 2018, pp. 1–50. DOI: `10.1007/978-981-10-1477-2_5-1`.

[101] Arthur H. Hartog. *An Introduction to Distributed Optical Fibre Sensors*. CRC Press, 2017. DOI: `10.1201/9781315119014`.

[102] Kyozo Tsujikawa et al. "Method for Predicting Rayleigh Scattering Loss of Silica-Based Optical Fibers". In: *Journal of Lightwave Technology* 25.8 (2007), pp. 2122–2128. DOI: `10.1109/jlt.2007.899789`.

[103] K. Saito et al. "Approach for reducing the Rayleigh scattering loss in optical fibers". In: *Journal of Applied Physics* 95.4 (2004), pp. 1733–1735. DOI: `10.1063/1.1638887`.

[104] Kyozo Tsujikawa et al. "Intrinsic loss of optical fibers". In: *Optical Fiber Technology* 11.4 (2005), pp. 319–331. DOI: `10.1016/j.yofte.2005.04.003`.

[105] Hesham Sakr et al. "Hollow core optical fibres with comparable attenuation to silica fibres between 600 and 1100 nm". In: *Nature Communications* 11.1 (2020). DOI: `10.1038/s41467-020-19910-7`.

[106] M. Balkanski. "SEMICONDUCTOR PHYSICS | Light Scattering". In: *Encyclopedia of Modern Optics*. Elsevier, 2005, pp. 460–465. DOI: `10.1016/b0-12-369395-0/00628-x`.

[107] S. Girard et al. "Radiation Effects on Silica-Based Optical Fibers: Recent Advances and Future Challenges". In: *IEEE Transactions on Nuclear Science* 60.3 (2013), pp. 2015–2036. DOI: `10.1109/tns.2012.2235464`.

[108] E. J. Friebele et al. "Overview Of Radiation Effects In Fiber Optics". In: *Radiation Effects on Optical Materials*. Ed. by Paul W. Levy. SPIE, 1985. DOI: `10.1117/12.975360`.

[109] D. Ehrt and W. Vogel. "Radiation effects in glasses". In: *Nuclear Instruments and Methods in Physics Research Section B: Beam Interactions with Materials and Atoms* 65.1-4 (1992), IN1–8. DOI: `10.1016/0168-583x(92)95006-d`.

[110] Iacopo Toccafondo et al. "Distributed Optical Fiber Radiation Sensing in a Mixed-Field Radiation Environment at CERN". In: *Journal of Lightwave Technology* 35.16 (2017), pp. 3303–3310. DOI: `10.1109/jlt.2016.2608849`.

[111] D. Di Francesca et al. "Radiation-Induced Attenuation in Single-Mode Phosphosilicate Optical Fibers for Radiation Detection". In: *IEEE Transactions on Nuclear Science* 65.1 (2018), pp. 126–131. DOI: `10.1109/tns.2017.2778314`.

[112] William R. Leo. "Scintillation Detectors". In: *Techniques for Nuclear and Particle Physics Experiments*. Springer Berlin Heidelberg, 1994, pp. 157–175. DOI: `10.1007/978-3-642-57920-2_7`.

[113] William Primak and Robert Kampwirth. "The Radiation Compaction of Vitreous Silica". In: *Journal of Applied Physics* 39.12 (1968), pp. 5651–5658. DOI: `10.1063/1.1656029`.

[114] Dan Sporea. "Optical Fiber Sensors in Ionizing Radiation Environments". In: *Handbook of Optical Fibers*. Springer Singapore, 2017, pp. 1–42. DOI: `10.1007/978-981-10-1477-2_25-1`.

[115] Paul W. Levy. "Color Centers and Radiation-Induced Defects in Al2O3". In: *Physical Review* 123.4 (1961), pp. 1226–1233. DOI: `10.1103/physrev.123.1226`.

[116] E. J. Friebele and D. L. Griscom. "Color Centers in Glass Optical Fiber Waveguides". In: *MRS Proceedings* 61 (1985). DOI: `10.1557/proc-61-319`.

[117] Joseph W. Goodman. *Speckle Phenomena in Optics: Theory and Applications, Second Edition*. SPIE, 2020. DOI: `10.1117/3.2548484`.

[118] Vitalii Khodnevych. "Scattered light studies for the LISA optical metrologysystem". PhD thesis. Université Côte d'Azur, 2020. URL: `https://tel.archives-ouvertes.fr/tel-03177562`.

[119] Jan Rybizki. "LISA back-link fibre: back reflection of a polarisation maintaining single-mode optical fibre". Diploma thesis. Leibniz Universität Hannover, 2011.

[120] Pavol Stajanca and Katerina Krebber. "Radiation-Induced Attenuation of Perfluorinated Polymer Optical Fibers for Radiation Monitoring". In: *Sensors* 17.9 (2017), p. 1959. DOI: `10.3390/s17091959`.

[121] R H. West. "Radiation Effects On Fibre Optics". In: *Optical Devices in Adverse Environments*. Ed. by Roger A. Greenwell. SPIE, 1988. DOI: `10.1117/12.965056`.

[122] Brigitte Kaune. "In-orbit Stability Analysis of the LISA Pathfinder Optical Metrology: Photoreceivers and Polarisation". en. PhD thesis. Gottfried Wilhelm Leibniz Universität Hannover, 2021. DOI: `10.15488/10887`.

[123] Measurement Computing. *USB-1608FS-Plus Simultaneous USB DAQ Device*. Apr. 2018. URL: `https://www.mccdaq.com/PDFs/specs/DS-USB-1608FS-Plus.pdf`.

[124] Bryan Lizon. *Fundamentals of Precision ADC Noise Analysis.* Texas Instruments, 2020. URL: `https://www.ti.com/lit/eb/slyy192/slyy192.pdf`.

[125] Michael Tröbs and Gerhard Heinzel. "Improved spectrum estimation from digitized time series on a logarithmic frequency axis". In: *Measurement* 39.2 (2006), pp. 120–129. DOI: `10.1016/j.measurement.2005.10.010`.

[126] Laird Thermal Systems. *DA PowerCool Series DA-160-24-02 Thermoelectric Assembly.* URL: `https://assets.lairdtech.com/home/brandworld/files/Laird-ETS-PowerCool-Series-DA-160-24-02-Data-Sheet.pdf`.

[127] Laird Thermal Systems. *PR-59 and LT-Interface user manual.* URL: `https://assets.lairdtech.com/home/brandworld/files/LT-THR-UM-PR591212.pdf`.

[128] Jochen Kuhnhenn et al. "Quality Assurance for Irradiation Tests of Optical Fibers: Uncertainty and Reproducibility". In: *IEEE Transactions on Nuclear Science* 56.4 (2009), pp. 2160–2166. DOI: `10.1109/tns.2009.2019605`.

[129] Simone Schmitz. *Co-60 gamma and 14 MeV neutron irradiation of PRDS Fibers.* Tech. rep. NEO-18-084. Fraunhofer-Institut für Naturwissenschaftlich-Technische Trendanalysen (INT), 2018.

[130] Max Zwetz and Stefan Ast. *Phase Reference Distribution System: Fibre Irradiation Test Procedure.* Tech. rep. LISA-AEI-PRDS-TP-001. Albert-Einstein-Institut Hannover, 2018.

[131] Johann Max Rohr et al. "Fiber backscatter under increasing exposure to ionizing radiation". In: *Optics Express* 28.23 (2020), p. 34894. DOI: `10.1364/oe.404139`.

[132] Maryanne C. J. Large et al. *Microstructured Polymer Optical Fibres.* Springer US, 2008. DOI: `10.1007/978-0-387-68617-2`.

[133] G. B. Hocker. "Fiber-optic sensing of pressure and temperature". In: *Applied Optics* 18.9 (1979), p. 1445. DOI: `10.1364/ao.18.001445`.

[134]   N. Lagakos et al. "Temperature-induced optical phase shifts in fibers". In: *Applied Optics* 20.13 (1981), p. 2305. DOI: `10.1364/ao.20.002305`.

[135]   S.J. Wilson. "Temperature sensitivity of optical fibre path length". In: *Optics Communications* 71.6 (1989), pp. 345–350. DOI: `10.1016/0030-4018(89)90046-1`.

[136]   UK OB team. *OB Design Report*. Tech. rep. LISA-UKOB-INST-RP-0005-i1. 2021.

[137]   M. Donno et al. "A New Flexible Optical Fiber Goniometer for Dynamic Angular Measurements: Application to Human Joint Movement Monitoring". In: *IEEE Transactions on Instrumentation and Measurement* 57.8 (2008), pp. 1614–1620. DOI: `10.1109/tim.2008.925336`.

[138]   L. M. N. Amaral et al. "Fiber-Optic Inclinometer Based on Taper Michelson Interferometer". In: *IEEE Sensors Journal* 11.9 (2011), pp. 1811–1814. DOI: `10.1109/jsen.2011.2105264`.

[139]   N. Fürstenau et al. "Simultaneous interferometric and polarimetric strain measurements on composites using a fiber-optic strain gauge". In: *Applied Optics* 31.16 (1992), p. 2987. DOI: `10.1364/ao.31.002987`.

[140]   Marcel Berger et al. "Opto-mechanical architecture of the LISA instrument". In: *International Conference on Space Optics — ICSO 2008*. Ed. by Josiane Costeraste et al. SPIE, 2017. DOI: `10.1117/12.2308192`.

[141]   Oliver Gerberding and Katharina-Sophie Isleif. *Recommended PRDS point design*. Tech. rep. eLISA-AEI-PRDS-2019-04-TN-PRDSrec. 2019.

[142]   Ewan Fitzsimons et al. *LISA Performance Model, Issue 2.1*. Tech. rep. LISA-LSCT-INST-TN-003. 2021.

[143]   Raymond T. Birge. "The Propagation of Errors". In: *American Journal of Physics* 7.6 (1939), pp. 351–357. DOI: `10.1119/1.1991484`.

[144] H.H. Ku. "Notes on the use of propagation of error formulas". In: *Journal of Research of the National Bureau of Standards, Section C: Engineering and Instrumentation* 70C.4 (1966), p. 263. DOI: 10.6028/jres.070c.025.

[145] Melanie Ast et al. *TN 1: Review of noise sources in laserdifferential phase noise*. Tech. rep. L-LTS-AEI-TN-1-001-002. Max Planck Institute for Gravitational Physics, 2019.

[146] Melanie Ast et al. *Detailed Design Description and Report of the ESA Project LISA Laser Test Setup*. Tech. rep. L-LTS-AEI-DD-001. Max Planck Institute for Gravitational Physics, 2019.

[147] B Willke et al. "Stabilized lasers for advanced gravitational wave detectors". In: *Classical and Quantum Gravity* 25.11 (2008), p. 114040. DOI: 10.1088/0264-9381/25/11/114040.

[148] Katharina-Sophie Isleif et al. "Experimental demonstration of deep frequency modulation interferometry". In: *Optics Express* 24.2 (2016), p. 1676. DOI: 10.1364/oe.24.001676.

[149] Katharina-Sophie Isleif et al. "Compact Multifringe Interferometry with Subpicometer Precision". In: *Physical Review Applied* 12.3 (2019). DOI: 10.1103/physrevapplied.12.034025.

[150] L.D Turner et al. "Frequency noise characterisation of narrow linewidth diode lasers". In: *Optics Communications* 201.4-6 (2002), pp. 391–397. DOI: 10.1016/s0030-4018(01)01689-3.

[151] R. W. P. Drever et al. "Laser phase and frequency stabilization using an optical resonator". In: *Applied Physics B Photophysics and Laser Chemistry* 31.2 (1983), pp. 97–105. DOI: 10.1007/bf00702605.

[152] Oliver Gerberding et al. "Laser-Frequency Stabilization via a Quasi-monolithic Mach-Zehnder Interferometer with Arms of Unequal Length and Balanced dc Readout". In: *Physical Review Applied* 7.2 (2017). DOI: 10.1103/physrevapplied.7.024027.

[153]   K Takahashi et al. "Stabilization of laser intensity and frequency using optical fiber". In: 122 (2008), p. 012016. DOI: 10.1088/1742-6596/122/1/012016.

[154]   Chathura P. Bandutunga et al. "Infrasonic performance of a passively stabilized, all-fiber, optical frequency reference". In: *Optics Express* 28.7 (Mar. 2020), p. 9280. DOI: 10.1364/oe.390250.

[155]   I. H. Malitson. "Interspecimen Comparison of the Refractive Index of Fused Silica". In: *Journal of the Optical Society of America* 55.10 (1965), p. 1205. DOI: 10.1364/josa.55.001205.

List of Publications

Journal papers

- **Johann Max Rohr**, Stefan Ast, Oliver Gerberding, Jens Reiche, and Gerhard Heinzel *"Fiber backscatter under increasing exposure to ionizing radiation"* in *Optics Express* 28, 34894-34903 (2020). doi:10.1364/OE.404139

- M. Chwalla, K. Danzmann, M. Dovale Álvarez, J.J. Esteban Delgado, G. Fernández Barranco, E. Fitzsimons, O. Gerberding, G. Heinzel, C.J. Killow, M. Lieser, M. Perreur-Lloyd, D.I. Robertson, **J.M. Rohr**, S. Schuster, T.S. Schwarze, M. Tröbs, G. Wanner, and H. Ward *"Optical Suppression of Tilt-to-Length Coupling in the LISA Long-Arm Interferometer"* in *Physical Review Applied* 14, 014030 (2020). doi:10.1103/PhysRevApplied.14.014030

- Katharina-Sophie Isleif, Lea Bischof, Stefan Ast, Daniel Penkert, Thomas S Schwarze, Germán Fernández Barranco, **Max Zwetz**, Sonja Veith, Jan-Simon Hennig, Michael Tröbs, Jens Reiche, Oliver Gerberding, Karsten Danzmann and Gerhard Heinzel *"Towards the LISA backlink: experiment design for comparing optical phase reference distribution systems"* in *Classical and Quantum Gravity* 35 085009 (2018). doi:10.1088/1361-6382/aaa879

- M Tröbs, S Schuster, M Lieser, **M Zwetz**, M Chwalla, K Danzmann, G Fernández Barránco, E D Fitzsimons, O Gerberding, G Heinzel, C J Killow, M Perreur-Lloyd, D I Robertson, T S Schwarze, G Wanner and H Ward *"Reducing tilt-to-length coupling for the LISA test mass interferometer"* in *Classical and Quantum Gravity* 35 105001 (2018). doi:10.1088/1361-6382/aab86c

- M Chwalla, K Danzmann, G Fernández Barranco, E Fitzsimons, O Gerberding, G Heinze, C J Killow, M Lieser, M Perreur-Lloyd, D I Robertson, S Schuster, T S Schwarze, M Tröbs, H Ward and **M Zwetz** *"Design and construction of an optical test bed for LISA imaging systems and tilt-to-length coupling"* in *Classical and Quantum Gravity* 33 245015 (2016). doi:10.1088/0264-9381/33/24/245015

Project documents

- **Johann Max Rohr** *"Fiber Temperature to Phase Coupling"*, LISA-AEI-PRDS-TN-002 (2021).

- **Johann Max Rohr** *"2nd Fiber Irradiation Test Campaign Test Report"*, LISA-AEI-PRDS-RP-002 (2021).

- J. Reiche, **M. Rohr**, S. Ast, J. Eder, G.P. Guizzo *"Fibre Irradiation Test Procedure 2nd Test Campaign"*, LISA-AEI-PRDS-TP-002 (2020).

- J. Reiche, **M. Zwetz**, S. Ast, O. Gerberding, J. Eder, G. P. Guizzo *"Fibre Irradiation Test Report"*, LISA-AEI-PRDS-RP-001 (2019).

- J. Reiche, **M. Zwetz**, S. Ast, O. Gerberding, J. Eder, G. P. Guizzo *"Fibre Irradiation Test Procedure"*, LISA-AEI-PRDS-TP-001 (2018).

Bibliography

Acknowledgements

At this point, I want to thank numerous people, starting with the members of my thesis advisory committee, Prof. Dr. Karsten Danzmann, apl. Prof. Dr. Gerhard Heinzel, and Prof. Dr. Oliver Gerberding for giving me the opportunity to undergo my PhD studies at the Albert Einstein Institute. I am grateful to Prof. Danzmann for making the AEI what it is today, an open and helpful environment, and peaking my interest in the work at the AEI during my first-semester lecture you held. Gerhard, I thank you for taking the time to answer my questions, for your supervision, and for your support in times of need. And Oliver, I thank you for getting me in the backlink team and for all your help and tips when I planned and started my experiments. I am grateful to the three of you for all your suggestions and tips during our various TAC meetings.

Next, I want to thank Stefan Ast. Thank you for being the person I could pester with all my questions and ordering components after Oliver left for Hamburg, for sharing your experience with me, and for all your help with my experiment, especially during the more stressful times in the radiation campaign - helping to keep my calm during the long measurement days.

Furthermore, I want to thank apl. Prof. Dr. Benno Willke for agreeing to be my referee and apl. Prof. Dr. Milutin Kovacev for agreeing to head the examination committee.

A special thanks goes to my colleague and friend Markus Otto; one could say that it is "your fault" that I came to the AEI. Thank you for introduc-

ing me to the work in the space group during our archery training, which resulted in me doing my bachelor's thesis here and in me continuing my research path here. Thank you for your support, tips, and time.

My gratitude also goes to Jens Reiche for all your work and support while dealing with the project documents and contracts. Also, thank you for your support in organizing and doing the radiation campaigns.

Speaking of radiation campaigns: My thanks also go to Jochen Kuhnhenn, Simone Schmitz (both from Fraunhofer INT), Linda Mondin, Alessandra Costantino (both from ESA), and Nancy Postiau (from the CLC at UCLouvain) for your support in organizing and running the radiation facilities.

I am very thankful to Katharina Isleif, for providing your Python code to run the backlink performance simulations and offering your time to answer my questions regarding the simulations.

Similarly, I am very thankful to Michael Born for your support when performing the motion coupling tests in the LDPN experiment.

My gratitude also goes to my former and current office mates: Alex, Lea, Stefan, Jonathan, and Gunnar. It was and is always a pleasure to discuss work-related and unrelated topics with you.

Not to be missed, of course, the backlink team and its current and former members. Thank you all for the great teamwork and support. Special thanks here go to Dave Robertson from the University of Glasgow for providing the FIOSs for backscatter testing. Equally, my thanks go to the space interferometry group for the excellent working atmosphere and all the helpful discussions. My thanks also go to the secretaries and the workshops for all your help.

My utmost thanks go to my proofreaders: Stefan, Markus, Lea, Michael, Jordina, Melanie, and Katharina. Thank you for all your helpful comments!

Finally, I would like to thank my family, especially my wife, from the bottom of my heart; for your continued support over every step of this journey.

Curriculum Vitae

Personal Data

Name	Johann Max Rohr, né Zwetz
Born	August 5$^{\text{th}}$ 1991 in Hannover, Germany
Nationality	German

Academic Career

Since 2017	**Research Associate (PhD Candidate)**
	Max-Planck-Institute for Gravitational Physics
	(Albert Einstein Institute) and
	Institut für Gravitationsphysik, Leibniz Universität
	Hannover
2016 - 2014	**Master of Science (Physics)**
	Leibniz Universität Hannover
2014 - 2011	**Bachelor of Science (Physics)**
	Leibniz Universität Hannover
2011	**Abitur**
	Kaiser-Wilhelm- und Ratsgymnasium Hannover

WORK EXPERIENCE

2017 - 2020	**Exercise Coordinator (Laser interferometry, Experimental Physics I+II)**
	Leibniz Universität Hannover
2012 - 2016	**Instructor (Experimental Physics I-IV)**
	Leibniz Universität Hannover
2014 - 2016	**Instructor (uni:fit)**
	Leibniz Universität Hannover